UNIVERSITAT POLITÈCNICA DE VALÈNCIA

DEPARTAMENTO DE QUÍMICA

INSTITUTO UNIVERSITARIO MIXTO DE TECNOLOGÍA QUÍMICA (UPV-CSIC)

DOCTORAL THESIS

Design of new up-conversion systems for anticancer therapies

Cristina Anaya González

Supervisors:

Dr. Francisco Boscá Mayans

Prof. Rosa Esperanza Tormos Faus

Valencia, March 2021

CERTIFICATION

Francisco Boscá Mayans, principal Researcher at CSIC, and Rosa Esperanza Tormos Faus, full professor at Universitat Politècnica de València (UPV),

CERTIFY that the Doctoral Thesis entitled “Design of new up-conversion systems for anticancer therapies” has been developed by Cristina Anaya González under their supervision at the Instituto Universitario Mixto de Tecnología Química (UPV-CSIC).

Dr. Francisco Boscá Mayans Prof. Rosa Esperanza Tormos Faus

Symbols and abbreviations

^1A	Molecule singlet excited state
$^1O_2$	Singlet-oxygen
^3A	Molecule triplet excited state
A	Absorption
A	Acceptor
A*	Excited molecule
ACLFX	Acyl Lomefloxacin
AcOH	Acetic acid
A_{em}	Absorbance at emission wavelength
A_{ex}	Absorbance at excitation wavelength
BIO	Biomolecule
BZ	Benzene
$CDCl_3$	Deuterated chloroform
CH_2Cl_2	Dichloromethane
CH_3CN	Acetonitrile
CHB	Chlorambucil
CLL	Chronic Lymphocytic Leukemia
CR	Cross relaxation
CSU	Cooperative sensitization upconversion
D	Donor
DCO	Deacetyl-colchicine
DMEM	Dulbecco's Modified Eagle Medium
DMF	Dimethylformamide
DNA	Deoxyribonucleic acid
EDS	Energy Dispersive Spectroscopy
E_{ox}	Oxidation potential
E_{red}	Reduction potential
E_s	Singlet Energy

ESA	Exited-state absorption
ESI	Electrospray ionization
EtOAc	Ethyl Acetate
ETU	Energy transfer upconversion
FBS	Fetal Bovine Serum
F_{corr}	Corrected fluorescence
Fl	Fluorescence
FLX	Fleroxacin
F_{obs}	Observed fluorescence
FQ	fluoroquinolone
FQ(-F^{-})	Aryl carbene
FQ(-F)$^{\cdot\cdot+}$	Diradical anion
FQ(-F)$^{+}$	Aryl cation
HSA	Human Serum Albumin
HPLC	High Performance Liquid Chromatography
hv	Photon
IC	Internal Conversion
IC_{50}	Inhibitory concentration
ICT	Intramolecular Charge Transfer
IFE	Inner Filter Effect
ISC	Intersystem Crossing
K_a	Association constant
K_d	Diffusion rate constant
K_q	Quenching rate constant
K_{sv}	Stern-Volmer constant
LFP	Laser Flash Photolysis
LFX	Lomefloxacin
Ln^{3+}	Trivalent ions of Lanthanides
MeOH	Methanol
NIR	Near Infrared
NMR	Nuclear Magnetic Resonance
NRU	Neutral Red Uptake

OA	Oleic acid
ODE	Octadecene
PA	Photon avalanche
PAA	Poly acrylic acid
PB	Phosphate buffer
PBS	Saline Phosphate Buffer
PDT	Photodynamic therapy
Ph	Phosphorescence
PHA	Phenylalanine
PIF	Photo-Irradiation-Factor
PMT	Photomultiplier Tube
PPG	Photolabile photoprotecting group
PTFE	Polytetrafluoroethylene
PTT	Photothermic therapy
Q	Quencher
ROS	Reactive Oxygen Species
SA	Succinic acid
SD	Standard deviation
SDS	Sodium dodecyl sulphate
TEM	Transmission electron microscopy
TICT	Twisted Intramolecular Charge Transfer
Trp	Triptophan
UC	Upconversion
UCNP	Upconversion nanoparticle
UV	Ultraviolet
UVA	Ultraviolet A
UVB	Ultraviolet B
UVC	Ultraviolet C
UV-Vis	ultraviolet-visible
ΔAbsorbance	Absorbance variation
ΔG_{pet}	Gibbs free energy
λ_{max}	maximum wavelength

τ	Lifetime
τ_0	Transient species lifetime
τ_{Fl}	Fluorescence lifetime
ϕ_D	Photodegradation quantum yield
ϕ_{Fl}	Fluorescence quantum yield
ϕ_{PF}	Photoproduct formation yield
ϕ_Δ	Singlet Oxygen quantum yield

Outline

Chapter 1: Introduction

1.1. Basic concepts on photochemistry and photophysics

Molecular photochemistry is defined as the science related to the description of physical and chemical processes derived by photons absorption. A photochemical process starts with radiation absorption of chromophore groups (whose electrons are in n or pi orbital such as carbonyl or aromatic groups) inside a molecule. The absorption and emission spectra of a molecule give relevant information about the structure, energy, and dynamics of its electronic excited states. Its study may help in the comprehension and interpretation of photochemical reactivity and their photophysical properties.

A molecule, after the absorption of a photon, rises to an electronic excited state. This virtual state is unstable compared with the ground state. If the excited molecule does not change its structure, it will look for a way to lose the energy giving place to a photophysical process. The different processes which can occur can be grouped in two: photochemical and photophysical. [1]

Photochemical processes are the transformations that a molecule can suffer from its electronic excited state to give place to different structures related to its constitution or configuration compared with the ground state one.

Photophysical processes produce a change in the quantum state of the molecule with no transformation in its natural chemistry. They are transitions in which interconversion between the excited state and the

ground state are produced. These processes can be radiant or non-radiant. A radiant process implies the emission of an electromagnetic radiation from the electronic excited state to the ground state. On the other hand, in a non-radiant process, the energy is transferred to another state without any emission.

The most common radiant processes are:

- Absorption: it is characterized by a molar absorption coefficient (related to the incidence area of the chromophore and the probability to produce an absorption in a specific wavelength). The absorption is associated to electronic transitions between different energetic levels in specific groups of the molecule. They can be permitted transitions (singlet-singlet) or forbidden ones (singlet-triplet) by the spin rule.
- Fluorescence: emission permitted by the spin rule in which a deactivation of an excited specie from first singlet excited state to ground state with the emission of a photon of radiation.
- Phosphorescence: forbidden by spin rule. On it, a deactivation of an excited specie from the first triplet excited state to the ground state occurs with a photon emission.

Between the most common non-radiant processes are:

- Internal conversion (IC): permitted transitions between excited states of the same multiplicity. On it, the excited molecule goes to a higher or lower electronic state, producing a series of vibrational

relaxations without radiation emission. It is favored when the electronic states are of similar energy.

- Intersystem crossing (ISC): forbidden transitions between states of different multiplicity. As in the internal conversion, the probability of this transition is higher if the vibrational levels of both are overlapping.
- Vibrational relaxation: transmission of an excess of energy of a vibrational excited level to a lower energy vibrational level.

These processes are shown in the Jablonski diagram (Scheme 1.1). Their duration is shown in table 1.1.

Table 1.1. Characteristic times of principal photophysical processes

PHOTOPHYSICAL PROCESS	TIME (s)
Absorption	10^{-15}
Vibrational relaxation	10^{-12}-10^{-10}
Singlet excited state (S_1) lifetime	10^{-10}-10^{-7}
Internal conversion	10^{-11}-10^{-9}
Intersystem crossing	10^{-10}-10^{-8}
Triplet excited state (T_1) lifetime	10^{-6}

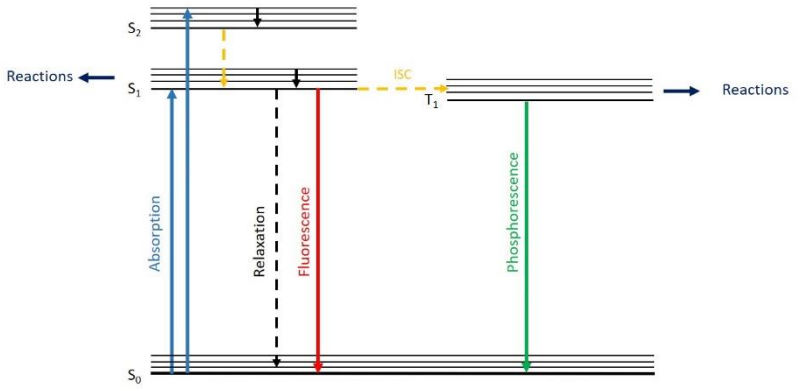

Scheme 1.1. Simplified Jablonski diagram

Narrow variations in the position and intensity of the band are related with structural changes. The study of these fluctuations helps to understand and determine the photophysical properties and the correlation between the structural characteristics and the damage caused in a biological environment.

Otherwise, when two chromophores are present in the same media (covalent bonded or not), light-induced processes can occur between them, such as energy transfer, electronic transfer, exciplex formation, proton transfer or excimer formation.

1.1.1. Photoinduced energy transfer

The energy of a donor chromophore (D*) in its excited state is transferred to an acceptor chromophore (A). In that moment, the deactivation of the donor (D) to the ground state and excitation of the acceptor (A*) take place.

For this process to occur, the energy of the excited state of the donor may be higher than the acceptor one (Eq 1.1). In addition, the donor needs a higher enough lifetime to react.

$$\Delta G = E^*_D - E^*_A \qquad \text{Eq. 1.1}$$

where ΔG is the variation of the free Gibbs energy of the process; E^*_D is the energy of the donor excited state and E^*_A the acceptor excited state energy. [2]

1.1.2. Photoinduced electron transfer

Usually, an electron transfer process takes place when a molecule in its excited state gives an electron to other molecule in the ground state.

The thermodynamics of this processes can be determined by the Rehm-Weller equation (equation 1.2).

$$\Delta G = E_{ox} - E_{red} - E_{0\text{-}0} + C \qquad \text{Eq. 1.2}$$

where ΔG is the variation in the Gibbs free energy of the process, E_{ox} and E_{red} are the oxidation and reduction potential respectively in the ground state of donor and acceptor, $E_{0\text{-}0}$ is the energy of the involved excited state and C is the coulombic term which considers the stabilization of the generated species in the used solvent. [3]

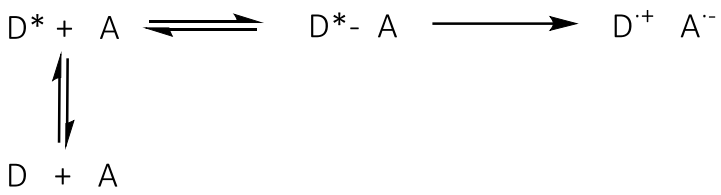

Scheme 1.6. Electron transfer mechanism

1.2. Cancer treatments nowadays

Cancer is among the leading causes of deaths worldwide[4] and it is mainly associated with ageing of population and lifestyle.[5] Over the next 20 years, the number of new cases is projected to increase by about 70%.[6] Surgery, radiotherapy and chemotherapy are the most common types of treatments available nowadays. The use of chemotherapy for treating cancer began in the 1930s. Discovered and named by Paul Ehrlich, a German scientist with particular interest in alkylating agents. From World War II, nitrogen mustard began to be used as the first chemotherapy after the exposure of soldiers to it showed decreased levels of leukocytes.[7] A reduction in the electrophilicity was necessary in order to reduce its toxicity. First of all, aliphatic mustards were developed and then, in the 1950s alkylating drugs appear providing a slower reactivity with the DNA. In 1953 Chlorambucil was synthesized by Everett et al. It is a bifunctional alkylating agent with activity against human neoplastic diseases. Chlorambucil is still used in several cancer such as Chronic lymphocytic leukaemia (CLL), Hodgkin lymphoma and non-Hodgkin lymphoma. At

that time, monotherapy drugs only achieved brief responses in some types of cancer.[8]

The beginning of the 20th century had a major limitation in the drug discovery. It was the development of models able to discern which chemicals have anticancer activity in humans.[9]

In the 1960s surgery and radiotherapy were the basis for solid tumour treatment but this leads in a curability plateau due to uncontrolled micrometastases. Adjuvant therapies arise as the first multimodality treatment with the combination of chemotherapy with radiotherapy or surgery. This strategy is still used today for numerous types of tumours.[7]

The quick development in the 1970s of the understanding of molecular changes in cancer cells increased the number of drugs with different mechanisms of action during the 1980s. This knowledge led to liposomal therapies to reduce side effects such as cardiotoxicity. With this technique the drug is placed inside vesicles made of lipid bilayers. This technique could be considered as the first steps in nanotechnology-based approaches.

Another used strategy has been the use of drugs which were designed for other purposes such as antibacterial agents. Two of them have been studied in this thesis. The first one is the colchicine. It is an alkaloid compound that can be found most abundantly in *Colchicum autumnale*. Since Egyptian times it has been used to treat gouty arthritis. Due to its side effects and high toxicity, it is not until 2009 when FDA approved it controlling strictly the dose.

Image 1.1. *Colchicum autumnale*

The other ones are fluoroquinolones. They arise from the widely studied family of the quinolones. They were usually used as antibacterial agents and tuberculosis treatment.

As shown, massive efforts have been made to understand the cancer biology, but it has been slowly translated into significant improvements in cancer care.[10] Lack of water solubility, nonspecific biodistribution and targeting, poor oral bioability and toxic side effects among others are the major limitations of conventional drug delivery systems. That is the reason why new types of treatment are emerging.

One example of new treatment is the immunotherapy which is based on the use of immune system components such as antibodies,

dendritic cells… to treat diseases. It is not only used for cancer but also allergies or autoimmune diseases among others.[7] The aim of immunotherapy in cancer is to kill tumour cells or give the immune system the power to destroy tumours. Immunotherapy drugs have been approved; however, they are not widely used as chemotherapy, radiotherapy, or surgery.

Other treatments which are arising nowadays are targeted therapy (based on small-molecule drugs or monoclonal antibodies), hormone therapy (can be used as neo-adjuvant and/or adjuvant therapy) and stem cell transplant (restoring blood-forming stem cells after certain cancer treatments).[11]

Another example of cancer treatment still growing is nanomedicine. It is based on nanoscale materials providing the opportunity to reduce the mentioned side effects of nowadays treatments.[11] This treatment includes a great variety of techniques that will be explained in detail in the next section.

Since the beginning of the history of medicine, light has been used as a way of treatment. It has to do with the extraordinary connection between light and biology. Plants are a clear example of that relation with their sophisticated energy-harvesting machinery able to convert solar energy into chemical energy. That is the reason why light has played an important role since the very beginning of the medicine. And it is still in continuous study with new ways of treatment with known or

new drugs and with new techniques such as light induced controlled drug delivery.

1.3. Nanomedicine

Nanotechnology can be defined as the use of materials between 1 and 100 nm.[12] When nanomaterials are applied in medicine it is known as nanomedicine and involves the use of engineered materials in the nanoscale to develop new treatments.

Main characteristics of nanocarriers are their high surface-to-volume ratio, better reach to tumour tissue and controlled drug release.[10] Nanoparticles may reduce problems related to poor water solubility and stability of drugs by caging them into a hydrophilic nanocarrier. Besides, better biodistribution and targeting are achieved by constructing specific nanocompounds.[13] In addition, biodegradation or excretion of the drug may be avoided by encapsulation. Finally, tumour resistance can be reduced due to targeted nanocarriers.[14]

An extensive range of nanomaterials have been developed as therapeutics either for cancer or other diseases. In agreement with the registry made by clinicaltrials.gov, a total of 1239 nanomedicine formulations have been registered as treatments by January 2020. As many as 939 of these are in the field of cancer therapy.[15]

1.3.1. Viral Nanoparticles

Natural mechanism of action of viruses is based on host's immune system invasion to ensure their own reproduction.[16] Taking advantage of this statement, virus-like nanoparticles have emerged as a new immunotherapy tool able to express therapeutic proteins.[17] In comparison to synthetic nanoparticles they are biocompatible and can be produced in large quantities in a very cheap manner. Plant-virus based nanoparticles have been the focus of researchers trying to minimize the chance of the virus to be infectious.[18] In addition, they can be used as reaction container or drug capsule because of their self-assemble property.[19,20] The main challenge is to evade the immune system response

1.3.2. Organic nanoparticles

At the present, natural or synthetic compounds are considered as organic nanocarriers.[10] There are many different types of organic nanocarriers, some of which will be described here.

1.3.2.1. Drug conjugates

Considered nowadays as one of the most successful nanomedicine therapeutics in clinical cancer. Their nanometric size and their conjugation to active pharmaceutical ingredients are the main reasons to consider drug conjugates as nanotherapeutics.[21,22]

1.3.2.2. Lipid-based nanocarriers

Liposome-based nanoparticles are created when an amphiphilic lipid is added to a hydrophilic liquid via lipid bilayers obtaining a spherical particle around 50 to 500 nm.[4] An advantage of these materials is the possibility to carry molecules which usually have problems like lack of hydrophilicity or negative charges.[23] In addition, they can respond to different stimuli such as pH, enzymes, temperature, or light. Molecules can be loaded in the aqueous area or in the middle of the lipid layer depending on its polarity changing the pharmacokinetics of the drug and reducing its side effects.[4]

1.3.2.3. Polymer-based nanocarriers

Polymeric nanoparticles can be prepared from synthetic or natural polymers.[10] They are usually spherical and solid. Many different drugs can be loaded in this type of nanoparticles, e.g., peptides, vaccines, or hydrophilic and hydrophobic drugs.[23] One of their main advantages is that they provide stability to labile molecules such as proteins.[24]

1.3.3. Inorganic nanoparticles

Different materials are included under this category. Gold and silver nanoparticles have special applications in surface plasmon resonance analysis. Gold nanoparticles serve as drug release material controlled by different stimuli.[25] In contrast, silver nanoparticles act as antimicrobial agents.[26]

Silica and porous silica nanoparticles have been studied for different applications such as therapy, diagnostic and drug delivery.[27,28]

Quantum dots are metallic particles made of semiconductor atoms like CdSe, ZnO or GaAs among others. Thanks to their optical characteristics they are good option for biomedical diagnostics and imaging.[29,30]

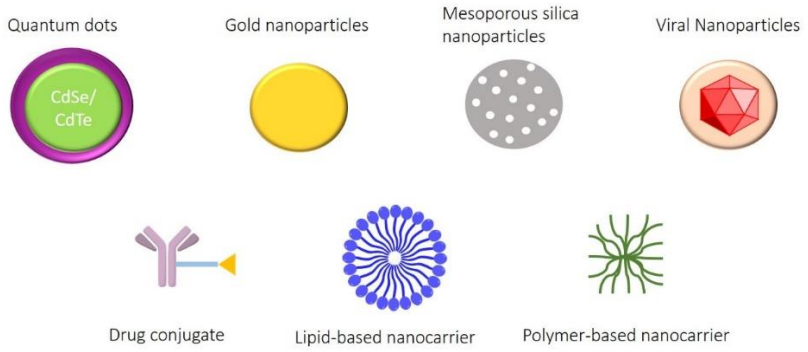

Figure 1.2. Examples of some nanocarriers

1.4. Upconversion nanoparticles

Upconversion nanoparticles (UCNP) are generally composed by an inorganic matrix with appropriated dielectric host lattice (e.g., $NaYF_4$) and optical inert lanthanides (e.g., Y), and doped with trivalent rare-earth ions (Ln^{3+}, e.g., Yb^{3+}, Er^{3+}, Tm^{3+}) achieving unique luminescent characteristics. They are usually codoped with a Ln^{3+} able to absorb light (sensitizer) and another one which emits light (activator).[31–33] It is known as anti-Stokes process in which two or more low energy photons (NIR range) are absorbed first by the sensitizer and then by the activator

emitting a higher energy photon (UV-Visible range).[34,35] The main characteristic is that those photons are absorbed by real energy states compared with the virtual energy states needed in Quantum dots or other nanoparticles.[36] In addition, the shielding of the intra f-f electron transitions by outer complete 5s and 5p electron shells provides high resistance to both photobleaching and photochemical degradation.[37,38] The electronic configuration of each lanthanide is unique and it is usually insensitive to inorganic host lattice, nanoparticle size and shape. It can be traduced into a system of well-defined, ladder-like energy levels.[33,38]

Thanks to their unique optic properties like high relation signal/noise, low toxicity and higher penetration in tissues, UCNP are gaining importance for biomedical applications such as photodynamic therapy, bioimaging[39] or controlled drug release[40] and in other areas away from medicine like laser design, sensors[41] or solar cells. [42–46]

1.4.1. Upconversion processes

Upconversion processes are a great method to produce visible light after NIR excitation. Trivalent ions of lanthanides (Ln^{3+}) have unique properties thanks to which these types of emission are possible. Ln^{3+} ions have their 4f electronic orbitals partially full ($4f^n5s^25p^6$, n= 0-14). The coupling of the electrons in $4f^n$ orbitals with electrons of the completed orbitals $5s^2$ and $5p^6$ results in 4f-4f transitions. If the ions are placed in static crystallin grid, these transitions become partially permitted.

Several pathways are possible for the UC emission, after sequential absorption of two or more photons in NIR, due to great number of energetic levels of the lanthanides.

There are five basic upconversion mechanisms encompassing excited-state absorption (ESA), energy transfer upconversion (ETU), photon avalanche (PA), cooperative sensitization upconversion (CSU) and cross relaxation (CR), although ETU is the most competitive for UCNP processes.[37,47–51] Those three are discussed below.

1.4.1.1. Excited-state absorption (ESA)

High photon density, low ion concentration, avoiding cross relaxation, and large absorption efficient section are needed to facilitate ESA process.[31] A single ion with multiple energy levels is able to absorb two successive photons due to the ladder-like structure of the system (see Figure 1.3). First of all, a photon is absorbed and a transition from ground state (G) to the intermediate exited state (E1) takes place. A second photon can be absorbed occurring the transition between E1 to a more energetic excited state (E2). The emission takes place with the relaxation from E2 to F.[52] An efficient ESA is achieved only when a ladder-like structure of the energy states exists. Only a few lanthanide ions such as Tm^{3+}, Ho^{3+}, Er^{3+} have such arrangement.[37]

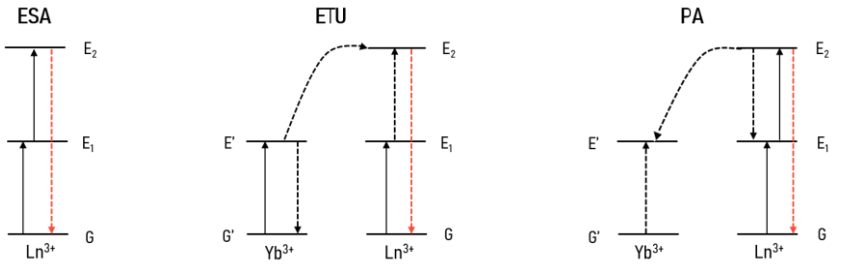

Figure 1.3. Principal UC emission processes for lanthanide-doped UCNP: exited-state absorption (ESA), energy transfer upconversion (ETU), photon avalanche (PA). Yb^{3+} activator and Ln^{3+} sensitizer. Excitation (continuous line), energy transfer (dashed line) and emission (red dashed line).

1.4.1.2. Energy transfer upconversion (ETU)

ETU is considered the most efficient upconversion process and the most observed in UCNP. It involves two neighboring lanthanide ions Ln^{3+} which are known as sensitizer an activator (see Figure 1.3). The absorption effective section of the sensitizer needs to be higher than that of the activator. Both, sensitizer and activator can absorb a photon thereby promoting their respective excited states (E' and E_1, respectively). The sensitizer successively transfers its energy by non-radiative process to the activator, relaxing to its ground-state F'. The activator reaches its upper excited state E_2 from which emission due to transition $E_2 \rightarrow F$ occurs. This process is highly dependent on the distance between ions.[38,53]

1.4.1.3. Photon avalanche (PA)

Photon avalanche is an UC which needs high excitation power to occur. The process starts with population of level E_1 by non-resonant GSA, followed by resonant ESA to populate the higher energy level E_2. Cross-relaxation energy transfer between the excited state and F' of the neighbor ion results in the population of E_1. Both ions easily populate E_2 to further initiate cross-relaxation and exponentially increase level E_2 population by ESA, producing strong UC emission as an avalanche process.[37,54] PA usually occurs in systems with high dopant concentration and enormous excitation power where the intermediate energy levels act as energy reservoir.[38,54,55]

UCNP nowadays are mostly based on ETU due to their higher efficiency. As previously discussed, this process needs an activator and a sensitizer. In this case, the most studied ones will be shown, with Yb^{3+} as an activator and Er^{3+} or Tm^{3+}as sensitizers.[31]

On one hand, in a matrix doped with Yb and Er, emissions in the violet (415 nm), the green (525nm, $^2H_{11} \rightarrow {}^4I_{15/2}$ and 542 nm, $^2S_{1/2} \rightarrow {}^4I_{15/2}$) and the red (655 nm, $^4F_{9/2} \rightarrow {}^4I_{15/2}$) (see Figure 1.4) are observed. In the case of the emission in green and red the processes are biphotonic and for violet it is attributed to a triphotonic process. On the other hand, a matrix doped with Yb and Tm shows emission in UV (362 nm), visible (450, 475 and 644 nm) and NIR (800 nm). In this case the UC emission involves more than two photons due to their higher distance between energetic levels (see Figure 1.4). In the case of the Er^{3+}, the higher energetic levels are closer. The 362 ($^1D_2 \rightarrow {}^3H_6$) and 450

nm ($^1G_4 \rightarrow {}^3F_4$) emissions require four photons. For those at 475 ($^1G_4 \rightarrow {}^3H_6$) and 644 nm ($^1G_4 \rightarrow {}^3F_4$), 3 photons are needed and, for the emission at 800 nm ($^3H_4 \rightarrow {}^3H_6$), only two.[31]

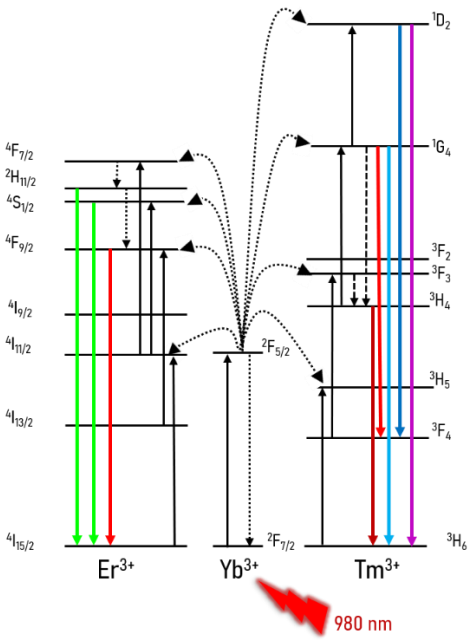

Figure 1.4. Scheme of ETU mechanisms in a matrix doped with Yb/Er or Yb/Tm. Colored arrows correspond to the emission. Dashed arrows represent transfer energy process or relaxation. Black continuous arrows mean excitation process.

1.4.2. UCNP composition

As previously mentioned, 4f-4f transitions are partially permitted when lanthanides are in a crystalline matrix.[56] Different hosts have different coordination number and distances between dopants and, thus, different energy transfer efficiency.[31]

The organic matrix should be selected depending on the desired optical properties and different parameters must be considered: a) transparency of the matrix in the spectral range of interest, b) high optical damage threshold, c) great chemical and thermal stability, d) high tolerance to Ln^{3+} luminescent and e) low phonon energy to prevent movement generated by the oscillation of the crystal lattice thus reducing non-radiative relaxation of the Ln^{3+} luminescent centers and maximizing the radiative emission.[31,38,54]

Different materials have been studied as matrix like vanadates (e.g. YVO_4, phonon energy ~890 cm^{-1})[57], oxides (e.g., Y_2O_3, phonon energy ~550 cm^{-1})[58], fluorides (e.g., $NaYF_4$ phonon energy ~350 cm^{-1})[59] or heavy halides like chlorides, bromides or iodides (phonon energy less than 300 cm^{-1}). An advantage of the oxides is their high chemical stability but they have high phonon energy. In contrast, heavy halides have low phonon energy but they are hygroscopic and are use-limited.[54] That is the reason why fluoride materials are the most used as matrix, in particular $NaYF_4$. At the same time, the crystal field of the matrix has a strong influence on the optical properties.[38] $NaYF_4$ matrix has two different crystalline phases, hexagonal and cubic. The cubic phase (α-$NaYF_4$) is less thermodynamically stable than the hexagonal (β- $NaYF_4$) one, being the emission of β-$NaYF_4$ around 10 times higher.[55]

1.4.3. UCNP synthesis

The design of synthetic routs for the obtention of UCNP is crucial to control the form, size, composition, and crystalline phase. To obtain small size distribution, best strategy is bottom up. There are different methods but all of them are made with colloidal solutions which allow the control of size and shape of the nanoparticles.

Several methods are established for the bottom-up strategy like coprecipitation, hydro(solvo)thermal, thermal decomposition, Ostwald-Ripening among others.[38,54,55,60]

Due to the large number of existing UCNPs, only the $NaYF_4$ matrix and the synthesis methods most used today will be explained.

1.4.3.1. Coprecipitation

Yi et al. [61] were the first to use this method which is one of the easiest procedures to obtain monodispersed NPs. At the beginning, UCNP were obtained with a shell of ethylendiaminotetraacetic (EDTA). The control of the size is difficult with this covering, so other coverings like polyethyleneimine (PEI) or polivinylpirrolidone (PVP) have been proposed [62]

Even so, UCNP obtained by coprecipitation have low luminescence and they also need high temperatures (400-600°C) to obtain β phase.[61]

1.4.3.2. Thermal decomposition

This method is about the use of organometallic precursors of the lanthanides, like trifluoroacetates, achieving high temperatures (~ 300°C) with octadecene (ODE) as organic solvent with high boiling point and oleic acid (OA) as organic ligand.[63]

With this method, high crystallinity, monodispersed, and high luminescent UCNP are obtained.[54]

1.4.3.3. Hydro(solvo)thermal

In this method lower temperatures are needed (> 250°C) but in contrast, pressure needs to be high. To achieve these conditions an autoclave is necessary. The method starts from nitrates ($Ln(NO_3)_3$ precursors in polar solvents. In this case, the F^- source is NH_4F_2. The duration of the synthesis goes from 12 to 24 h depending on the desired size. One of the main advantages of this method is that there are no toxic subproducts produced during the process. With the change of the surfactant, the solvent or the reaction time it is possible to control the size of the UCNPs.[64]

1.4.3.4. Ostwald-ripening

The beginning of this synthesis is $LnCl_3$ with OA as ligand and ODE as solvent.[65] The controlled addition of a solution with stoichiometric quantities of sodium and fluor allows the formation of nucleus of $NaYF_4$ stabilized by OA. Afterwards, an increase of the temperature until ~ 300°C leads to the uniform growth of crystalline nanoparticles.[66]

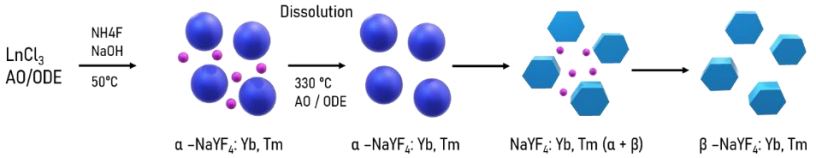

Figure 1.5. Growth stages of β-$NaYF_4$:Yb^{3+}/Tm^{3+}.

The particles with less surface/volume ratio (that is the bigger ones) are energetically favored over the smaller nanoparticles (less stable).[67] This is known as Ostwald ripening process.

Drop by drop addition of fluor and sodium precursors allows the spatial separation of the nucleation and the crystal growth.[68] The control of the temperature and reaction time, in addition to the variation of the OA/ODE ratio allow the obtention of monodisperse β phase crystalline nanoparticles with different sizes (Figure 1.5).[65]

This method does not generate toxic subproducts, it needs shorter reaction time and milder reaction conditions.[69] In conclusion, it is considered as the best procedure to obtain monodispersed UCNP with uniform size and one crystalline phase.[70] For all these reasons, the Ostwald ripening method is the selected for the development of this thesis.

1.4.4. UCNP biomedical applications

1.4.4.1. Bioimage

The visualization of biological samples to obtain information about anatomy, morphology and physiology is really important in

biomedicine. It leads to earlier detection and screening of diseases.[71] As mentioned before, NIR light has higher penetration into tissues and, moreover, it prevents the autofluorescence of the samples and the light scattering.[44,72] In addition, NIR light has excellent optical and chemical properties. All these characteristics make UCNP a great alternative for UV-visible fluorophores and quantum dots.[71,73] Despite these advantages, overcoming the high excitation density required for UCNP processes is costly and limits its applications.[71,74]

Due to the great variety of UCNP, they can be applied in a vast number of bioimaging techniques such as fluorescence, ultrasounds or X-ray among others.[31,45,72,75]

1.4.4.2. Biosensing and bioassay

Detection of different molecular targets or biomolecules play a key role in monitoring physiological processes which are fundamental and play vital roles. The main advantage of UCNP systems for biosensing is the high sensitivity at deep locations.[76] UCNP are not used by themselves, apart from temperature sensing, because they need to be combined with recognition elements such as an antibody or an enzyme. The UCNP act as the transducer of the recognition into an optical signal.[43] There are different types of biosensing:

- Temperature sensing.[77]
- Detection of small gas molecules such as ammonia or carbon dioxide.[78]

- Ions sensing like mercury. [78]
- Biomolecules detection or bioassays[76]

1.4.4.3. Therapy

UCNP are useful as therapeutic agents, in special against cancer. There are different types of treatment with these nanoparticles:

- Photodynamic therapy (PDT): consists in the generation of reactive oxygen species (ROS) through photosensitizer activation by light. Different organic molecules as for example methylene blue or chlorin e6 are able to generate ROS, more specifically singlet oxygen, after NIR excitation.[79]
- Photothermic therapy (PTT): UCNP functionalized with photothermic agents like gold or silver nanoparticles. The temperature increase causes cell damage.[80]
- The chemotherapy based on UCNP has two different aspects: the bioimage guided therapy and the controlled drug delivery by light.[81]

1.5. Drugs for photosensitized reactions

The exposure of a patient to solar light during a treatment with some drugs can produce a phototoxic reaction which will be presented as an erythema. Some examples of photosensitizing drugs are antibiotics such as tetracyclines or fluoroquinolones, nonsteroidal anti-inflammatory drugs like ibuprofen or targeted therapies such as Imatinib, among others. Those photosensitizing properties can be used for therapeutic purposes.

There are two types of principal photosensitized reactions. The first one is the photoallergy. It occurs as a result of an immune system response to an antigen produced in the skin after exposure of a photosensitizing substance to solar radiation. It only occurs in some people.[82] On the other hand, phototoxicity can occur which, will be produced in every person who receives a chemical substance in sufficient dose and appropriate radiation exposure. This last type of photosensitization can be used as therapeutic strategy and is going to be explained below.

1.5.1. Photosensitization mechanism

The transitory species generated by the interaction light-drug (singlet and triplet excited states as well as intermediate reagents) can react with biomolecules through two different mechanisms [83]:

i. Type I: the excited states or intermediate reagents of the drug can generate charge, hydrogen or energy transfer processes with biomolecules bringing about different types of lesions.
ii. Type II: an energy transfer from excited state of the drug to the molecular oxygen occurs, generating singlet oxygen ($^1O_2$). This oxidant reagent reacts with numerous biological molecules. It only will occur when the energy of the excited state is greater than that of the singlet oxygen and its lifetime is long enough to react.

1.5.2. Light

The solar radiation which reaches the earth is composed of wavelengths comprised between 290 and 5000 nm. The stratospheric ozone layer blocks the most dangerous wavelengths (UV-C). The radiation energy is composed by 56% of infrared rays (800-5000 nm), 39% of visible light (400 nm – 800 nm) and 5% of ultraviolet radiation (UV) (290 nm – 400 nm). The latter is divided in:

i. UVA (320 nm – 400 nm) which constitutes 98% of the UV rays that penetrate glass and epidermis.
ii. UVB (290 nm – 320 nm) represents 2% of UV rays and are blocked by glass and epidermis.
iii. UVC (100 nm – 290 nm) is absorbed by the ozone layer and does not reach the earth. [84]

Proteins and nucleic acids are able to absorb UVB light directly. However, UVA can result dangerous when photosensitizing molecules are present. They are able to modify molecules.

Ultraviolet light has several drawbacks that make it not the best option for non-skin treatments. Its greatest limitation is the low penetration into the tissues. This is due to the scattering absorption of UV light by water and biological substances.[85] Taking this drawback into account, treatments that require light on internal tissues will not be possible with UV light. In contrast, near-infrared light (NIR) can penetrate deeply into tissues making it a god option to consider for light treatments.

1.5.3. Fluoroquinolones

Fluoroquinolones are part of a big family known as quinolones. They are synthetic antimicrobial compounds with bactericidal action that first appeared in 1962. Quinolones have a basic structure, 4-quinolin acid, 3-carboxilic (4-quinolone).[86] The low number of bacteria on which they could act at the beginning drove the synthesis to the addition of a piperazine ring in carbon 7 enhancing their activity against gram (-) bacteria and some gram (+). The piperazine ring enhanced the penetration power across the bacteria cellular wall. They were used until the end of 70's when greater changes in the structural composition were made in order to increase the activity and the action spectrum.

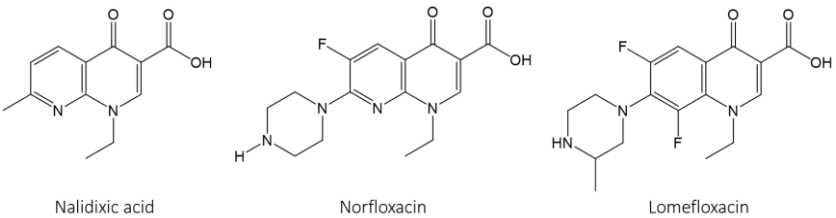

Figure 1.6. Examples of first, second and third generation FQ respectively.

One of those bigger changes was the addition of a fluorine atom in position 6 giving rise to second generation quinolones or fluoroquinolones.[87]

The relation between the biological activity and the chemical structure of these molecules motivated the synthesis of compounds with new substituents trying to increase the efficiency, power, and action spectrum and, in addition, decrease their side effects. In that sense, third generation quinolones appeared with longer plasma half life and antibacterial power against gram (+). They are di or trifluorinated compounds.

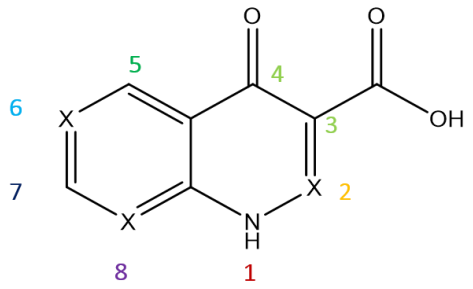

1. Influence over power and pharmacokinetics
2. No properties alteration
3 and 4. Essential for gyrase binding and membrane transport
5. Gram (+) and (-) bacteria activity enhancement
6. When X=C-F, control of gyrase and antibacterial power
7. Influence over action spectrum, power and pharmacokinetics
8. Pharmacokinetics control

Figure 1.7. Relation between structure and pharmacological properties

1.5.3.1. Fluoroquinolones' mechanism of action

Quinolones are the only known antibacterial compounds that act against bacterial topoisomerases II and IV. These enzymes are responsible for adequate coiling in chromosomic regions. Quinolones inhibit the activity of DNA-gyrase avoiding DNA reparation and recovery of its supercoiled form ending the cellular division.

The mechanism of action proceeds through the formation of a quinolone-enzyme-DNA complex. The binding of the quinolones to the enzyme induces a conformational change in the enzyme-DNA complex.[88]

Several studies have been carried out evidencing the antitumoral activity of fluoroquinolones. Depending on the FQ the mechanism of action is different.

- Cell cycle arrest inducers: ciprofloxacin is an example that produce phase arrest in S/G2 phase in prostate and bladder cancer cells.[89,90] Another strategy to produce cell cycle arrest is the inhibition of involved enzymes like cyclin-dependent kinases Miofloxacin in pancreatic cells.[90]
- Apoptotic agents: cancer is sometimes a consequence of non-regulated apoptosis. The lack of apoptosis is translated to tumor formation, metastasis and even drug resistance.[91] Some examples of FQs which have apoptotic effects are norfloxacin. Perucca et al.

showed that exposure of Ciprofloxacin and Levofloxacin to UVA light leads to apoptosis.[92]

- Adjuvant chemotherapy enhancers: combinatorial administration of anti-cancer drugs is highly effective due to the different mechanisms of action of co-administered drugs. An example of combination drugs is Enoxacin (FQ) and Doxorubicin.[93]

1.5.3.2. Fluoroquinolones' photogenotoxicity

In the presence of ultraviolet radiation (UV) fluoroquinolones reveal an enhancement of its genotoxicity in eukaryotic systems. Previous studies unveil that photoactive FQs experience a photodehalogenation by heterolysis of their C8-halogen bond producing reactive intermediates which produce biological damage. [94]

1.6. Photosensitized release

Conventional drug delivery systems have certain drawbacks such as the lack of control in the distribution of the therapeutic agent and the low concentration at the target site. Associated with these problems are the efficiency and toxicity of the drug. All these drawbacks translate into side effects in the patient.[95]

Nanomedicine has appeared as a promising option to overcome such differences. The base behind this option is the use of nanoparticles as therapeutic carriers achieving higher drug solubility and circulation

time and decreasing side effects by delivering the drugs in target sites.[96–98]

The effect known as enhanced permeation and retention (EPR) can be achieved by synthesizing nanoparticles with sizes between ~30 nm and 200 nm which will accumulate preferentially in tissues with deficient vasculatures such as the tumor ones.[99] It can lead to an enhancement of the therapeutic effect.

Different sources for external trigger can be used as energy ones such as magnetic [100] fields, ultrasound [101] or light.[102] As mentioned before, light has been used in many different ways in medicine from photosensitizing to therapeutic use itself like photodynamic therapy (PDT). Centering the attention in the photochemical reactions, they need high energy emitting from UV/visible wavelength to occur. Nevertheless, it has poor penetration tissue depth and causes cell damage by reaction with biomolecules. In contrast, NIR light overcomes those problems but it usually has low energy to produce photochemical reactions. Up-conversion nanoparticles are able to mix the best of both radiations. They can absorb NIR light and emit UV/visible light avoiding the problems of tissue penetration and cell damage from UV light and the low energy of NIR light.[103,104]

1.6.1. Loaded drugs

Conformational changes in the carriers after NIR irradiation leads to drug delivery. Different techniques have emerged for physical loading.

Two examples of those techniques are the drug loading in mesoporous silica by hydrogen bond interactions or prodrug load in mesoporous silica. Not only drugs can be loaded, but also other molecules such as siRNA or bioimaging dyes.

1.6.2. Conjugated drugs

One way to achieve drug delivery from UCNP is the direct conjugation of the therapeutic molecule to the nanoparticle surface[105]. Another way is the use of photocleavable prodrugs.[106,107] These prodrugs are composed by the therapeutical agent and a photocleavable protecting group (PPGs). PPGs have been used with other purposes apart from drug delivery such as volatiles release [108,109] or polymerization, among others.[110,111] A good PPG may have some special characteristics like a high quantum yield to have a clean and efficient photoreaction. In addition, if during the photochemical reaction side products are generated, they should not react with the studied media and they should not absorb in the working wavelength in order to avoid competitive absorption.

The first and more used PPGs are the nitroaryl compounds, but their photolysis generates toxic photoproducts with high absorption in the working range. For that reason, several PPGs have been developed during the last decades. Some examples of PGGs are the metal-containing groups, coumarin-4-ylmethyl groups, arylmethyl groups and

the arylcarbonylmethyl group, among others.[112] In this section coumarin and nitrobenzyl groups will be described.

1.6.2.1. Coumarin-4-ylmethyl groups

First coumarins used as PPGs were 7-methoxycoumarinyl-4-methyl and they were the base for new cages. Variations in their maximum absorption can be achieved by modifying C6 and C7.[112] Regardless, low water solubility still remains unresolved in this first generation coumarins. The addition of an alkoxy group in C6 contributes to a red shifting of the absorption maximum. Second generation coumarinylmethyl cages achieves better photochemical and spectroscopic properties and, moreover, shifts the absorption maxima until 350-400 nm by adding 7-amino substituents.[113] In order to solve the water solubility problem, which is really important for biological applications, different polar groups such as carboxylic acids have been added.

The photorelease mechanism depends on the selected leaving group. In the case of alcohols, thiols and phenols, the derivatives render resistant to heterolysis. The best strategy is the use of a carbonate linkage.

Amines proceed with a slow rate.[114–117] As shown un Figure 1.8, decarboxylation of carbamate anion is the rate-limiting point. It will be dependent on the released amine and the pH.[118,119] This slow release is a disadvantage if the process needs a rapid substrate release.

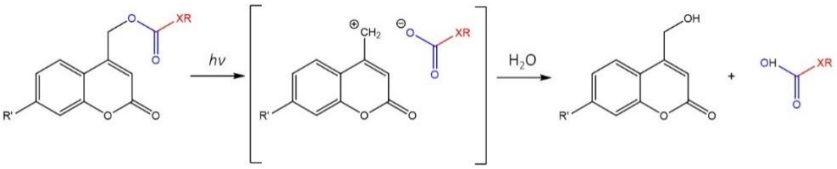

Figure.1.8. Photorelease of thiols, amines, and alcohols

The most successful leaving groups are carboxylic acids, sulfonates and phosphonates. After irradiation, consequent absorption, and relaxation to lowest singlet excited state, three different options may occur:

- Radiationless decay
- Fluorescence
- Heterolytic bond cleavage

The intermediate formed at the beginning by tight ion pair is the key. Coumarin-methyl cation reacts with solvent or nucleophiles to yield a stable product. On the other hand, tight ion pair can escape the cage and react with nucleophiles. After the recombination of the ion pair, the caged derivative comes back to the ground state via nonproductive pathway.[120–122]

Even though the heterolytic bond cleavage rate constant for these cases is very fast, ion pair recombination is quicker. The addition of electron-donor groups in the coumarin derivatives and selection of leaving groups with low pK_a favours the reaction and avoid the ion pair recombination.

1.6.2.2. *Orto*-Nitrobenzyl groups

Despite their disadvantages, o-nitrobenzyl groups have been widely used as PPGs. The changes in their substituents are crucial for the chromophore absorption spectrum and, in addition, for the stability of the photocleavable bond. Minor changes create PPGs able to photocleavage at different wavelengths (from 345 to 420 nm).[113,123,132–134,124–131]

The addition of an electron-withdrawing group at *para*-position is an easy way to obtain a red shifted absorption. Moreover, the change in *meta*-position by the addition of an electron-donating group allows longer wavelength cleavage.[125–127,131,133]

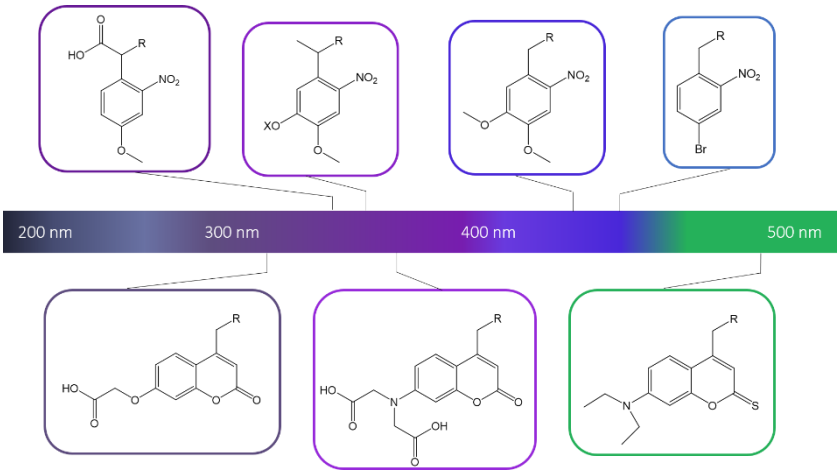

Figure 1.9. *Ortho*-nitrobenzyl and coumarin-4-ylmethyl derivatives and their wavelength

After irradiation, hydrogen abstraction by nitro group occurs.[135] Either from singlet or triplet, the return to the ground state takes place via π-electron reorganization forming the *aci*-nitro intermediate (see figure 1.9). This process is faster than the intramolecular back-reaction. When *o*-nitrobenzyl derivatives carries a leaving group at benzylic position, the photoliberation reaction takes place via *aci*-nitro intermediates. Decay of these intermediates strongly depends on the substituents, the solvent, and the pH. The direct attachment of alcohols and amines is possible but the use of carbonic derivatives, which make them a better leaving group is more frequent.[136,137]

1.7. References

1. Turro NJ. *Modern Molecular Photochemistry*. University Science Book, 1991.
2. Speiser S. *Photophysics and Mechanisms of Intramolecular Electronic Energy Transfer in Bichromophoric Molecular Systems: Solution and Supersonic Jet Studies*. American Chemical Society ; 1996. doi:10.1021/CR941193+
3. Rehm D, Weller A. Kinetics of Fluorescence Quenching by Electron and H-Atom Transfer. *Isr J Chem*. 1970;8(2):259-271.
4. Tran S, DeGiovanni P-J, Piel B, Rai P. Cancer nanomedicine: a review of recent success in drug delivery. *Clin Transl Med*. 2017;6(1).
5. Urruticoechea A, Alemany R, Balart J, Villanueva A, Vinals F, Capella G. Recent Advances in Cancer Therapy: An Overview. *Curr Pharm Des*. 2009;16(1):3-10.
6. Siegel RL, Fedewa SA, Anderson WF, et al. Colorectal Cancer Incidence Patterns in the United States, 1974-2013. *J Natl Cancer Inst*. 2017;109(8).

7. Arruebo M, Vilaboa N, Sáez-Gutierrez B, et al. Assessment of the evolution of cancer treatment therapies. *Cancers (Basel)*. 2011;3(3):3279-3330.
8. GILMAN A. Therapeutic applications of chemical warfare agents. *Fed Proc*. 1946;5:285-292.
9. DeVita VT, Chu E. A history of cancer chemotherapy. *Cancer Res*. 2008;68(21):8643-8653.
10. Wicki A, Witzigmann D, Balasubramanian V, Huwyler J. Nanomedicine in cancer therapy: Challenges, opportunities, and clinical applications. *J Control Release*. 2015;200:138-157.
11. Types of Cancer Treatment - National Cancer Institute. https://www.cancer.gov/about-cancer/treatment/types.
12. Bhushan B. Introduction to Nanotechnology. In: *Springer Handbook of Nanotechnology*. Berlin, Heidelberg: Springer Berlin Heidelberg; 2010:1-13.
13. Lammers T, Kiessling F, Hennink WE, Storm G. Drug targeting to tumors: Principles, pitfalls and (pre-) clinical progress. *J Control Release*. 2012;161(2):175-187.
14. Hu C-M, Zhang L. Therapeutic Nanoparticles to Combat Cancer Drug Resistance. *Curr Drug Metab*. 2010;10(8):836-841.
15. Home - ClinicalTrials.gov. https://clinicaltrials.gov/ct2/home.
16. Shoeb E, Hefferon K. Future of cancer immunotherapy using plant virus-based nanoparticles. *Futur Sci OA*. 2019;5(7).
17. Franzen S, Lommel SA. Targeting cancer with 'smart bombs': equipping plant virus nanoparticles for a 'seek and destroy' mission. *Nanomedicine*. 2009;4(5):575-588.
18. Aa A, Phd A. *Viral Nanoparticles: A Drug Delivery Platform*. Vol 1. Pulsus Group; 2018.
19. Leung RLC, Robinson MDM, Ajabali AAA, et al. Monitoring the Disassembly of Virus-like Particles by 19F-NMR. *J Am Chem Soc*. 2017;139(15):5277-5280.
20. Cuervo A, Daudén MI, Carrascosa JL. Nucleic acid packaging in viruses. *Subcell Biochem*. 2013;68:361-394.

21. Duncan R. Polymer conjugates as anticancer nanomedicines. *Nat Rev Cancer*. 2006;6(9):688-701.
22. Hawe A, Hulse WL, Jiskoot W, Forbes RT. Taylor dispersion analysis compared to dynamic light scattering for the size analysis of therapeutic peptides and proteins and their aggregates. *Pharm Res*. 2011;28(9):2302-2310.
23. Sun T, Zhang YS, Pang B, Hyun DC, Yang M, Xia Y. Engineered nanoparticles for drug delivery in cancer therapy. *Angew Chemie - Int Ed*. 2014;53(46):12320-12364.
24. Kamaly N, Xiao Z, Valencia PM, Radovic-Moreno AF, Farokhzad OC. Targeted polymeric therapeutic nanoparticles: Design, development and clinical translation. *Chem Soc Rev*. 2012;41(7):2971-3010.
25. Farooq MU, Novosad V, Rozhkova EA, et al. Gold Nanoparticles-enabled Efficient Dual Delivery of Anticancer Therapeutics to HeLa Cells. *Sci Rep*. 2018;8(1):1-12.
26. Burdușel AC, Gherasim O, Grumezescu AM, Mogoantă L, Ficai A, Andronescu E. Biomedical applications of silver nanoparticles: An up-to-date overview. *Nanomaterials*. 2018;8(9):681.
27. Li Z, Barnes JC, Bosoy A, Stoddart JF, Zink JI. Mesoporous silica nanoparticles in biomedical applications. *Chem Soc Rev*. 2012;41(7):2590-2605.
28. Wang Y, Zhao Q, Han N, et al. Mesoporous silica nanoparticles in drug delivery and biomedical applications. *Nanomedicine Nanotechnology, Biol Med*. 2015;11(2):313-327.
29. Bentolila LA. Photoluminescent quantum dots in imaging, diagnostics and therapy. In: *Applications of Nanoscience in Photomedicine*. Elsevier Inc.; 2015:77-104.
30. Matea CT, Mocan T, Tabaran F, et al. Quantum dots in imaging, drug delivery and sensor applications. *Int J Nanomedicine*. 2017;12:5421-5431.
31. Dong H, Sun LD, Yan CH. Energy transfer in lanthanide upconversion studies for extended optical applications. *Chem*

Soc Rev. 2015;44(6):1608-1634. doi:10.1039/c4cs00188e

32. Liu RS. *Phosphors, up Conversion Nano Particles, Quantum Dots and Their Applications*. Springer Berlin Heidelberg; 2016.
33. Chen G, Roy I, Yang C, Prasad PN. Nanochemistry and Nanomedicine for Nanoparticle-based Diagnostics and Therapy. *Chem Rev*. 2016;116(5):2826-2885.
34. Chen G, Ågren H, Ohulchanskyy TY, Prasad PN. Light upconverting core-shell nanostructures: Nanophotonic control for emerging applications. *Chem Soc Rev*. 2015;44(6):1680-1713.
35. Chen G, Yang C, Prasad PN. Nanophotonics and nanochemistry: Controlling the excitation dynamics for frequency up- and down-conversion in lanthanide-doped nanoparticles. *Acc Chem Res*. 2013;46(7):1474-1486.
36. Himmelstoß SF, Hirsch T. A critical comparison of lanthanide based upconversion nanoparticles to fluorescent proteins, semiconductor quantum dots, and carbon dots for use in optical sensing and imaging. *Methods Appl Fluoresc*. 2019;7(2):22002.
37. Auzel F. Upconversion and Anti-Stokes Processes with f and d Ions in Solids. *Chem Rev*. 2004;104(1):139-173.
38. Chen G, Qiu H, Prasad PN, Chen X. Upconversion nanoparticles: Design, nanochemistry, and applications in Theranostics. *Chem Rev*. 2014;114(10):5161-5214.
39. Wolfbeis OS. An overview of nanoparticles commonly used in fluorescent bioimaging. *Chem Soc Rev*. 2015;44(14):4743-4768.
40. Yang D, Ma P, Hou Z, Cheng Z, Li C, Lin J. Current advances in lanthanide ion (Ln3+)-based upconversion nanomaterials for drug delivery. *Chem Soc Rev*. 2015;44(6):1416-1448.
41. Christ S, Schäferling M. Chemical sensing and imaging based on photon upconverting nano- and microcrystals: a review. *Methods Appl Fluoresc*. 2015;3(3):034004.
42. Liu Y, Tu D, Zhu H, Chen X. Lanthanide-doped luminescent nanoprobes: Controlled synthesis, optical spectroscopy, and

bioapplications. *Chem Soc Rev*. 2013;42(16):6924-6958.

43. DaCosta M V., Doughan S, Han Y, Krull UJ. Lanthanide upconversion nanoparticles and applications in bioassays and bioimaging: A review. *Anal Chim Acta*. 2014;832:1-33.
44. Gnach A, Lipinski T, Bednarkiewicz A, Rybka J, Capobianco JA. Upconverting nanoparticles: Assessing the toxicity. *Chem Soc Rev*. 2015;44(6):1561-1584.
45. Gu Z, Yan L, Tian G, Li S, Chai Z, Zhao Y. Recent advances in design and fabrication of upconversion nanoparticles and their safe theranostic applications. *Adv Mater*. 2013;25(28):3758-3779.
46. Scheps R. Upconversion laser processes. *Prog Quantum Electron*. 1996;20(4):271-358.
47. Chen G, Somesfalean G, Liu Y, Zhang Z, Sun Q, Wang F. Upconversion mechanism for two-color emission in rare-earth-ion-doped Zr O2 nanocrystals. *Phys Rev B - Condens Matter Mater Phys*. 2007;75(19):195204.
48. Chen GY, Liu Y, Zhang YG, et al. Bright white upconversion luminescence in rare-earth-ion-doped Y2 O3 nanocrystals. *Appl Phys Lett*. 2007;91(13):133103.
49. Chen GY, Zhang YG, Somesfalean G, Zhang ZG, Sun Q, Wang FP. Two-color upconversion in rare-earth-ion-doped ZrO2 nanocrystals. *Appl Phys Lett*. 2006;89(16):163105.
50. Chen GY, Somesfalean G, Zhang ZG, Sun Q, Wang FP. Ultraviolet upconversion fluorescence in rare-earth-ion-doped Y_2O_3 induced by infrared diode laser excitation. *Opt Lett*. 2007;32(1):87.
51. Gai S, Li C, Yang P, Lin J. Recent progress in rare earth micro/nanocrystals: Soft chemical synthesis, luminescent properties, and biomedical applications. *Chem Rev*. 2014;114(4):2343-2389.
52. Dong H, Sun LD, Yan CH. Basic understanding of the lanthanide related upconversion emissions. *Nanoscale*. 2013;5(13):5703-5714.

53. Zhao J, Sun Y, Kong X, et al. Controlled synthesis, formation mechanism, and great enhancement of red upconversion luminescence of NaYF4:Yb3+, Er3+ nanocrystals/submicroplates at low doping level. *J Phys Chem B*. 2008;112(49):15666-15672.
54. Wang F, Liu X. Recent advances in the chemistry of lanthanide-doped upconversion nanocrystals. *Chem Soc Rev*. 2009;38(4):976-989.
55. Wang M, Abbineni G, Clevenger A, Mao C, Xu S. Upconversion nanoparticles: Synthesis, surface modification and biological applications. *Nanomedicine Nanotechnology, Biol Med*. 2011;7(6):710-729.
56. Naccache R, Yu Q, Capobianco JA. The Fluoride Host: Nucleation, Growth, and Upconversion of Lanthanide-Doped Nanoparticles. *Adv Opt Mater*. 2015;3(4):482-509.
57. Mialon G, Türkcan S, Dantelle G, et al. High up-conversion efficiency of YVO4:Yb,Er nanoparticles in water down to the single-particle level. *J Phys Chem C*. 2010;114(51):22449-22454.
58. Martínez A, Morales J, Díaz-Torres LA, et al. Green and red upconverted emission of hydrothermal synthesized Y_2O_3: Er^{3+}-Yb^{3+} nanophosphors using different solvent ratio conditions. In: *Materials Science and Engineering B: Solid-State Materials for Advanced Technology*. Vol 174. Elsevier; 2010:164-168.
59. Ivaturi A, Macdougall SKW, Martín-Rodríguez R, et al. Optimizing infrared to near infrared upconversion quantum yield of β-$NaYF_4$:Er^{3+} in fluoropolymer matrix for photovoltaic devices. *J Appl Phys*. 2013;114(1):013505.
60. Wang H, Lau M, Sannomiya T, et al. Laser-induced growth of YVO_4:Eu^{3+} nanoparticles from sequential flowing aqueous suspension. *RSC Adv*. 2017;7(15):9002-9008.
61. Yi G, Lu H, Zhao S, et al. Synthesis, characterization, and biological application of size-controlled nanocrystalline $NaYF_4$:Yb,Er infrared-to-visible up-conversion phosphors. *Nano Lett*. 2004;4(11):2191-2196.

62. Altavilla C, ed. *Upconverting Nanomaterials*. Boca Raton : Taylor & Francis, 2016. | Series: Nanomaterials and: CRC Press; 2016.
63. Mai HX, Zhang YW, Si R, et al. High-quality sodium rare-earth fluoride nanocrystals: Controlled synthesis and optical properties. *J Am Chem Soc*. 2006;128(19):6426-6436.
64. Yang J, Shen D, Li X, et al. One-step hydrothermal synthesis of carboxyl-functionalized upconversion phosphors for bioapplications. *Chem - A Eur J*. 2012;18(43):13642-13650.
65. Li Z, Zhang Y. An efficient and user-friendly method for the synthesis of hexagonal-phase $NaYF_4$:Yb, Er/Tm nanocrystals with controllable shape and upconversion fluorescence. *Nanotechnology*. 2008;19(34).
66. Hudry D, Abeykoon AMM, Dooryhee E, Nykypanchuk D, Dickerson JH. Probing the Crystal Structure and Formation Mechanism of Lanthanide-Doped Upconverting Nanocrystals. *Chem Mater*. 2016;28(23):8752-8763.
67. Voorhees PW. The theory of Ostwald ripening. *J Stat Phys*. 1985;38(1-2):231-252.
68. Zhang F. Upconversion Nanoparticles for Biomedical Imaging. In: ; 2015:187-232.
69. Chen G, Qiu H, Prasad PN, Chen X. Upconversion nanoparticles: Design, nanochemistry, and applications in Theranostics. *Chem Rev*. 2014;114(10):5161-5214.
70. Muhr V, Wilhelm S, Hirsch T, Wolfbeis OS. Upconversion nanoparticles: From hydrophobic to hydrophilic surfaces. *Acc Chem Res*. 2014;47(12):3481-3493.
71. Prasad PN. *Introduction to Biophotonics*. Hoboken, NJ, USA: John Wiley & Sons, Inc.; 2003.
72. González-Béjar M, Francés-Soriano L, Pérez-Prieto J. Upconversion nanoparticles for bioimaging and regenerative medicine. *Front Bioeng Biotechnol*. 2016;4(JUN).
73. Chen G, Ohulchanskyy TY, Liu S, et al. Core/shell $NaGdF_4$:Nd^{3+}/$NaGdF_4$ nanocrystals with efficient near-infrared to near-

infrared downconversion photoluminescence for bioimaging applications. *ACS Nano*. 2012;6(4):2969-2977.

74. Ohulchanskyy TY, Roy I, Yong K-T, Pudavar HE, Prasad PN. High-resolution light microscopy using luminescent nanoparticles. *Wiley Interdiscip Rev Nanomedicine Nanobiotechnology*. 2010;2(2):162-175.
75. Dong H, Du SR, Zheng XY, et al. Lanthanide Nanoparticles: From Design toward Bioimaging and Therapy. *Chem Rev*. 2015;115(19):10725-10815.
76. Hao S, Chen G, Yang C. Sensing using rare-earth-doped upconversion nano-particles. *Theranostics*. 2013;3(5):331-345.
77. Green K, Huang K, Pan H, Han G, Lim SF. Optical Temperature Sensing With Infrared Excited Upconversion Nanoparticles. *Front Chem*. 2018;6:416.
78. Gu B, Zhang Q. Recent Advances on Functionalized Upconversion Nanoparticles for Detection of Small Molecules and Ions in Biosystems. *Adv Sci*. 2018;5(3):1700609.
79. Chen C, Li C, Shi Z. Current Advances in Lanthanide-Doped Upconversion Nanostructures for Detection and Bioapplication. *Adv Sci*. 2016;3(10).
80. Cheng L, Yang K, Li Y, et al. Facile preparation of multifunctional upconversion nanoprobes for multimodal imaging and dual-targeted photothermal therapy. *Angew Chemie - Int Ed*. 2011;50(32):7385-7390.
81. Liu J, Bu W, Pan L, Shi J. NIR-Triggered Anticancer Drug Delivery by Upconverting Nanoparticles with Integrated Azobenzene-Modified Mesoporous Silica. *Angew Chemie Int Ed*. 2013;52(16):4375-4379.
82. Fasani E, Mella M, Caccia D, Tassi S, Fagnoni M, Albini A. The photochemistry of lomefloxacin. An aromatic carbene as the key intermediate in photodecomposition. *Chem Commun*. 1997;(14):1329-1330.
83. Boscá F, Marín ML, Miranda MA. Photoreactivity of the

Nonsteroidal Anti-inflammatory 2-Arylpropionic Acids with Photosensitizing Side Effects¶. *Photochem Photobiol*. 2001;74(5):637.

84. Honeyman J. Efectos de las radiaciones ultravioleta en la piel. *Rev Peru Dermatología*. 2002;12.
85. Weissleder R. A clearer vision for in vivo imaging: Progress continues in the development of smaller, more penetrable probes for biological imaging. *Nat Biotechnol*. 2001;19(4):316-317.
86. Jimenez Pacheco, A., Arrabal Polo, M.A., Nogueras Ocaña M. No TitleResistencias a quinolonas en aislados clínicos de Escherichia coli productores de betalactamas de espectro extendido. *Hig y Sanid Ambient*. 2009;9:449-466.
87. Sortino S, Marconi G, Giuffrida S, Guidi G De, Monti S. Photophysical Properties of Rufloxacin in Neutral Aqueous Solution. *Photochem Photobiol*. 1999;70(5):731-736.
88. Leyva S, Leyva E. Fluoroquinolonas. Mecanismos de acción y resistencia, estructura, síntesis y reacciones fisicoquímicas importantes para propiedades medicinales. *Bol Soc Quím Méx*. 2008;2(1):1-13.
89. Kloskowski T, Gurtowska N, Nowak M, et al. The influence of ciprofloxacin on viability of A549, HepG2, A375.S2, B16 and C6 cell lines in vitro. *Acta Pol Pharm - Drug Res*. 2011;68(6):859-865.
90. Aranha O, Wood DP, Sarkar FH. Ciprofloxacin mediated cell growth inhibition, S/G2-M cell cycle arrest, and apoptosis in a human transitional cell carcinoma of the bladder cell line. *Clin Cancer Res*. 2000;6(3):891-900.
91. Johnstone RW, Ruefli AA, Lowe SW. Apoptosis: A link between cancer genetics and chemotherapy. *Cell*. 2002;108(2):153-164.
92. Perucca P, Savio M, Cazzalini O, et al. Structure-activity relationship and role of oxygen in the potential antitumour activity of fluoroquinolones in human epithelial cancer cells. *J*

Photochem Photobiol B Biol. 2014;140:57-68.

93. Cornaz-Buros S, Riggi N, Devito C, et al. Targeting cancer stem-like cells as an approach to defeating cellular heterogeneity in Ewing sarcoma. *Cancer Res*. 2014;74(22):6610-6622.
94. Perrone CE, Takahashi KC, Williams GM. Inhibition of human topoisomerase IIα by fluoroquinolones and ultraviolet A irradiation. *Toxicol Sci*. 2002;69(1):16-22.
95. Uhrich KE, Cannizzaro SM, Langer RS, Shakesheff KM. Polymeric Systems for Controlled Drug Release. *Chem Rev*. 1999;99(11):3181-3198.
96. Peer D, Karp JM, Hong S, Farokhzad OC, Margalit R, Langer R. Nanocarriers as an emerging platform for cancer therapy. *Nat Nanotechnol*. 2007;2(12):751-760.
97. Kim K, Pollard JM, Norris AJ, et al. High-throughput screening identifies two classes of antibiotics as radioprotectors: Tetracyclines and fluoroquinolones. *Clin Cancer Res*. 2009;15(23):7238-7245.
98. Zhu X, Radovic-Moreno AF, Wu J, Langer R, Shi J. Nanomedicine in the management of microbial infection - Overview and perspectives. *Nano Today*. 2014;9(4):478-498.
99. Albanese A, Tang PS, Chan WCW. The effect of nanoparticle size, shape, and surface chemistry on biological systems. *Annu Rev Biomed Eng*. 2012;14:1-16.
100. Hoare T, Timko BP, Santamaria J, et al. Magnetically triggered nanocomposite membranes: A versatile platform for triggered drug release. *Nano Lett*. 2011;11(3):1395-1400.
101. Epstein-Barash H, Orbey G, Polat BE, et al. A microcomposite hydrogel for repeated on-demand ultrasound-triggered drug delivery. *Biomaterials*. 2010;31(19):5208-5217.
102. Timko BP, Arruebo M, Shankarappa SA, et al. Near-infrared-actuated devices for remotely controlled drug delivery. *Proc Natl Acad Sci U S A*. 2014;111(4):1349-1354.
103. Das GK, Anderson DS, Wallis CD, Carratt SA, Kennedy IM, Van

Winkle LS. Novel multi-functional europium-doped gadolinium oxide nanoparticle aerosols facilitate the study of deposition in the developing rat lung. *Nanoscale*. 2016;8(22):11518-11530.

104. Zhou J, Liu Q, Feng W, Sun Y, Li F. Upconversion luminescent materials: Advances and applications. *Chem Rev*. 2015;115(1):395-465.
105. Fedoryshin LL, Tavares AJ, Petryayeva E, Doughan S, Krull UJ. Near-infrared-triggered anticancer drug release from upconverting nanoparticles. *ACS Appl Mater Interfaces*. 2014;6(16):13600-13606.
106. Dai Y, Xiao H, Liu J, et al. In vivo multimodality imaging and cancer therapy by near-infrared light-triggered trans -platinum pro-drug-conjugated upconverison nanoparticles. *J Am Chem Soc*. 2013;135(50):18920-18929.
107. Min Y, Li J, Liu F, Yeow EKL, Xing B. Near-Infrared Light-Mediated Photoactivation of a Platinum Antitumor Prodrug and Simultaneous Cellular Apoptosis Imaging by Upconversion-Luminescent Nanoparticles. *Angew Chemie*. 2014;126(4):1030-1034.
108. Herrmann A. Controlled Release of Volatiles under Mild Reaction Conditions: From Nature to Everyday Products. *Angew Chemie Int Ed*. 2007;46(31):5836-5863.
109. Herrmann A. Using photolabile protecting groups for the controlled release of bioactive volatiles. *Photochem Photobiol Sci*. 2012;11(3):446-459.
110. Suyama K, Shirai M. Photobase generators: Recent progress and application trend in polymer systems. *Prog Polym Sci*. 2009;34(2):194-209.
111. Zhao H, Sterner ES, Coughlin EB, Theato P. O-Nitrobenzyl alcohol derivatives: Opportunities in polymer and materials science. *Macromolecules*. 2012;45(4):1723-1736.
112. Klán P, Šolomek T, Bochet CG, et al. Photoremovable protecting groups in chemistry and biology: Reaction mechanisms and

efficacy. *Chem Rev*. 2013;113(1):119-191.

113. Hansen MJ, Velema WA, Lerch MM, Szymanski W, Feringa BL. Wavelength-selective cleavage of photoprotecting groups: strategies and applications in dynamic systems. *This J is Cite this Chem Soc Rev*. 2015;44:3358.
114. Fonseca ASC, Gonçalves MST, Costa SPG. Photocleavage studies of fluorescent amino acid conjugates bearing different types of linkages. *Tetrahedron*. 2007;63(6):1353-1359.
115. Furuta T, Watanabe T, Tanabe S, Sakyo J, Matsuba C. Phototriggers for nucleobases with improved photochemical properties. *Org Lett*. 2007;9(23):4717-4720.
116. Subramaniam R, Xiao Y, Li Y, Qian SY, Sun W, Mallik S. Light-mediated and H-bond facilitated liposomal release: the role of lipid head groups in release efficiency. *Tetrahedron Lett*. 2010;51(3):529-532.
117. Wylie RG, Shoichet MS. Two-photon micropatterning of amines within an agarose hydrogel. *J Mater Chem*. 2008;18(23):2716-2721.
118. Johnson SL, Morrison DL. Kinetics and Mechanism of Decarboxylation of N-Arylcarbamates. Evidence for Kinetically Important Zwitterionic Carbamic Acid Species of Short Lifetime. *J Am Chem Soc*. 1972;94(4):1323-1334.
119. Papageorgiou G, Barth A, Corrie JET. Flash photolytic release of alcohols from photolabile carbamates or carbonates is rate-limited by decarboxylation of the photoproduct. *Photochem Photobiol Sci*. 2005;4(2):216-220.
120. Senda N, Momotake A, Nishimura Y, Arai T. Synthesis and Photochemical Properties of a New Water-Soluble Coumarin, Designed as a Chromophore for Highly Water-Soluble and Photolabile Protecting Group. *Bull Chem Soc Jpn*. 2006;79(11):1753-1757.
121. Schmidt R, Geissler D, Hagen V, Bendig J. Mechanism of photocleavage of (coumarin-4-yl)methyl esters. In: *Journal of*

Physical Chemistry A. Vol 111. American Chemical Society; 2007:5768-5774.

122. Schmidt R, Geissler D, Hagen V, Bendig J. Kinetics study of the photocleavage of (coumarin-4-yl)methyl esters. *J Phys Chem A*. 2005;109(23):5000-5004.
123. Kessler M, Glatthar R, Giese B, Bochet CG. Sequentially photocleavable protecting groups in solid-phase synthesis. *Org Lett*. 2003;5(8):1179-1181.
124. Stegmaier P, Alonso JM, Del Campo A. Photoresponsive surfaces with two independent wavelength-selective functional levels. *Langmuir*. 2008;24(20):11872-11879.
125. San Miguel V, Bochet CG, Del Campo A. Wavelength-selective caged surfaces: How many functional levels are possible? *J Am Chem Soc*. 2011;133(14):5380-5388.
126. Stanton-Humphreys MN, Taylor RDT, Mc Dougall C, et al. Wavelength-orthogonal photolysis of neurotransmitters in vitro. *Chem Commun*. 2012;48(5):657-659.
127. Bochet CG. Orthogonal Photolysis of Protecting Groups. *Angew Chemie Int Ed*. 2001;40(11):2071-2073.
128. Rodrigues-Correia A, Weyel XMM, Heckel A. Four levels of wavelength-selective uncaging for oligonucleotides. *Org Lett*. 2013;15(21):5500-5503.
129. Griffin DR, Kasko AM. Photoselective delivery of model therapeutics from hydrogels. *ACS Macro Lett*. 2012;1(11):1330-1334.
130. Priestman MA, Sun L, Lawrence DS. Dual wavelength photoactivation of cAMP- and cGMP-dependent protein kinase signaling pathways. *ACS Chem Biol*. 2011;6(4):377-384.
131. Ladlow M, Legge CH, Neudeck T, Pipe AJ, Sheppard T, Yang LL. Wavelength dependent photo-controlled differential release of compounds from solid phase resin. *Chem Commun*. 2003;3(16):2048-2049.
132. Blanc A, Bochet CG. Wavelength-controlled orthogonal

photolysis of protecting groups. *J Org Chem*. 2002;67(16):5567-5577.

133. Kotzur N, Briand B, Beyermann M, Hagen V. Wavelength-selective photoactivatable protecting groups for thiols. *J Am Chem Soc*. 2009;131(46):16927-16931.
134. Schäfer F, Joshi KB, Fichte MAH, MacK T, Wachtveitl J, Heckel A. Wavelength-selective uncaging of da and dC residues. *Org Lett*. 2011;13(6):1450-1453.
135. Yip RW, Sharma DK, Giasson R, Gravel D. Photochemistry of the o-nitrobenzyl system in solution: Evidence for singlet state intramolecular hydrogen abstraction. *J Phys Chem*. 1985;89(25):5328-5330.
136. Papageorgiou G, Corrie JET. Synthesis and properties of carbamoyl derivatives of photolabile benzoins. *Tetrahedron*. 1997;53(11):3917-3932.
137. Corrie JET, Barth A, Munasinghe VRN, Trentham DR, Hutter MC. Photolytic cleavage of 1-(2-nitrophenyl)ethyl ethers involves two parallel pathways and product release is rate-limited by decomposition of a common hemiacetal intermediate. *J Am Chem Soc*. 2003;125(28):8546-8554.

Chapter 2. General Objectives

This doctoral thesis focuses on developing new anticancer treatments by using new prodrugs and nanoparticles. The new treatments will be created combining drugs used or not for cancer treatments with up-conversion nanoparticles and using near infrared light.

Accordingly, this has been approached through the following specific objectives, which correspond to the different chapters of this Doctoral Thesis:

1. To synthesize new fluoroquinolones with higher photogenotoxic effect and undertake complete photochemical, photophysical and phototoxic characterization.

2. To undertake a complete study of fluoroquinolone-biomolecules interaction under light with the new fluoroquinolones.

3. To develop and study new material based on biocompatible up-conversion nanoparticles carried with the most phototoxic fluoroquinolone.

4. To analyze the photophysical and photochemical properties of new prodrugs using a 7-aminomethyl coumarin derivative as the photolabile molecule.

5. To create a new material based on biocompatible up-conversion nanoparticles carried with prodrugs made with a 7-aminomethyl coumarin derivative and chlorambucil.

Chapter 3: Chemical tuning for potential antitumor fluoroquinolones

3.1. Introduction

Quinolones are “building blocks” with flexible synthetic routes that can be adapted to prepare large libraries of bioactive compounds. Since 1962, 4-quinolone-3-carboxylic acid derivatives are widely used as antibacterial agents and for tuberculosis treatment.[1,2] Moreover, during the last few years, structural modifications on quinolones have shown that this type of compounds can also display antitumor and/or antiviral activities.[3–9] Thereby, both, high activity of these drugs against eukaryotic topoisomerase and their relevant toxicity to cultured mammalian cells and in vivo tumor cells,[10] clearly show their potential as new anticancer agents. A family of modified quinolones with antitumor activity that reduce all-cause mortality among cancer patients are the fluoroquinolones (FQ). [11]

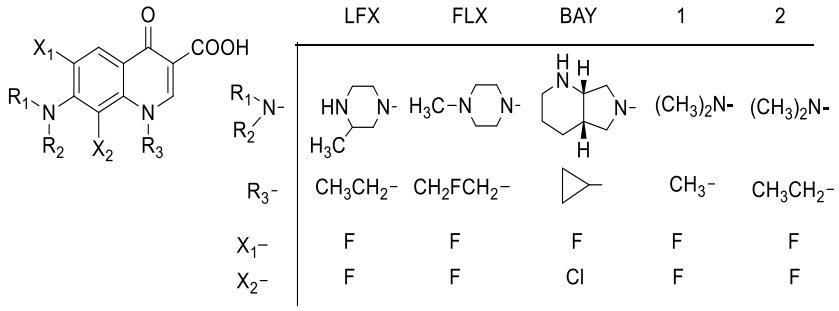

Chart 3.1. Chemical structure of dihalogenated FQs

Interestingly, a recent study reported an enhancement of the FQ genotoxicity in an eukaryotic system by UV irradiation,[12] which also confers to these drugs a potential property as photochemotherapeutic agents. In this context, phototoxicity and photogenotoxicity have been remarkably detected in dihalogenated quinolones such as fleroxacin

(FLX), BAY y3118 (BAY) as well as lomefloxacin (LFX, compound used as standard for photomutagenic studies, see structures in Chart 3.1).[13–21] Consequently, a large number of studies concerning the photophysical and photochemical properties of 6,8-dihalogenated FQ in the presence and/or absence of biomolecules have been carried out. An unusual photodehalogenation of these FQ by heterolysis of their C8–halogen bonds is the key point in the photoinduced biological damages. The FQ photosensitivity reactions have been associated with the generation of reactive intermediates in their photodehalogenation processes.[22–28] In fact, two pathways have been proposed to explain the photoinduced adverse effects observed for this type of FQ: I) an aryl radical ($FQ(-F)^{\cdot}$) is generated from an intermolecular electron transfer between FQ singlet excited state and a complexed electron donor biomolecule, and II) an aryl cation with alkylating properties is formed from the heterolytic dehalogenation of its FQ triplet excited state (^3FQ) (see Scheme 3.1).[26–28] Interestingly, it has been observed in FQ photodegradation studies that peripheral substituents of FQ skeleton such as the piperazinyl ring and or the *N*(1) alkyl substituents react with the aryl cation ($FQ(-F)^+$ to produce photoproducts, hindering intermolecular photoreactions with biomolecules or molecular oxygen (see pathway II in Scheme 3.1).[27,28] Photoallergy is mainly produced from pathway I,[27] however, the contribution of routes I and II is still imprecise for the phototoxic processes associated with FQ.

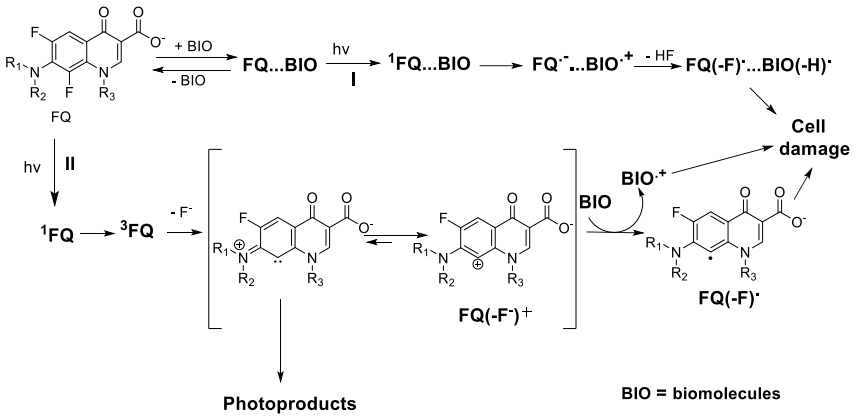

Scheme 3.1. Proposed mechanisms for the photodehalogenation process of 6,8-difluoroquinolones (FQ) in presence of biomolecules (BIO).

With this background, the aim of the present study is to enhance the phototoxic potential of FQ in order to obtain drugs with more photochemotherapeutic properties. For this purpose, it was thought to decrease the FQ peripheral size for improving the efficiency of the intermolecular photoreactions between FQ and biomolecules or molecular oxygen via pathway II. Thus, a new tailored 6,8-dihalogenated FQ (1-methyl-6,8-difluoro-4-oxo-7-aminodimethyl-1,4-dihidroquinoline-3-carboxylic acid (**1**), see Chart 3.1 was synthesized. In order to probe this hypothesis, photophysical and photochemical studies (fluorescence emissions, time resolved and steady state photolysis) will be combined together with in vitro cell cultured experiments (3T3 NRU phototoxicity assay) using FQ derivatives with different peripheral substituents (see chemical structures in Chart 3.1). Thus, the selected FQ was the new compound **1**, LFX and 1-ethyl-6,8-difluoro-4-oxo-7-aminodimethyl-1,4-dihidroquinoline-3-carboxylic

acid (**2**).[29] Moreover, the role of the FQ photodehalogenation pathways in the phototoxic properties associated with FQ will be also evaluated.

3.2. Results and discussion

3.2.1. Absorption spectra of fluoroquinolones 1 and 2

The absorption spectra of **1** and **2** showed almost identical UV-Vis spectral features (see Figure 3.1). Nevertheless, in the case of LFX, although its absorption maxima were also similar to those of **1** and **2**, some changes can be observed, indicating that some photophysical properties of the quinolone chromophore change by the presence of a piperazinyl ring.

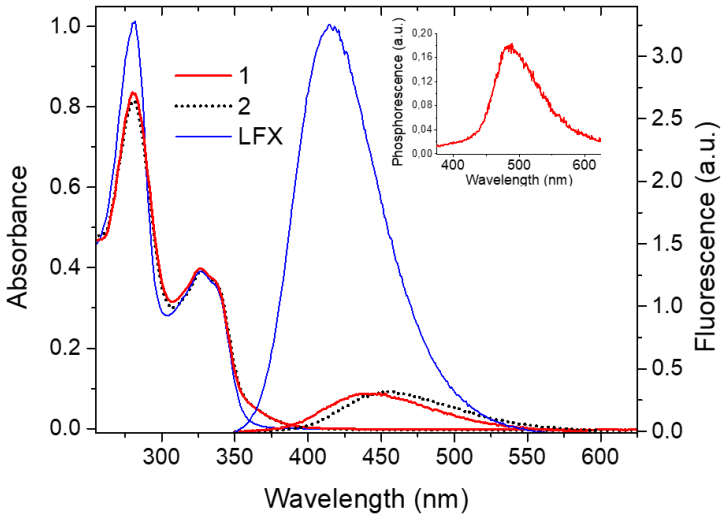

Figure 3.1. Absorption (left) and fluorescence (right) of compound **1**, **2** and LFX (4×10^{-5} M) in 2 mM PB aqueous medium. Inset: Phosphorescence of **1** in aqueous medium at 77 K. The emission measurements were performed at the excitation wavelength of 310 nm.

3.2.2. Emission measurements of fluoroquinolones 1 and 2

Fluorescence spectrum of LFX under neutral conditions (1 mM PB aqueous medium, pH *ca.* 7.4) showed an emission band with a maximum at 415 nm as described in the literature.[22] However, the fluorescence spectra of **1** and **2** display bands at λ_{max} *ca.* 445 and 455 nm respectively, exhibiting a redshift effect. In this context, fluorescence quantum yields (ϕ_{Fl}) of 1 and 2 resulted to be markedly lower than that described for LFX (ϕ_{Fl} *ca*. 0.08) but their emission lifetimes were similar (Table 3.1).

Table 3.1. Emission and photochemical properties of LFX, 1 and 2 in aqueous media.

	[a]Fl			[b]Ph		[c]ϕ_D
FQ	λ_{max} nm	ϕ_{Fl}	τ_{Fl} ns	λ_{max} nm	H_2O	H_2O/EtOH (1/1)
LFX	415	0.080	1.3	480	0.55	
1	445	0.008	1.2	480	0.40	0.62
2	455	0.008	1.3	480	0.75	0.76

[a]In aqueous medium. [b]In frozen buffered aqueous media at 77 K.

[c]Photodegradation quantum yields were determined taking as standard LFX in water (ϕ_D = 0.55) [25].

When phosphorescence measurements of **1**, **2** and LFX were performed in frozen buffered aqueous media at 77 K, their emission spectra resulted to be almost identical (see inset Figure 3.1 for phosphorescence of **1**). Thus, a triplet energy *ca.* 273 kJ/mol was determined for the three compounds.

The decay traces of singlet-oxygen ($^1O_2$) phosphorescence at 1270 nm generated by pulsed-laser irradiation at 355 nm of aerated deuterated aqueous neutral solutions (1 mM PB aqueous medium, pH *ca.* 7.4) of LFX, **1**, **2** and perinaphthenone as reference were recorded to determine $^1O_2$ quantum yield (ϕ_Δ)of these FQs. The values obtained revealed ϕ_Δ for LFX, **1** and **2** lower than 0.005. The result obtained for LFX is not completely in agreement with the value described in the literature (ϕ_Δ *ca.* 0.07 in buffered deuterated water).[30] However, as photodegradation quantum yield (ϕ_D) of LFX is very high (ϕ_D = 0.55),[25] the value described could have increased due to $^1O_2$ generation from photoproducts generated during the measurements. In fact, we observed that the use of several fresh samples during the acquisition of the value of each dihalogenated fluoroquinolone was needed.

3.2.3. Laser flash photolysis studies (LFP) of fluoroquinolones 1 and 2

Laser flash photolysis of **1** and **2** were carried out in buffered water (1 mM PB) under different atmospheres using LFX as reference compound. Thus, LFX under N_2O atmosphere at pH = 7.4 showed the presence of an aryl cation with λ_{max} 480 nm and a lifetime (τ) of 250 ns, data very similar to those described in the literature.[22–24] When the experiments were performed using **1**, an intermediate absorbing also at λ_{max} 480 nm was also detected (see Figure 3.2). However, this intermediate showed longer lifetime (τ *ca.* 3.1 μs) than the observed for LFX. A reactivity study using molecular oxygen was performed in order to determine the nature of the intermediate arising from photolysis of **1**. The fact that the presence of molecular oxygen up to 2

x 10^{-3} M did not show any effect on the intermediate lifetime discards a triplet excited state nature. Hence, to achieve an unambiguous assignment of this transient species, compound **1** was submitted to LFP in the presence of a nucleophilic anion such as Br^-. The efficient quenching by Br^- showed a rate quenching constant of 1.5 x 10^{10} M^{-1} s^{-1}, a value very close to those reported for aryl cations generated from LFX and other dihalogenated FQ such as BAY y3118 or fleroxacin.[23,31]

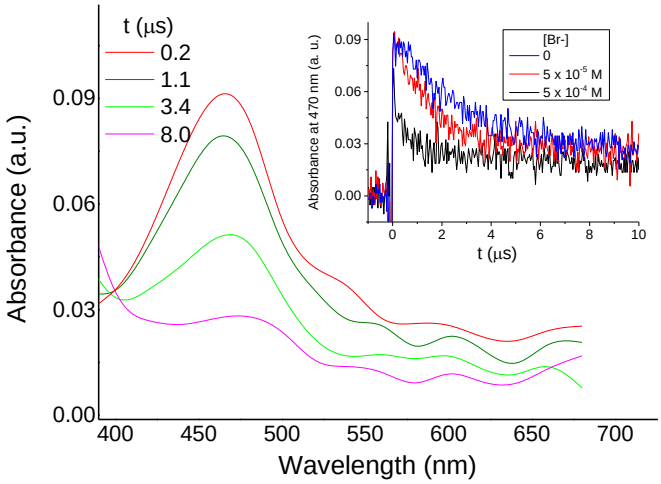

Figure 3.2. Transient absorption spectra of **1** (10^{-4} M) in aqueous 1 mM PB in N_2O atmosphere at different times after the 355 nm laser excitation. Inset: Decay traces at 470 nm of **1** under the same conditions in the presence of different concentrations of Br^- anion.

Interestingly, LFP assays using **2** in aqueous solutions showed two consecutive transient species (see Figure 3.3). The first one displayed an absorption spectrum with a λ_{max} 470 nm with a $\tau < 300$ ns and the second one at λ_{max} 460 nm and a τ 980 ns. It was observed that the two

bands were not appreciably quenched or modified by the presence of O_2 atmosphere, whereas they were affected by the presence of the Br^- anion. Apparently, the first intermediate seems to be reactive to the anion while the second one decreases its absorbance (see inset of Figure 3.3). Thereby, the structure of the first transient species would be attributed to an aryl cation $(FQ(-F)^+)$ similar to the describe for most of the dihalogenated FQ including **1**. The assignment of the second one could be a diradical cation $(FQ(-F)^{\cdot\cdot+})$ arising from the first intermediate (see Scheme 3.1) as it has previously been proposed in the photolysis of *N*-acetylated LFX.[22]

In this context, highlight the absence of any detectable triplet excited state corresponding to the FQs, which is in agreement with the almost inappreciable detection of $^1O_2$ for these compounds.

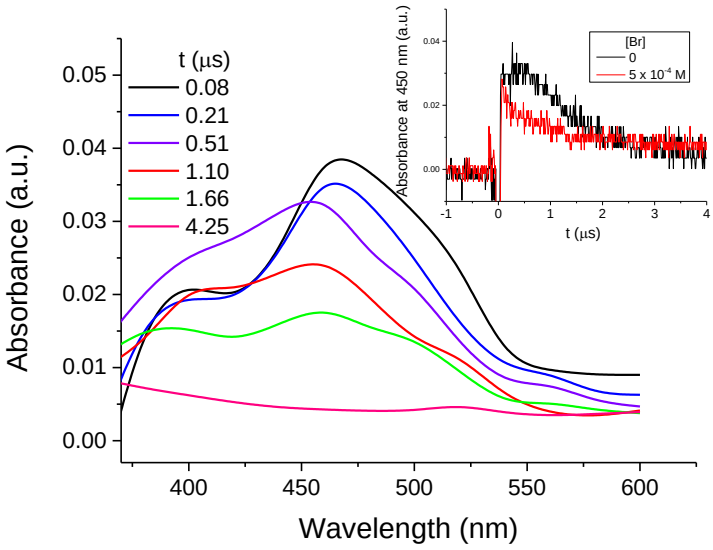

Figure 3.3. Transient absorption spectra of **2** (10^{-4} M) in aqueous 1 mM PB in N_2O atmosphere at different times after the 355 nm laser excitation. Inset: Decay traces at 450 nm of **1** under aerobic condition in the presence and/or absence of Br^- anion.

When the LFP of **1**, **2** and LFX were carried out under N_2 atmosphere, besides detecting the same transient species with similar lifetimes than in the experiments performed in N_2O, an intermediate absorbing at λ_{max} *ca.* 720 nm was observed. The spectrum absorption shape and the high quenching rate constant by oxygen and N_2O (> 10^9 M^{-1} s^{-1}) supports its assignment as the solvated electron. In fact, this intermediate has been observed in neutral aqueous medium by excitation at 355 nm through a two-photon process under moderate laser energy conditions in all FQ studied under similar conditions.[23,32–34] In this context, in agreement with the literature,[22–28] the solvated electrons detected under N_2 or the hydroxyl radicals generated from the reaction of solvated electrons

with N_2O do not seem to modify the lifetime of the detected intermediates.

3.2.4. Photodegradation studies

Irradiations of **1** and **2** in deaerated aqueous solutions at pH *ca.* 7.4 using LFX as reference compound were performed in a multilamp photoreactor using UVA light at λ_{max} = 350 nm. Kinetics studies showed different photodegradation quantum yields (ϕ_D) for **1**, **2** and LFX (Table 3.1). Analysis of the photoreactions revealed a photodegradation quantum yield (ϕ_D) of 0.4 for **1** but only a small number of photoproducts were detected being the major photoproduct with **1P** with a formation quantum yield (ϕ_{PF}) lower than 0.02 (see structure in Scheme 3.2). Thereby, a photopolymerization process justifies the high ϕ_D of **1**. Interestingly, photolysis of **2** showed the highest ϕ_D giving rise mainly to **2P1** (ϕ_{PF} 0.75) and small amounts of **2P2** (ϕ_{PF} of 0.05) (see Scheme 3.2). In this context, significant changes were observed when the photodegradation of **1** was carried out using a hydrogen donor media such as a mixture of ethanol/water (2 mM PB) 1/1. In fact, ϕ_D of **1** increased to 0.62 and the ϕ_{PF} of its photoproduct **1P** grew up to 0.20. By contrast, ϕ_D of **2** did not appreciably change in the aqueous alcoholic medium (ϕ_D = 0.76) although ϕ_{PF} of its photoproducts was modified (ϕ_{PF} of 0.70 and 0.14 for **2P1** and **2P2** respectively). The structures of **1P**, **2P1** and **2P2** were unambiguously assigned using the spectroscopic data, which are listed in the experimental section (See NMR spectra in section 3.5).

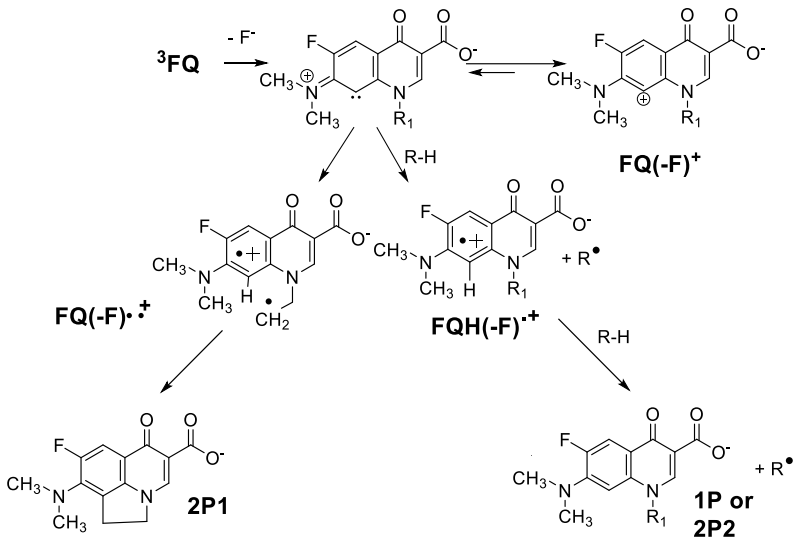

Scheme 3.2. Photodegradation pathways of 1 and 2 in aqueous media.

3.2.5. Phototoxic properties

Cell viability upon incubation with LFX, 1 and 2 in combination with UVA light was assessed by the in vitro 3T3 NRU phototoxicity test. Thus, cytotoxicity profiles of BALB/c 3T3 fibroblasts treated with LFX, 1 and 2 were measured in the presence and absence of UVA light, using neutral red as vital dye, and half maximal inhibitory concentration (IC_{50}) were determined from dose-response curves (see Figure 3.4).

This test is based on the calculation of the Photo-Irritation-Factor (PIF) that corresponds to the ratio of the IC_{50} for each compound with and without UVA irradiation. The obtained values are shown in Table 3.2.

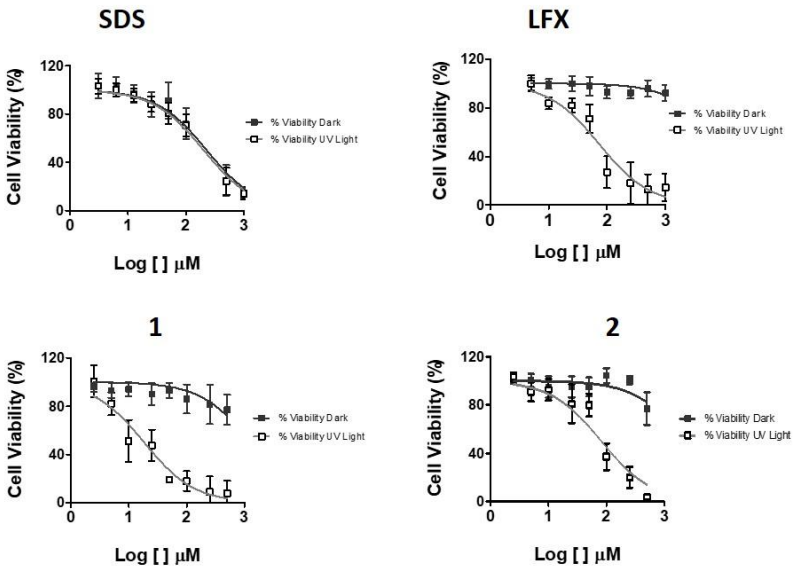

Figure 3.4. Dose-Response curves for cell viability of 3T3 cells treated with SDS, LFX, **1** and **2** by using neutral red vital stain (NRU) assay in the presence (□) or absence (■) of UV Light. Data represent Mean±SD from four independent experiments. SDS and LFX were used as negative and positive control of phototoxicity, respectively.

Table 3.2. In vitro 3T3 NRU phototoxicity assay of LFX, **1** and **2**.

Compound	IC_{50} dark (µM)	IC_{50} UVA Light (µM)	Photoirritant factor (PIF)[a]
LFX	> 500	50±8	> 10
1	> 500	16±9	> 30
2	> 500	65±26	> 8
SDS	220±21	244±25	1

Data represent mean ±SD from four independent experiments. LFX and SDS were used as positive and negative controls of phototoxicity, respectively.

[a]According to the OECD (2004)[35], PIF<2 means "No Phototoxicity", 2<PIF<5 means "Probably Phototoxicity" and PIF>5 means "Phototoxicity".

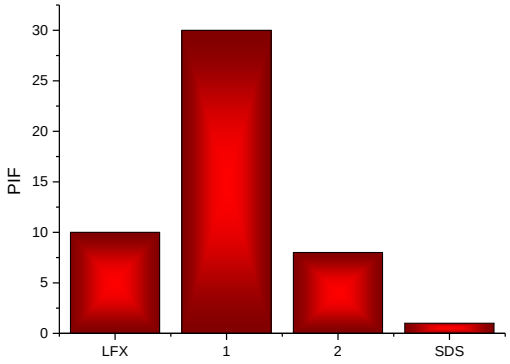

Figure 3.5. Data represent the Photo-Irritation-Factor (PIF) determined using the equation PIF=IC_{50} DARK/IC_{50} UVA LIGHT. The IC_{50} were determined from the 3T3 NRU assay. 3T3 cells were treated with serial dilutions of LFX, **1** and **2** ranging from 0.5µM to 500µM for 1h, followed by irradiation (or not) with a dose of 5J/cm^2 UVA light. LFX and SDS were used as positive and negative control of phototoxicity, respectively.[35,36] After 24 h cell viability was determined by neutral red uptake and IC_{50} values were calculated by non-lineal regression with GraphPad Prism 5.0.

As shown in Table 3.2 and Figure 3.5, LFX was clearly phototoxic as anticipated (PIF *ca.* 10). For **2** a toxicity with a PIF of *ca.* 8 was obtained. Interestingly, the effect observed for **1** resulted to be higher than LFX and **2** (a 3-fold increase of the IC_{50} was determined, PIF *ca.* 30). Noteworthy, only **1** displays a *N*(1) methyl substituent. Hence, the different behavior shown in phototoxic assays may be modulated by the *N*-alkyl chain of the fluoroquinolones. However, as FQ location in cells could modify the biomolecules photodegradation and, consequently the phototoxicity, intracellular localization of LFX, **1** and

2 in FSK cells was performed by confocal microscopy. Interestingly, as shown in Figure 3.5, similar cytoplasmic distribution is observed for all compounds (blue emission), indicating that the higher photo-toxicity of 1 relative to LFX and 2 can not be attributed to damage of different cellular targets.

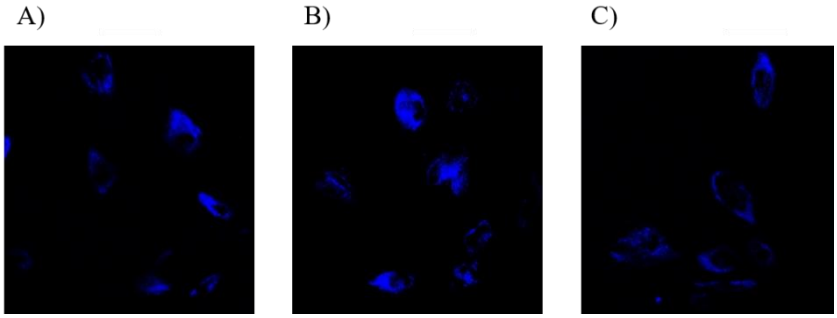

Figure 3.6. Confocal microscopy images of intracellular localization of LFX (A), 1 (B) and 2 (C) in FSK cells (blue fluorescence). Representative images were selected from three different regions on the slide.

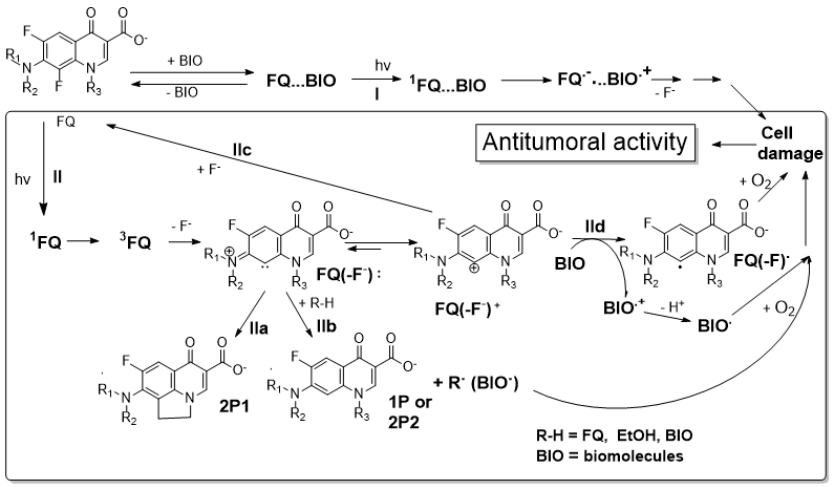

Scheme 3.3. Photodegradation pathways of 1 and 2 in presence of hydrogen and/or electron donors organic compounds.

The photophysical, photochemical and photobiological properties found for **1** and **2** together with those described in the literature for other dihalogenated FQ[22–28,35] were analyzed to rationalize the possible mechanisms involving the photosensitized cell damage produced by the dihalogenated FQ **1** and **2**.

Initially, as the UV-induced biomolecules damage in the presence of FQs can involve a triplet-triplet energy transfer reaction, photosensitized generation of $^1O_2$ and radicals generation from FQ photodehalogenation,[13,37] all of them would be evaluated to determine the mechanisms responsible for the phototoxic properties associated with the dihalogenated quinolones. However, the lack of detection of any triplet excited state for LFX, **1** and **2** in the laser flash photolysis experiments and the almost unappreciable singlet oxygen generation from the three dihalogenated quinolones clearly evidence that the photodehalogenation of these FQs is their major process to produce the biological damage. The apparent inconsistency between the lack of detection of LFX triplet excited state and the described LFX-photosensitized formation of cyclobutane dimers in cellular DNA,[37] which must occur via triplet-triplet energy transfer mechanism,[38] could be understood through the participation of LFX photoproducts because the photodehalogenation is highly efficient process for LFX. In fact, this also explains why a $^1O_2$ generation quantum yield of 0.07 had been described for LFX.[30] Thereby, the main pathways involving photodehalogenation of LFX, **1** and **2** are shown in Scheme 3.3. As previously shown in Scheme 3.1 for LFX and other dihalogenated

quinolones,[26–28] the most relevant photosensitization processes associated with dihalogenated FQ including compound **1** and **2** can be understood from photodehalogenation pathways I and II. However, the results obtained in this study have evidenced that the reactions arising from II must be the key processes in the FQ photosensitized cell damage. In this context, photophysical and photochemical properties of **1**, **2** and LFX were compared to determine the effects of peripheral substituents such as the *N*(1)alkyl or the piperazinyl ring. Thus, although most of the photophysical properties of **2** are quite different to that of LFX (see Figure 3.1 and Table 3.1), photodegradation of aqueous solutions of **2** mainly produces photoproduct **2P1** (see via IIa in Scheme 3.3), a tricyclic compound similar to the main photoproduct of LFX.[26–28] An intramolecular hydrogen abstraction reaction between the aryl carbene of **2** and its *N*(1)ethyl group initiates a cyclization route to form **2P1** (intermediates involving this process are shown in Scheme 3.2). By contrast, photoproduct analysis of the irradiation of **1** revealed the inability of the aryl carbene FQ(-F^-): of **1** to react with its *N*(1)-methyl substituent. These results can be correlated with the results of laser flash photolysis experiments, where the detected aryl cations arising from **1** and **2** showed important differences in the generation and lifetime of their aryl cations (see Figure 3.1 and Figure 3.2). Hence, a fast intramolecular rate constant between a carbene FQ(-F^-): and its *N*(1)-ethyl substituent can justify the observed decrease in the generation and lifetime of the aryl cations arising from **2** and also from LFX. Thereby, the longer lifetime of the aryl cation of **1** produces an efficiency growth of the intermolecular reactions of this intermediate

with its released fluorine anion (via IIc, which clarifies the lower photodegradation quantum yield of **1** than that of **2** or LFX under the same conditions (Table 3.1)) or with **1** ground states (via IIb, which can be the first step of a polymerization process). In this context, pathway IIb can also explain the degradation changes observed in the photolysis of **1** and **2** when they were performed using a hydrogen donor solvent such as ethanol (see results in Table 3.1). Thus, the presence of high amounts of hydrogen donor molecules in the photoreaction media produces a reaction rate increase of the aryl carbene FQ(-F^-): generated from **1** or **2** with ethanol, which improves the formation of photoproduct **1P** or **2P2,** respectively. By contrast, the efficiency of the other hydrogen abstraction processes is reduced. Hence, the presence of ethanol in the photodegradation of **1** also produces a decrease of the intermolecular reactions of the aryl carbene FQ(-F^-): with its ground state (see via IIb in Scheme 3.3) and with fluoride anion via IIc (Scheme 3.3). Consequently, a low photopolymerization of **1** and a growth of its photodegradation quantum yield (see Table 3.1), respectively, is observed. In the case of **2**, as its intermolecular reactions of via IIb compete mainly with the intramolecular pathway IIa (see Scheme 3.3), the presence of ethanol reduces the amounts of **2P1**.

These findings resulted to be relevant to understand the cellular damage photoinduced by FQ when *in vitro* 3T3 NRU assays were performed. Thus, a clear correlation between the photodehalogenation process of route II and phototoxic effects in cultured cells was found (see Figure 3.3 and Table 3.2). The highest phototoxicity produced by **1**

in the presence of fibroblast cells seems to indicate that the main pathway involved in its phototoxicity is pathway II because only this route can be influenced by the reactivity of the *N*(1)-alkyl chain of FQ (Scheme 3.2 and Scheme 3.3). Intermolecular reactions between biomolecules and the intermediates arising from FQ dehalogenation are the main processes involved in the phototoxicity of **1** (see pathways IIb and IId in Scheme 3.3), however for **2** and LFX, annihilation of their aryl carbenes by coupling of them with their N(1)-ethyl groups is an efficient process competing with pathways IIb and IId. The interpretation of the findings could be incorrect if the cellular location of **1**, **2** and LFX was different because this fact could modulate the biomolecules photodegradation and consequently the phototoxic effects. Interestingly, as shown in Figure 3.6, similar cytoplasmic distribution is observed for all compounds (blue emission), indicating that the higher phototoxicity of **1** relative to LFX and **2** cannot be attributed to damage of different cellular targets.

3.3. Conclusion

A new FQ (**1**) with a *N*(1)-methyl group has been synthesized, the reduction in the length of the *N*(1)-alkyl chain of FQ reveals significant changes in the FQ photodehalogenation processes. Thus, an increase in the generation efficiency and lifetime of a reactive intermediate is observed and the photoproducts formation is also modified. Besides, the results of *in vitro* 3T3 NRU assays revealed a higher phototoxicity for **1** than those with longer a *N*(1)-alkyl chain. All the results can be understood by the lack of intramolecular reactivity of a carbene

intermediate with its *N*(1)-methyl substituent. Moreover, the higher phototoxicity for **1** also confirms that the photodehalogenation arising from the free FQ (in bulk water) is the main pathway involved in the phototoxic processes. This study provides a way for tuning the phototoxicity of FQ, which could be used to enhance this adverse effect as a photochemotherapeutic property to improve their antitumor activity.

3.4. Experimental section

3.4.1. Materials

Ethyl 6,7,8-trifluoro-1,4-dihydro-4-oxo-3-quinolinecarboxylate and lomefloxacin (LFX) were from Sigma Chemical Company (St Louis, MO). Sodium phosphate buffer was prepared from reagent-grade products using milli-Q water; the pH of the solutions was measured through a glass electrode and adjusted with NaOH to pH 7.4. Other chemicals were of reagent grade and used as received.

3.4.2. Synthesis of fluoroquinolones

*1-Methyl-7-dimethy1amino-6,8-difluoro-1,4-dihydro-3-quinolinecarboxylic acid (**1**)*. To 5.89 g (21.7 mmol) of ethyl 6,7,8-trifluoro-1,4-dihydro-4-oxo-3-quinolinecarboxylate were added 7.5 g (2.5 equiv.) of K_2CO_3 and 300 mL of dry DMF. After the mixture was stirred for 30 min at 50 °C, 20 ml (*ca*. 11.0 equiv.) of iodomethane were added. The temperature was raised to 80 °C, and the mixture stirred vigorously for 48 h. It was concentrated to dryness and the residue was diluted with dichloromethane and rinsed several times with water. It

was dried and concentrated to yield a dark oil. To 2.2 g (7.4 mmol) of this material were added AcOH (40 mL) and HCl (20 ml, 3N) and the mixture was heated for 5 h. Dilution with water and filtration gave 1.3 g (64 %) of l-methyl-6,7,8-trifluoro-1,4-dihydro-4-oxo-3-quinoline-carboxylic acid.[39]

To 1.00 g (3.5 mmol) of l-methyl-6,7,8-trifluoro-1,4-dihydro-4-oxo-3-quinoline-carboxylic acid in 25 mL of CH_3CN was added a solution of 0.55 g (1.0 equiv.) of 1,8-diazabicyclo[5.4.0]undec-7-ene (DBU) and 1 ml (1.1 equiv.) of dimethylamine in 5 mL of CH_3CN. The mixture was refluxed for 4 h and was stirred at room temperature overnight. Then, the solid was filtered and washed with 20 mL of CH_3CN, 10 mL of 80% aqueous CH_3CN, 20 mL of ethanol, and 20 mL of ether to give 1.01 g (75%) of **1** (amorphous solid).

^{1}H NMR [$CDCl_3$, 300 MHz] δ 2.95 (s, 6H) 4.09 (d, 3H, J=14.7 Hz), 7.8 (d, 1H, J=14.7 Hz), 8.60 (s, 1H). ^{13}C NMR [$CDCl_3$, 75 MHz] δ 42.03, 45.68, 106.27, 107.64, 118.0, 127.06, 134.67, 144.6 (CF, J = 270.25 Hz), 149.75, 153.9 (CF, J = 270.25 Hz), 165.21, 175.23. Exact Mass: m/z found 283.0894, calculated for $C_{13}H_{13}F_2N_2O_3$ (MH^+) 283.0894. The UV-Vis spectra of **1** in **2** mM PB aqueous medium shows λ_{max} at 280 and 320 nm (^{1}H and ^{13}C NMR spectra are shown in Section 3.5).

*1-Ethyl-7-dimethy1amino-6,8-difluoro-1,4-dihydro-3-quinolinecarboxylic acid (**2**)*.[29] The same procedures described above for 1-methyl-7-dimethy1amino-6,8-difluoro-1,4-dihydro-3-

quinolinecarboxylic acid (**1**) were employed to obtain **2** (^{1}H and ^{13}C NMR spectra are shown in Section 3.5).

3.4.3. Emission measurements

The FQ samples were prepared at 1mM PB concentrations starting from a stock solution of 200 mM PB adjusted at pH 7.4. The pH changes were induced adding different amounts of HCl or NaOH (12 M) to the neutral samples. These measurements were performed with a Crison pH-meter.

Fluorescence emission spectra were recorded on a Photon Technology International (PTI) LPS-220B fluorimeter. The fluorescence quantum yields were determined by comparing the areas under the emission curves with that obtained with quinine bisulfate in 1 N H_2SO_4, a widely used fluorescence standard (ϕ_{Fl} = 0.546). Isoabsorptive samples at 310 nm (A_{310nm} = 0.3) were used. All measurements were recorded at room temperature using 1 cm pathway quartz cells with 4 mL capacity.

Phosphorescence spectra were obtained from a Photon Technology International (PTI, TimeMaster TM-2/2003) spectrofluorometer equipped with a pulsed Xe lamp. The apparatus was operated in time-resolved mode, with a delay time of 0.5 ms. For phosphorecence measurements samples similar to those described were used to obtain the fluorescence data.

Singlet-oxygen measurements were performed by registering phosphorescence decay traces at 1270 nm after laser pulse employing

a Peltier-cooled (- 62.8 ºC) Hamamatsu NIR detector operating at 650 V, coupled to a computer-controlled grating monochromator. A pulsed Nd:YAG L52137 V LOTIS TII was used at the excitation wavelength of 355 nm. The single pulses were of ca. 10 ns duration, and the energy was lower than 5 mJ per pulse. The system consisted of the pulsed laser, a 77250 Oriel mono-chromator coupled to the Hamamatsu NIR detector and the oscilloscope connected to the computer. The output signal was transferred from the oscilloscope to a personal computer. All measurements were made at room temperature, under air atmosphere, and using deuterated water at pH *ca.* 7.4 (1mM PB) as solvent in 10 × 10 mm^2 quartz cells with a capacity of 4 mL. The absorbance of the samples was 0.30 at the laser excitation wavelength. Perinaphthenone in water (singlet oxygen quantum yield (ϕ_Δ *ca*. 0.98)40 was used as standard to estimate ϕ_Δ of each compound by comparing the phosphorescence intensities at 1270 nm. The signal was obtained from the average of 50 laser shots. In this context, fresh samples were used every five laser shots to obtain the luminescence of singlet oxygen at 1270 nm.

3.4.4. LFP measurements

A pulsed Nd:YAG SL404G-10 Spectron Laser Systems was used at the excitation wavelength of 355 nm. The single pulses were ~10 ns duration and the energy was lower than 10 mJ/pulse. The detecting light source was a pulsed Lo255 Oriel xenon lamp. The LFP system consisted of the pulsed laser, the Xe lamp, a 77200 Oriel monochromator, an Oriel photomultiplier tube (PMT) system made up

of a 77348 side-on PMT tube, 70680 PMT housing and a 70705 PMT power supply. The oscilloscope was a TDS-640A Tektronix. The output signal from the oscilloscope was transferred to a personal computer.

Unless otherwise stated, all samples used were in aqueous solutions at pH 7.4, and the absorbance was set at 0.3 at 355 nm. Each sample was deaerated by bubbling N_2O in order to remove the solvated electron. Spectra and decays were registered from solutions prepared at different pHs by addition of NaOH or HCl to the neutral buffered solution.

Determination of the quenching rate constants of the intermediates arising from **1** and **2** by sodium bromide (NaBr) were carried out using increasing amounts of the quenchers (from 1 to 400 mM) ensuring that no changes in the pH were induced. Under these conditions more than 99 % of the light was absorbed by the fluoroquinolone.

To determine every FQ quenching rate constant (k_q) the Stern-Volmer equation was applied

$$\frac{1}{\tau} = \frac{1}{\tau_0} + k_q[Q] \qquad \text{Eq. 3.1}$$

where τ_0 is the lifetime of transient species without quencher (Q).

3.4.5. Irradiation procedures and equipment

Irradiations were performed in a multilamp photoreactor equipped with four lamps emitting in the 310-390 nm range (Gaussian

distribution), with a maximum at 350 nm. The photoreactions were performed under anaerobic conditions using FQs (5 x 10^{-5} M) in 1 mM PB aqueous medium and in 2 mM PB/ethanol (50/50). The kinetic studies to determine photodegradation quantum yields of **1**, **2** and LFX and the generation of their photoproducts were performed taking aliquots after 20, 40, 60, 80, 100 and 120 seconds of irradiation. Afterwards, these samples were monitored by HPLC on an analytical C18 column (25 x 0.4 cm, mean particle size 5 µm) with flow rate of 0.7 mL/min and a mixture of acetonitrile/water/trifluoroacetic acid 50/49.9/0.1 was used as eluent.

For *in vitro* phototoxicity assays, the used light source was a photoreactor model LZC-Y equipped with 14 lamps for top and side irradiation (lamps emitting in the 310-390 nm range with a maximum at 350 nm and Gaussian distribution. The irradiation was performed through the lid of a 96 well-plate and in order to avoid overheating, the plates were placed on ice during the irradiation step.

The corresponding photoproducts were initially identified by UPLC-MS/MS. Briefly, the chromatography was performed on an ACQUITY UPLC system (Waters Corp.) with a conditioned autosampler at 4 °C. The separation was carried out on an ACQUITY UPLC BEH C18 column (50 mm × 2.1 mm i.d., 1.7 µm). The column temperature was maintained at 40 °C. The analysis was achieved with gradient elution using acetonitrile and water (containing 0.01% formic acid) as the mobile phase. The Waters ACQUITY™ XevoQToF Spectrometer (Waters Corp.) was connected to the UPLC system *via* an electrospray ionization

(ESI) interface. The ESI source was operated in positive ionization mode with the capillary voltage at 3.0 kV. The temperature of the source and desolvation was set at 100 °C and 400 °C, respectively. The cone and desolvation gas flows were 100 L h^{-1} and 800 L h^{-1}, respectively. All data collected in Centroid mode were acquired using Masslynx™ software (Waters Corp.). Leucine-enkephalin was used as the lock mass generating an $[M+H]^+$ ion (*m/z* 556.2771) at a concentration of 500 pg/mL and flow rate of 50 µL/min to ensure accuracy during the MS analysis.

The photodegradation quantum yields (ϕ_D) were obtained by comparison with the value reported for LFX (*ca.* 0.55), which was used as actinometer.

3.4.6. General procedure to identify photoproducts of 1 and 2

Preparative deaerated irradiations of **1** and **2** (2 x 10^{-3} M) in 2 mM PB/ ethanol (50/50) using the procedure described above were performed to isolate their major photoproducts. Thereby, a solution of **1** (0.283 g in 500 mL of 2 mM PB/ethanol (1/1)) was irradiated for 3 h. Subsequently, the photomixture was acidified with HCl (1N) to pH *ca.* 3 and extracted with CH_2Cl_2 (3 x 25mL). The organic mixture was dried with $MgSO_4$ and concentrated under reduced pressure. Analysis of this photomixture using UPLC-MS/MS revealed the formation of photoproduct **1P** which shows an exact mass (m/z) found 265.0992, calculated for $C_{13}H_{14}FN_2O_3$ (MH^+) 265.0988. However, this compound was unambiguously assigned after photomixture treatment with

(trimethylsilyl)diazomethane, where isolation and characterization were done for its methyl ester **1P´** (methyl 1-methyl-7-dimethy1amino-6-fluoro-1,4-dihydro-3-quinolinecarboxylate). Thus, the photoproduct mixture was treated with 300µL of (trimethylsilyl)diazomethane ($TMSCHN_2$ 2.0 M solution in diethyl ether) in dichloromethane (10 mL) for this aim. The reaction mixture was stirred under N_2 at 40°C for 2h and at room temperature overnight. The reaction mixture was neutralized by adding water (10 mL) and extracted with CH_2Cl_2 (3 x 25mL). The organic mixture was dried over $MgSO_4$ and concentrated under vacuum. Then, this photomixture was submitted to silica gel column chromatography, using 55/30/10/5 of dichloromethane/cyclohexane/acetone/ethanol as mobile phase to isolate 25 mg (9 %) of **1P´** (colorless gum).

Methyl 1-methyl-7-dimethy1amino-6-Fluoro-1,4-dihydro-3-quinolinecarboxylate (**1P´**) ^{1}H NMR [$CDCl_3$, 300 MHz,] δ 2.95 (s, 6H) 3.75 (s, 3H), 3.87 (s, 3H), 6.40 (d, 1H, *J* = 6.9 Hz), 7.92 (d, 1H, *J*=14.7 Hz), 8.30 (s, 1H). ^{13}C NMR [$CDCl_3$, 75 MHz] δ 40.41, 43.29, 51.99, 101.48, 109.74, 113.58, 121.27, 137.48, 144.64, 149.20, 151.95 (CF, *J* = 270.35 Hz), 166.65, 173.12 (^{1}H and ^{13}C NMR spectra are shown in section 3.5). Exact Mass: m/z found 279.1150, calculated for $C_{14}H_{16}FN_2O_3$ (MH^+) 279.1145. The UV-Vis spectrum of **1P´**in 2 mM PB aqueous medium shows λ_{max} at 280 and 320 nm.

Photoproducts **2P1** and **2P2** were directly obtained from a preparative irradiation similar to that described for **1** above but using **2** (296 mg in 500 ml of 2 mM PB/ethanol 1/1 solution). Hence, after 3 h

of sample irradiation, the photomixture was acidified with HCl (1N) to pH *ca.* 3 and extracted with CH_2Cl_2 (3 x 25mL). The organic mixture was dried over $MgSO_4$ and concentrated under vacuum. Afterwards, the photomixture was submitted to silica gel column chromatography, using 55/30/10/5 of dichloromethane/cyclohexane/acetone/ethanol as mobile phase to isolate two amorphous solids, **2P1** 64 mg (23 %) and **2P2** 12 mg (5%).

1,8-(1,2-ethyl)-7-dimethy1amino-6-fluoro-1,4-dihydro-3-quinolinecarboxylic acid (**2P1**) ^{1}H NMR [D_2O, 300 MHz] δ 2.80 (s, 6H) 3.55 (t, 2H, *J*=7 Hz), 4.57 (t, 2H, *J*=7 Hz), 7.30 (d, 1H, *J*=15 Hz), 8.25 (s, 1H). ^{13}C NMR [D_2O, 75 MHz] δ 28.19, 42.79, 52.29, 107.39, 107.73, 118.53, 119.06, 125.10, 141.03, 141.51, 156.30 (CF, *J*= 272.15 Hz), 173.14, 174.75 (^{1}H and ^{13}C NMR spectra are shown in Section 3.5). Exact Mass: m/z found 277.0988, calculated for $C_{14}H_{14}FN_2O_3$ (MH^+) 277.0981. The UV-Vis spectrum of **2P1** in 2 mM PB aqueous medium shows λ_{max} at 280 and 320 nm.

1-ethyl-7-dimethy1amino-6-Fluoro-1,4-dihydro-3-quinolinecarboxylic acid (**2P2**) ^{1}H NMR [$CDCl_3$, 300 MHz] δ 1.45 ((t, 3H, *J*=6.8 Hz), 3.05 (s, 6H) 3.75 (s, 3H), 4.22 (c, 2H, *J*=6.8 Hz), 6.45 (d, 1H, *J*=6.9 Hz), 7.84 (d, 1H, *J*=15.2 Hz), 8.50 (s, 1H). ^{13}C NMR [$CDCl_3$, 75 MHz] δ 14.26, 42.21, 49.20, 100.80, 107.83, 112.65, 118.08, 137.42, 145.72, 146.88, 151.65 (CF, *J*= 270.35 Hz), 167.41, 176.64 (^{1}H and ^{13}C NMR spectra are shown in section 3.5). Exact Mass: m/z found 279.1134, calculated for $C_{14}H_{16}FN_2O_3$ (MH^+) 279.1145. The UV-Vis spectrum of **2P2** in 2 mM PB aqueous medium shows λ_{max} at 280 and 320 nm.

3.4.7. *In Vitro* 3T3 neutral red uptake (NRU) phototoxicity test

BALB/c 3T3 fibroblasts cell line was grown in Dulbecco's Modified Eagle Medium (DMEM) supplemented with 4 mM glutamine, 1% penicillin/streptomycin 10% and Fetal Bovine Serum (FBS) and routinely maintained in exponential growth in 75 cm^2 plastic flasks in a humidified incubator at 37 C under 5% carbon dioxide atmosphere. The 3T3 Neutral Red Uptake Phototoxicity Test was performed as described by the OECD guideline 432 (OECD, 2004) with minor modifications.[35,40] Briefly, two 96-wells plates (2.5×10^4 cells/well) were seeded for each compound. Cells were treated with compounds LFX, **1**, **2** and SDS at several concentrations ranging from 0.5 µM to 500 µM and incubated for 1 h. Afterwards, one plate was irradiated on ice for 11 min to achieve a dose of UVA equivalent to 5 J/cm^2 (UVA LIGHT), whereas the other plate was kept in a dark box (DARK). The viability of UVA-treated control cells in the absence of test compounds was > 90% of those kept in the dark indicating the suitability of the UV dose. After irradiation, the compound solutions were replaced with DMEM medium, and plates were incubated overnight. Subsequently, neutral red solution (50 µg/mL) was added into each well and incubated for 2 h. Cells were washed with PBS and neutral red was extracted in 100 µL with the desorbs solution (water 49% (v/v), ethanol 50% (v/v) and acetic acid 1% (v/v). Then, the absorbance was measured at 550 nm on a Multiskan Ex microplate reader. For each compound dose-response curves were established in order to determine the concentration of the compound producing a 50% reduction of the neutral red uptake (IC_{50}) in the dark

and light. In the end, Photo-Irritation-Factor (PIF) was determined using the following equation:

$$PIF = \frac{IC_{50}\ DARK}{IC_{50}\ UVA\ LIGHT} \qquad \text{Eq. 3.2}$$

According to the OECD Test Guideline (OECD, 2004)[35] a chemical is predicted as phototoxic if PIF is > 5, probably phototoxic if PIF > 2 and < 5, and non-phototoxic when PIF < 2. Sodium dodecyl sulphate (SDS) was used as negative control and lomefloxacin (LFX) was used as an established phototoxic reference compound.[19,21]

3.4.8. Cellular localization studies by confocal microscopy

Firstly, FSK cells were seeded on glass coverslips in 24 well-plates (5.0×10^4 cells/well). Next day, DMEM medium was replaced by 500 µL of compound solutions (LFX, **1** and **2**) at 200 µM and incubated for 2 h at 37ºC. Then, coverslips were washed once for 5 min with PBS and finally mounted using Mowiol. Microscopy and imaging were performed with a Leica SP5 confocal microscope (Leica, Germany) using sequential mode. Representative images were selected from at least three different regions on the slide.

3.5. NMR Spectra

^{1}H Compound 1

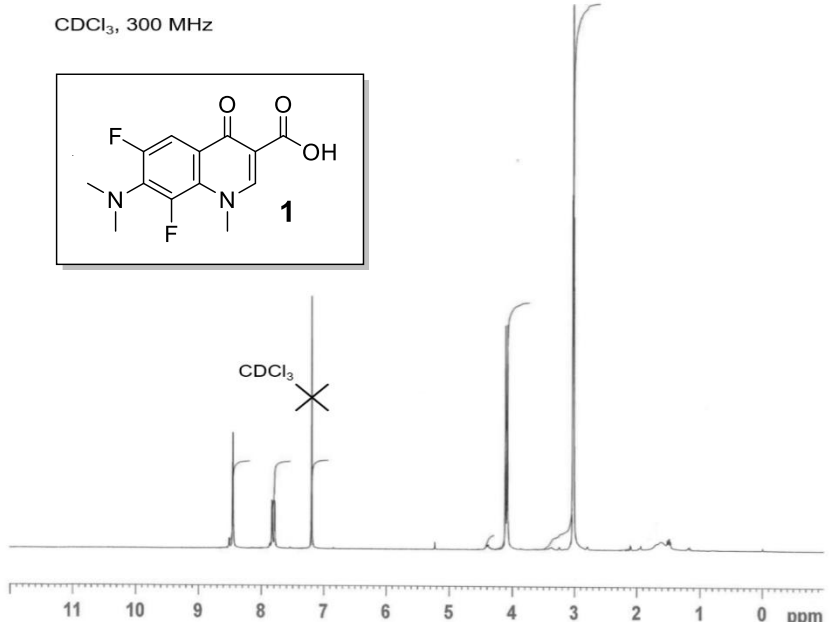

^{13}C Compound 1

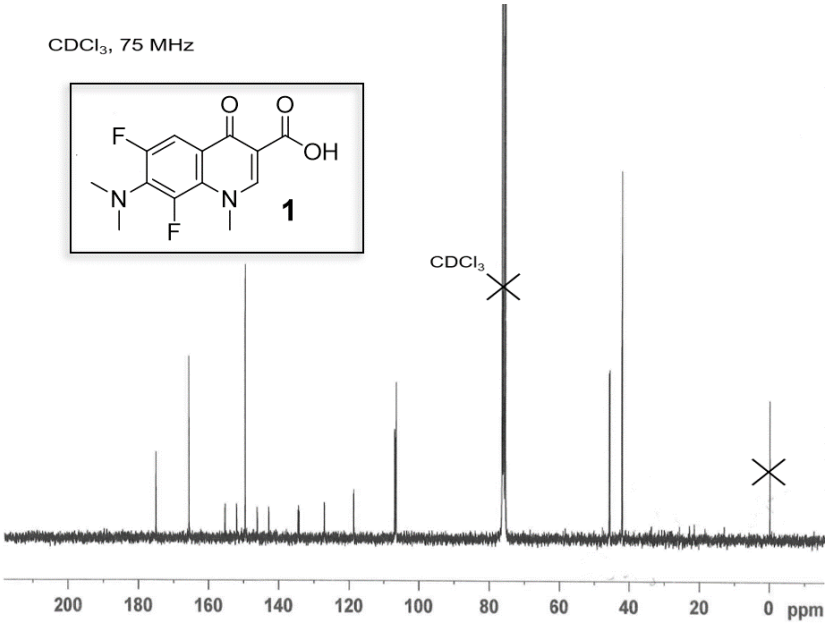

^{1}HCompound 1P’

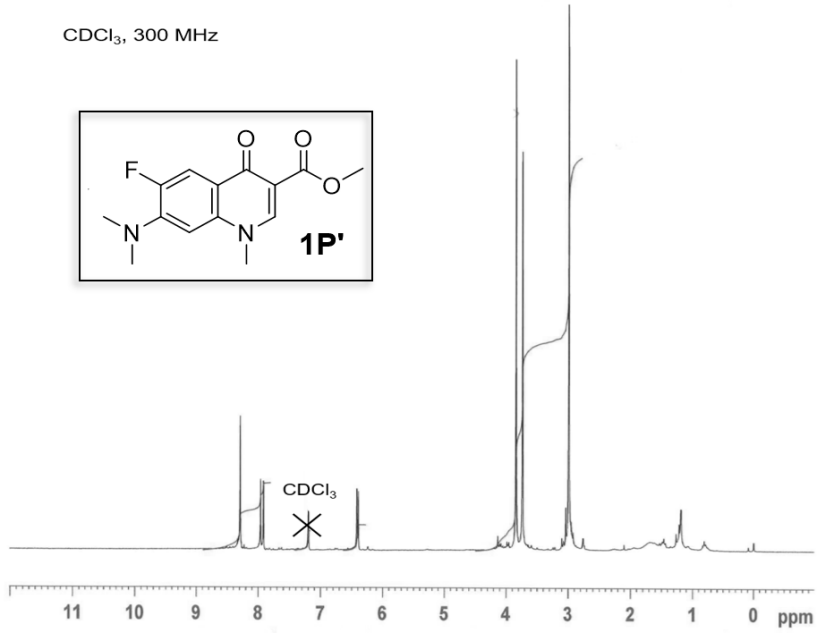

^{13}C Compound 1P'

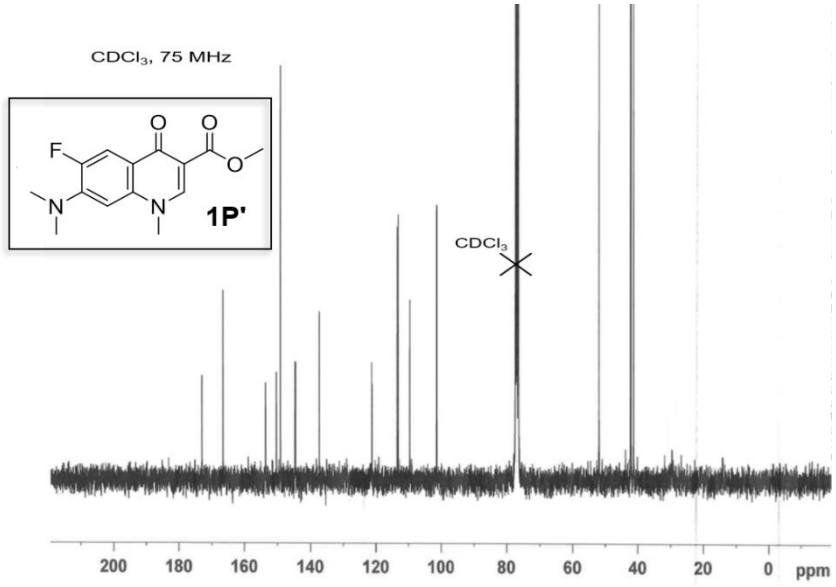

^{1}H Compound 2P1

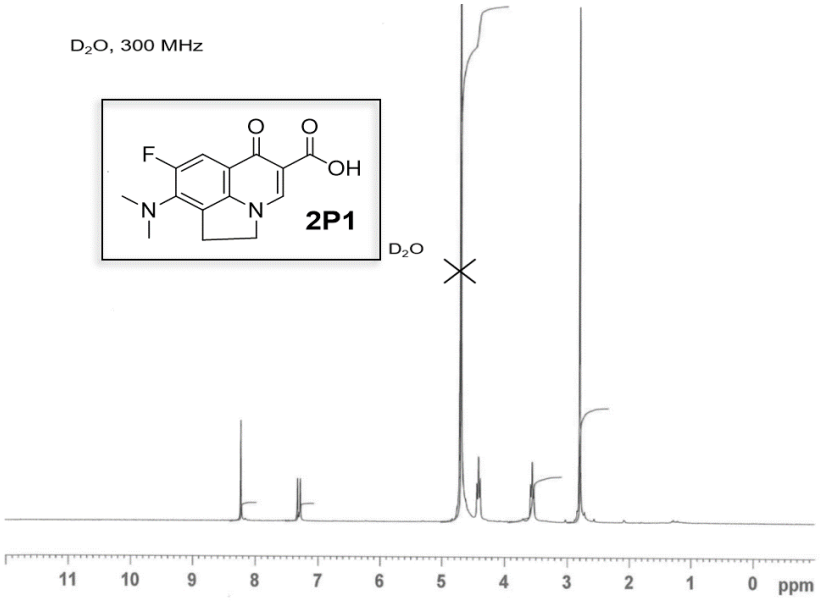

^{13}C Compound 2P1

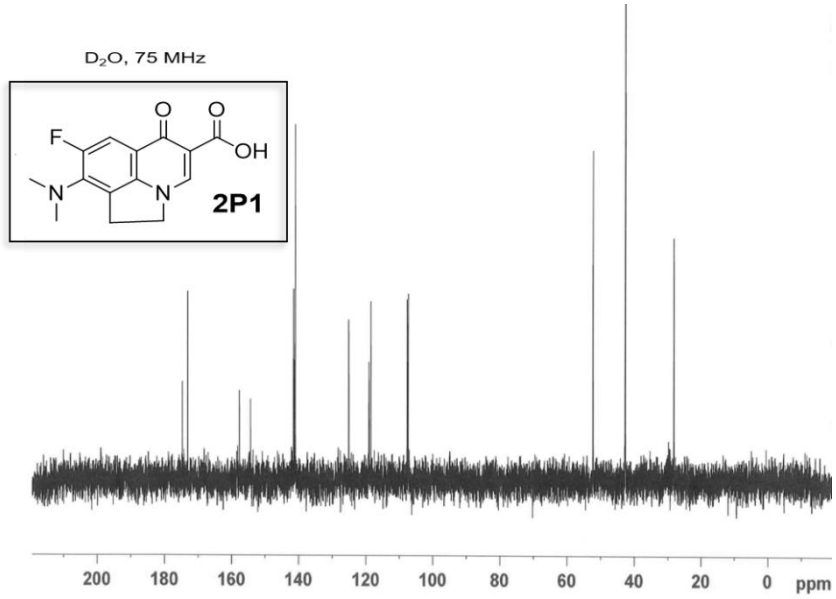

^{1}HCompound 2P2

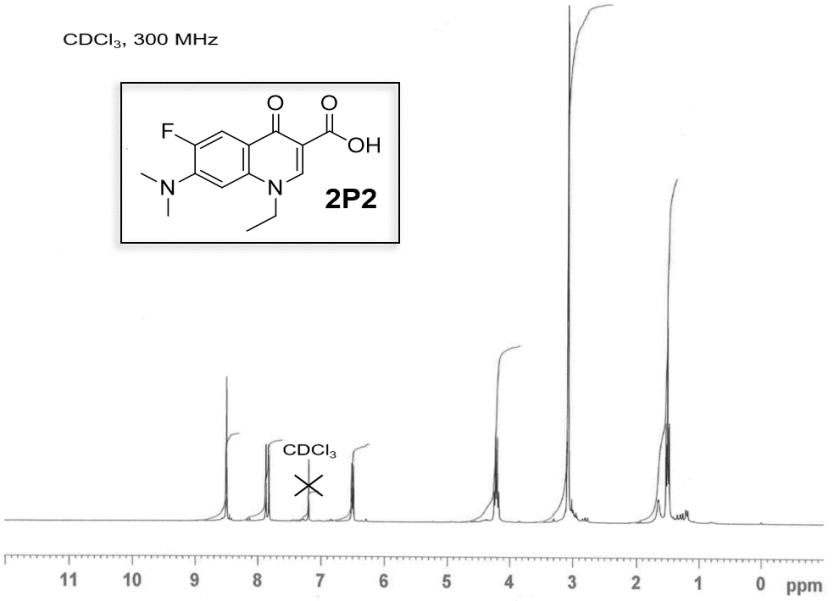

^{13}C Compound 2P2

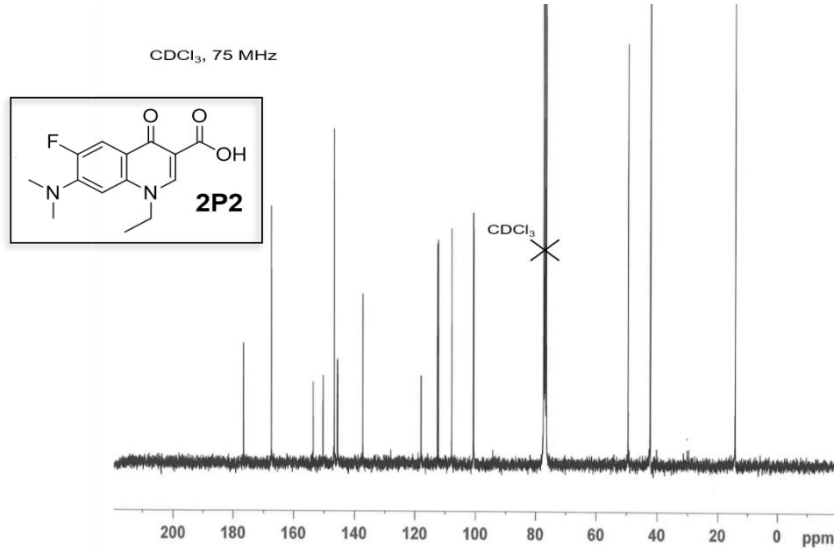

3.6. References

1. Ahmed A, Daneshtalab M. Nonclassical biological activities of quinolone derivatives. *J Pharm Pharm Sci*. 2011;15(1):52-72.
2. Domagala JM, Hanna LD, Heifetz CL, et al. New Structure-Activity Relationships of the Quinolone Antibacterials Using the Target Enzyme. The Development and Application of a DNA Gyrase Assay. *J Med Chem*. 1986;29(3):394-404.
3. Kang D-H, Kim J-S, Jung M-J, et al. New insight for fluoroquinophenoxazine derivatives as possibly new potent topoisomerase I inhibitor. *Bioorg Med Chem Lett*. 2008;18(4):1520-1524.
4. Azéma J, Guidetti B, Dewelle J, et al. 7-((4-Substituted)piperazin-1-yl) derivatives of ciprofloxacin: Synthesis and in vitro biological evaluation as potential antitumor agents. *Bioorganic Med Chem*. 2009;17(15):5396-5407.
5. Cullen M, Baijal S. Prevention of febrile neutropenia: Use of prophylactic antibiotics. *Br J Cancer*. 2009;101:S11-S14.
6. Kim K, Pollard JM, Norris AJ, et al. High-throughput screening identifies two classes of antibiotics as radioprotectors: Tetracyclines and fluoroquinolones. *Clin Cancer Res*. 2009;15(23):7238-7245.
7. Al-Trawneh SA, Zahra JA, Kamal MR, et al. Synthesis and biological evaluation of tetracyclic fluoroquinolones as antibacterial and anticancer agents. *Bioorganic Med Chem*. 2010;18(16):5873-5884.
8. Aldred KJ, Schwanz HA, Li G, et al. Activity of quinolone CP-115,955 against bacterial and human type ii topoisomerases is mediated by different interactions. *Biochemistry*. 2015;54(5):1278-1286.
9. Pommier Y, Leo E, Zhang H, Marchand C. DNA topoisomerases

and their poisoning by anticancer and antibacterial drugs. *Chem Biol*. 2010;17(5):421-433.

10. Palumbo M, Gatto B, Zagotto G, Palù G. On the mechanism of action of quinolone drugs. *Trends Microbiol*. 1993;1(6):232-235.
11. Paul M, Gafter-Gvili A, Fraser A, Leibovici L. The anti-cancer effects of quinolone antibiotics? *Eur J Clin Microbiol Infect Dis*. 2007;26(11):825-831.
12. Perrone CE, Takahashi KC, Williams GM. Inhibition of human topoisomerase IIalpha by fluoroquinolones and ultraviolet A irradiation. *Toxicol Sci*. 2002;69(1):16-22.
13. Lhiaubet-Vallet V, Bosca F, Miranda MA. Photosensitized DNA Damage: The Case of Fluoroquinolones. *Photochem Photobiol*. 2009;85(4):861-868.
14. Marrot L, Belaïdi JP, Jones C, et al. Molecular responses to photogenotoxic stress induced by the antibiotic lomefloxacin in human skin cells: From DNA damage to apoptosis. *J Invest Dermatol*. 2003;121(3):596-606.
15. JR M, A S, L M. Photogenotoxicity of mammalian cells: a review of the different assays for in vitro testing. *Photochem Photobiol*. 2002;75(5):437-447.
16. Martinez LJ, Li G, Chignell CF. Photogeneration of fluoride by the fluoroquinolone antimicrobial agents lomefloxacin and fleroxacin. *Photochem Photobiol*. 1997;65(3):599-602.
17. Chignell CF, Haseman JK, Sik RH, Tennant RW, Trempus CS. Photocarcinogenesis in the Tg.AC mouse: lomefloxacin and 8-methoxypsoralen. *Photochem Photobiol*. 2003;77(1):77-80.
18. Fasani E, Profumo A, Albini A. Structure and Medium-Dependent Photodecomposition of Fluoroquinolone Antibiotics. *Photochem Photobiol*. 1998;68(5):666-674.
19. Jeffrey AM, Shao L, Brendler-Schwaab SY, Schlüter G, Williams GM. Photochemical mutagenicity of phototoxic and photochemically carcinogenic fluoroquinolones in comparison with the photostable moxifloxacin. *Arch Toxicol*.

2000;74(9):555-559.

20. Spratt TE, Schultz SS, Levy DE, Chen D, Schlüter G, Williams GM. Different mechanisms for the photoinduced production of oxidative dna damage by fluoroquinolones differing in photostability. *Chem Res Toxicol*. 1999;12(9):809-815.
21. Reus AA, Usta M, Kenny JD, et al. The in vivo rat skin photomicronucleus assay: phototoxicity and photogenotoxicity evaluation of six fluoroquinolones. *Mutagenesis*. 2012;27(6):721-729.
22. Soldevila S, Bosca F. Photoreactivity of fluoroquinolones: Nature of aryl cations generated in water. *Org Lett*. 2012;14(15):3940-3943.
23. Cuquerella MC, Miranda MA, Boscá F. Generation of detectable singlet aryl cations by photodehalogenation of fluoroquinolones. *J Phys Chem B*. 2006;110(13):6441-6443.
24. Freccero M, Fasani E, Mella M, Manet I, Monti S, Albini A. Modeling the Photochemistry of the Reference Phototoxic Drug Lomefloxacin by Steady-State and Time-Resolved Experiments, and DFT and Post-HF Calculations. *Chem - A Eur J*. 2008;14(2):653-663.
25. Albini A, Monti S. Photophysics and photochemistry of fluoroquinolones. *Chem Soc Rev*. 2003;32(4):238-250.
26. Fasani E, Manet I, Capobianco ML, Monti S, Pretali L, Albini A. Fluoroquinolones as potential photochemotherapeutic agents: Covalent addition to guanosine monophosphate. *Org Biomol Chem*. 2010;8(16):3621-3623.
27. Soldevila S, Cuquerella MC, Bosca F. Understanding of the photoallergic properties of fluoroquinolones: Photoreactivity of lomefloxacin with amino acids and albumin. *Chem Res Toxicol*. 2014;27(4):514-523.
28. Soldevila S, Consuelo Cuquerella M, Lhiaubet-Vallet V, Edge R, Bosca F. Seeking the mechanism responsible for fluoroquinolone photomutagenicity: A pulse radiolysis, steady-

state, and laser flash photolysis study. *Free Radic Biol Med*. 2014;67:417-425.

29. Sarma MR, Kumar V, Prasad ASR, et al. Synthesis and Biological Activity of Novel Antibacterial Quinolones *T*. Vol 40.; 2001.
30. Martínez LJ, Sik RH, Chignell CF. Fluoroquinolone antimicrobials: singlet oxygen, superoxide and phototoxicity. *Photochem Photobiol*. 1998;67(4):399-403.
31. Fasani E, Monti S, Manet I, et al. Inter-and intramolecular photochemical reactions of fleroxacin. *Org Lett*. 2009;11(9):1875-1878.
32. Belvedere A, Boscá F, Catalfo A, Cuquerella MC, De Guidi G, Miranda MA. Type II guanine oxidation photoinduced by the antibacterial fluoroquinolone rufloxacin in isolated DNA and in 2′-deoxyguanosine. *Chem Res Toxicol*. 2002;15(9):1142-1149.
33. Cuquerella MC, Boscá F, Miranda MA, Belvedere A, Catalfo A, De Guidi G. Photochemical properties of ofloxacin involved in oxidative DNA damage: A comparison with rufloxacin. *Chem Res Toxicol*. 2003;16(4):562-570.
34. Monti S, Sortino S. Laser flash photolysis study of photoionization in fluoroquinolones. *Photochem Photobiol Sci*. 2002;1(11):877-881.
35. Palumbo F, Garcia-Lainez G, Limones-Herrero D, et al. Enhanced photo(geno)toxicity of demethylated chlorpromazine metabolites. *Toxicol Appl Pharmacol*. 2016;313:131-137.
36. Seto Y, Inoue R, Ochi M, Gandy G, Yamada S, Onoue S. Combined use of in vitro phototoxic assessments and cassette dosing pharmacokinetic study for phototoxicity characterization of fluoroquinolones. *AAPS J*. 2011;13(3):482-492.
37. Sauvaigo S, Douki T, Odin F, Caillat S, Ravanat J-L, Cadet J. Analysis of Fluoroquinolone-mediated Photosensitization of 2′-Deoxyguanosine, Calf Thymus and Cellular DNA: Determination of Type-I, Type-II and Triplet-Triplet Energy Transfer Mechanism Contribution¶. *Photochem Photobiol*. 2007;73(3):230-237.

38. Cuquerella MC, Lhiaubet-Vallet V, Cadet J, Miranda MA. Benzophenone photosensitized DNA damage. *Acc Chem Res*. 2012;45(9):1558-1570.
39. Domagala JM, Heifetz CL, Hutt MP, et al. 1-Substituted 7-[3-[(Ethylamino)methyl]-1-pyrrolidinyl]-6,8-difluoro-1,4-dihydro-4-oxo-3-quinolinecarboxylic Acids. New Quantitative Structure-Activity Relationships at N1 for the Quinolone Antibacterials. *J Med Chem*. 1988;31(5):991-1001.
40. Garcia-Lainez G, Martínez-Reig AM, Limones-Herrero D, Consuelo Jiménez M, Miranda MA, Andreu I. Photo(geno)toxicity changes associated with hydroxylation of the aromatic chromophores during diclofenac metabolism. *Toxicol Appl Pharmacol*. 2018;341:51-55.

Chapter 4. Effects of fluoroquinolones structural modifications on their photosensitizing properties

4.1. Introduction

Fluoroquinolones (FQ) are quinolinic derivatives with an aminoalkyl substituent (Chart 4.1). They are widely used as antibacterial agents because they develop their pharmacological activity through the inhibition of Topoisomerase II, a bacterial enzyme involved in the replication and repair of bacterial DNA. [1] A large number of studies about the effect of the structural modifications of FQs on the antimicrobial activity of this type of drugs have been conducted.[2] Thus, it has been observed that modifications on positions 1, 2 , 5, 7 and 8 of the quinolinic ring affect the antimicrobial activity of FQs and consequently their affinity to biomolecules. In this context, most of the modifications also affect the photochemical and photobiological properties associated to these drugs.[3] During the last years FQ have raised much attention due to their antitumoral activity.[4–8] In *vitro* and in *vivo* studies have confirmed anti-cancer effects of quinolone antibiotics supporting the observation that FQs reduce all-cause mortality among cancer patients.[9] The direct anti-tumor effect of FQs has also been associated with the inhibition of mammalian enzymes such as deoxyribonucleic acid topoisomerase I, topoisomerase II and DNA polymerase. Interestingly, the genotoxic effects exhibited by FQs in eukaryotic systems are enhanced by UV irradiation,[10] which confers to these type of drugs a potential property as photochemotherapeutic agents. In fact, photoinduced genotoxicity has remarkably been detected in 6,8-dihalogenated FQs such as fleroxacin, BAY y3118 and lomefloxacin (LFX, compound proposed as photomutagenic standard,

Chart 4.1).[11–17] Moreover, it has been clearly observed that these drugs also produce photoxicity and photoallergy.[18,19] Thereby, a large number of studies concerning the photochemical and photobiological properties of FQs bearing a further halogen atom at position 8 of the quinolinic ring have been carried out during the last few years.[14–26] All of them have shown an unusual photodehalogenation by heterolysis of the strong C_8-halogen bond from the triplet excited state of FQ (^{3}FQ) leading to the generation of an aryl cation with alkylating properties.[20–26] However, other intermediates can also be generated when dihalogenated fluoroquinolones are associated with biomolecules.[21,22] Several processes can be involved in the photosensitized biomolecular damage produced by FQs. Thus, photooxidation of DNA is the main damage caused by its association with FQs, while in proteins, such as albumin, a photobinding occurs between the protein and the FQ. [21,22]

A recent study designed a new 6,8 dihalogenated quinolone **1** (*1-methyl-6,8-difluoro-4-oxo-7-aminodimethyl-1,4-dihydroquinoline-3-carboxylic acid*) for improving the phototoxic properties of fluoroquinolones by increasing the alkylating properties of the quinolinic structure.[27] However, although this property was clearly proved and correlated with a higher phototoxic effect than those observed for close related FQs, the affinity of these compounds to biomolecules was not evaluated and their knowledge could allow to design new compounds with improved phototoxic effects. With this background, the aim of the present study is to analyze the effect of small structural modifications in the main ring of four FQs (see in chart

4.1 LFX, ACLFX, compound **1** and **2**) which can modify their binding affinity to biomolecules and consequently, the photochemical processes involved in their phototoxic effects.

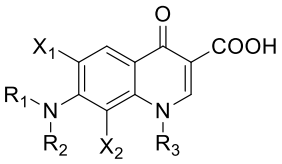

	LFX	ACLFX	FLX	BAY	1	2
R_1, R_2	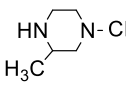	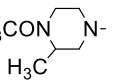	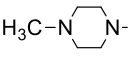	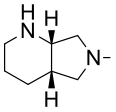	$(CH_3)_2N$-	$(CH_3)_2N$-
R_3-	CH_3CH_2–	CH_3CH_2–	CH_2FCH_2–		CH_3–	CH_3CH_2–
X_1–	F	F	F	F	F	F
X_2–	F	F	F	Cl	F	F

Chart 4.1. Chemical structure of dihalogenated FQs

4.2. Results and discussion

4.2.1. Study of the interactions between FQ and biomolecules using emission measurements

Fluorescence lifetimes of FQs were registered at λ_{ex} 350 nm (an isosbestic wavelength of their absorption spectra with increasing amounts of DNA) with and without the presence of DNA (10^{-3} M in nucleotide) to evaluate the possible involvement of a dynamic quenching in their emissions. Hence, the emission lifetimes of LFX, ACLFX, **1** and **2** were 1.2, 1.4, 1.2 and 1.3 ns respectively and they do not show any change by the presence of DNA. These results, in agreement with data described in the literature for LFX and ACLFX,[22]

discard any dynamic fluorescence quenching process. Moreover, the static emission quenching of FQs was also analyzed to determine the possibility of binding of FQs to DNA. The evolution of emission spectra of aqueous solutions of each FQ in the presence of different DNA quantities showed low emission decreases for all compounds. Figure 4.1 displays the fluorescence spectra obtained for compound **1** and **2**. Thus, the K_{sv} for each FQ was calculated from Equation 4.1 assuming that the FQ complexed to DNA (FQ…DNA) does not emit. Results are shown in Table 4.1. The equilibrium constants for the complex formation estimated for LFX…DNA and for ALFX…DNA were similar to those described in the literature. In this context, compound **2** showed a Stern-Volmer constant (K_{sv}) very similar to that obtained for ACLFX while a very low K_{sv} value obtained for **1** evidenced the absence of any type of complexation between DNA and **1**. Consequently, polarity decreases of the FQs, such as the *N*(4')-acetylation of the piperazinyl ring or the absence of this substituent, diminishes FQ affinity to DNA. Interestingly, the absence of complexation observed for **1** would be attributed to the change of an ethyl at the *N*(1) position of the quinolinic ring by a methyl substituent.

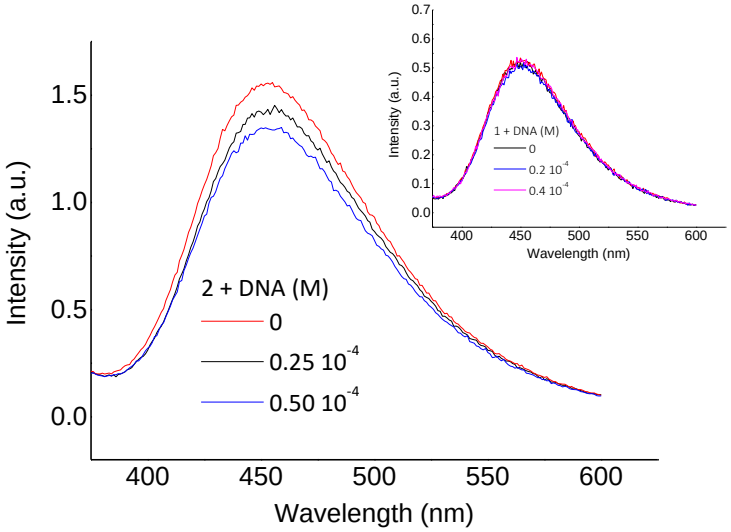

Figure 4.1. Fluorescence quenching of **2** by the presence of different amounts of DNA (molar concentrations of nucleotides) in aqueous media. Inset: Effect of increasing amounts of DNA in the fluorescence of **1** under similar conditions.

Table 4.1. Stern-Volmer constants of biomolecules (DNA, HSA) with FQs in neutral aqueous media (PB 1 mM) and percentage of HSA-FQ photoadduct generated in the irradiations of aqueous solutions of FQ in HSA.

	1	**2**	**ACLFX**	**LFX**
DNA[a] K_{SV} (M^{-1})	>30	332	435	1300
HSA[b] K_{SV} (M^{-1})	4.1×10^4	4.8×10^4	4.8×10^4 (1×10^4)[a]	2.3×10^3 (2.6×10^3)[a]
PHOTOADDUCT HSA-FQ (%)	11 ± 1	7 ± 1	5 ± 1	1.5 ± 1

[a]; Values determined from FQ fluorescence quenching by biomolecules. [b]; Values determined from HSA fluorescence quenching by FQs.

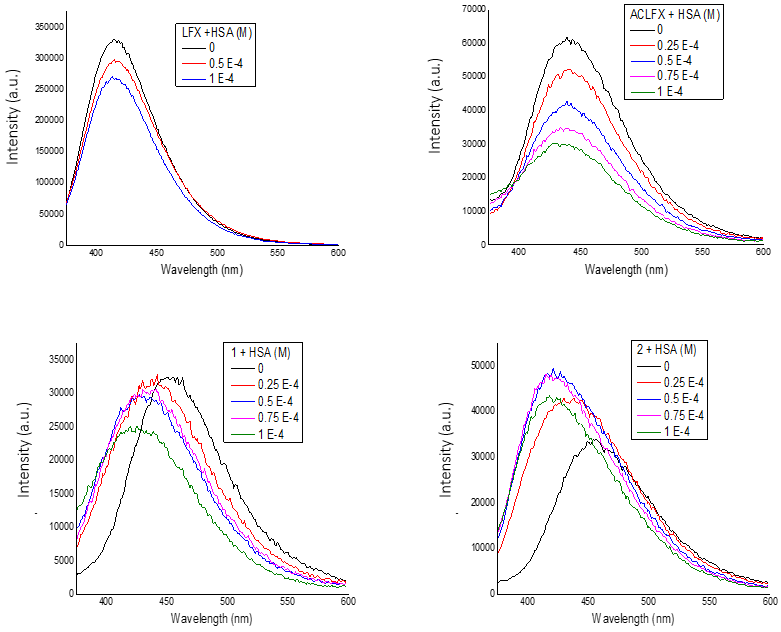

Figure 4.2. Effect of increasing amounts of HSA in the fluorescence of FQ aqueous solutions.

FQs fluorescence quenching by HSA was carried out by addition of albumin (up to 10^{-4} M) to 7.5 x 10^{-5} M FQ solutions using λ_{ex} 310 nm (it is an isosbestic wavelength of the absorption spectra of FQ with increasing amounts of HSA) with the aim of determining more accurately the HSA…FQ binding constants. Figure 4.2 shows the results of the FQs fluorescence intensities adding different amounts of albumin. As expected for ACLFX, its emission is quenched more efficiently than that of LFX.[28] By contrast, the effect observed for compounds **1** and **2** was a blue shift of their emissions, which indicates that they are also associated with albumin but without a clear interaction between the singlet excited state of these FQs because

emission quenching of compounds **1** and **2** by HSA does not apparently occur. In this context, fluorescence lifetime (τ_F) of all FQs did not show any change by the addition of 10^{-4} M HSA. Thus, the static fluorescence quenching observed for LFX and ACLFX can only be attributed to the singlet excited state reactivity of LFX and ACLFX (^{1}LFX and ^{1}ACLFX) with albumin when this FQs are associated with HSA because there is not any involvement of a dynamic process in the emissions quenching of both FQs. Contrarily, ^{1}**1** and ^{1}**2** do not react with albumin although FQs…HSA complexes are also formed. With these results and assuming that the LFX and ACLFX bounds to HSA do not emit, K_{sv} was only determined for the formation of the complex between HSA and LFX or ACLFX as a simple model to obtain their association constants (K_a). These values, shown in Table 4.1, were obtained using Equation 4.2 and they are in agreement with data of the literature.[21,29]

In this context, emission quenching of the Trp unit present in HSA is often used to obtain information about FQ…albumin associations. The Trp fluorescence band is centered at *ca*. 344 nm and it is exclusively exhibited by albumin after excitation at 295 nm.[30] Hence, the experiments were performed using 10^{-5} M HSA in aqueous solutions (10^{-3} M PB, pH *ca.* 7.4) by adding different amounts of FQ (between 10^{-6} and 1.2 x 10^{-5} M). Correction for the inner filter effect (IFE) was applied before analysis of the results because the FQs show absorption at the excitation and emission wavelengths (more details are provided in the experimental section).

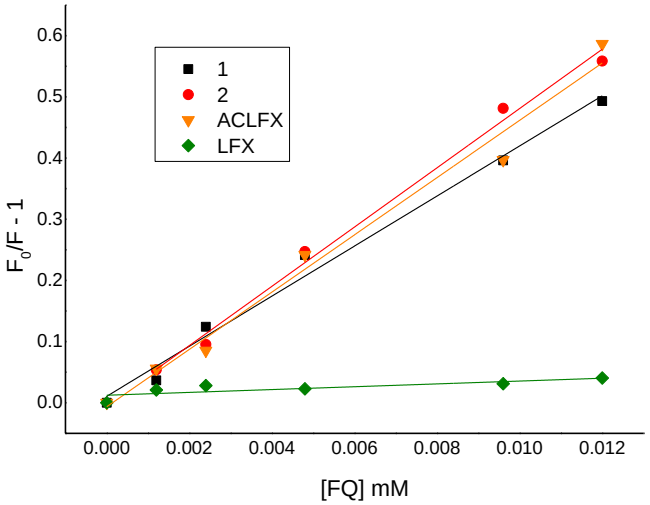

Figure 4.3. Stern-Volmer plots of HSA fluorescence versus FQs.

The K_{sv} of the experiments were calculated from the slope of the plot F_0/F versus [Q] of Figure 4.3. Results showed in Table 4.1 and Figure 4.3 revealed that the interactions between HSA and FQs such as ACLFX or **1** or **2** are higher than those produced between HSA and LFX. In static quenching processes, the K_{sv} values correspond to the total association constant of quencher to the protein when the quencher totally suppresses the intrinsic protein fluorescence.[31] Therefore, the resulting K_{sv} are a good approximation for FQ…albumin association constants.[32]

It was established that *N*-acetylation of LFX produces an increase in the affinity predominantly for site II,[22] which could also be occurring for **1** and **2**. Moreover, these results are also fully consistent with the preferential affinity of nalidixic acid (a quinolone lacking a piperazinyl

ring) for site II of HSA.[33] In fact, it is reasonable that a cationic piperazinyl ring increases FQ affinity for aqueous media.

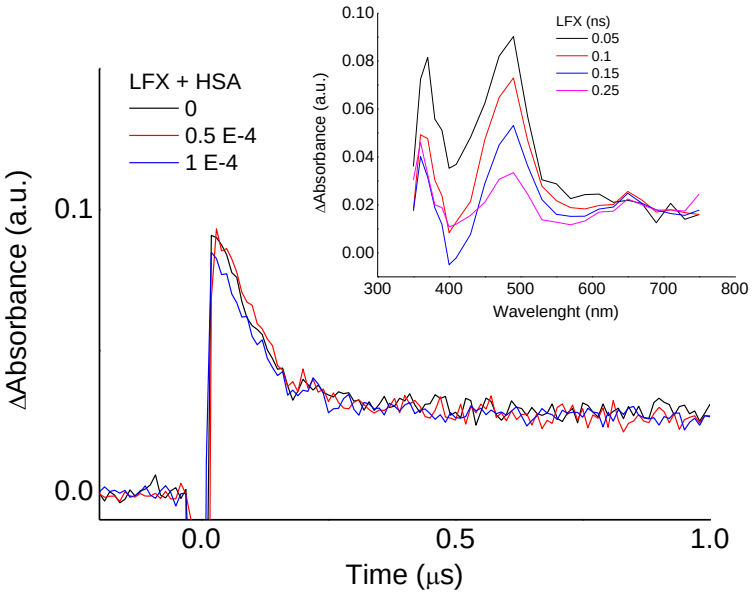

Figure 4.4. Decay traces of LFX at 490 nm in the presence of different concentrations of HSA under anaerobic (N_2O) aqueous media. Inset; Transient absorption spectra of LFX aryl cation generated after the laser pulse at 355 nm under anaerobic (N_2O) aqueous media.

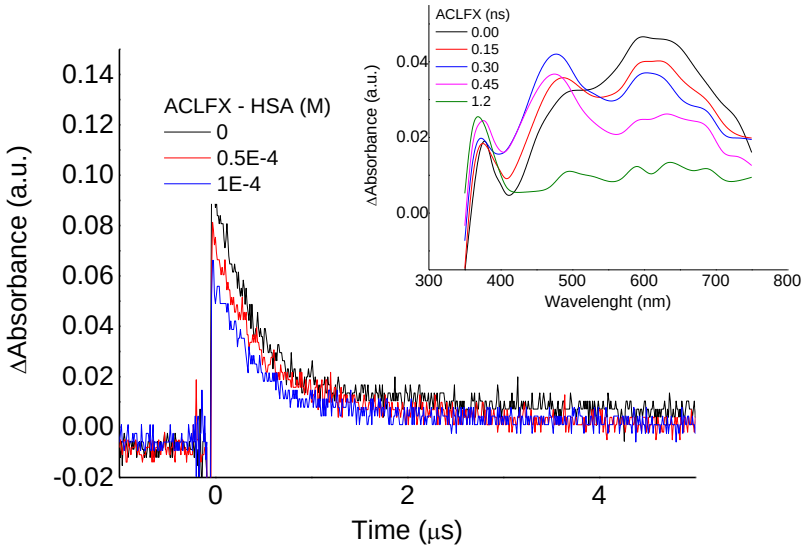

Figure 4.5. Decay traces of ACLFX at 600 nm in the presence of different concentrations of HSA under anaerobic (N_2O) aqueous media. Inset; Transient absorption spectra of ACLFX aryl cation generated after the laser pulse at 355 nm under anaerobic (N_2O) aqueous media.

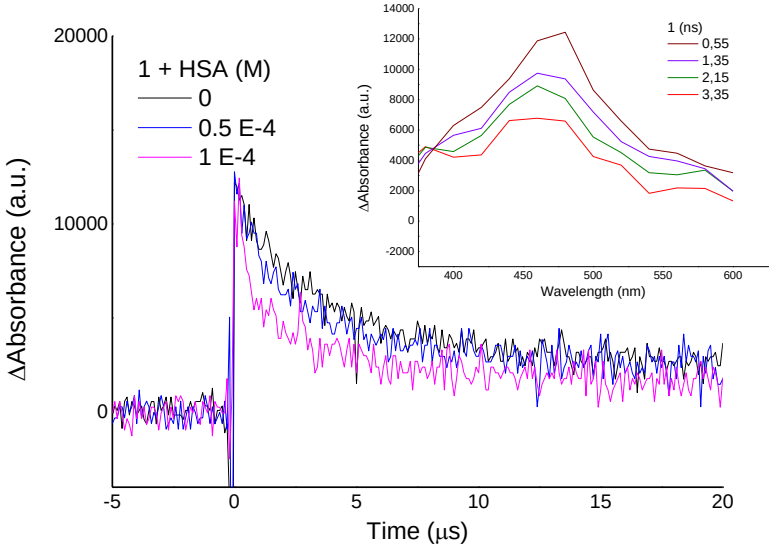

Figure 4.6. Decay traces of **1** at 480 nm in the presence of different concentrations of HSA under anaerobic (N_2O) aqueous media. Inset; Transient absorption spectra of **1** aryl cation generated after the laser pulse at 355 nm under anaerobic (N_2O) aqueous media.

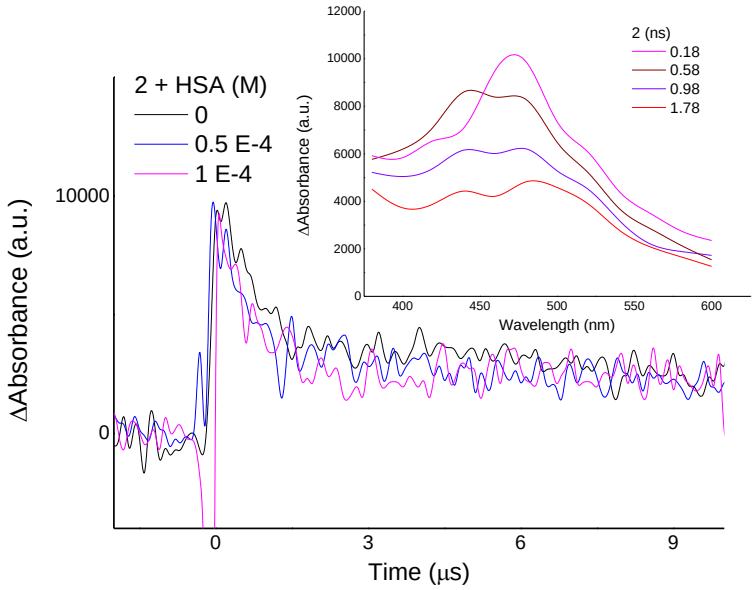

Figure 4.7. Decay traces of **2** at 490 nm in the presence of different concentrations of HSA under anaerobic (N_2O) aqueous media. Inset; Transient absorption spectra of **2** aryl cation generated after the laser pulse at 355 nm under anaerobic (N_2O) aqueous media.

4.2.2. Reactivity of FQ aryl cations with HSA

In agreement with the literature, when photolysis of aqueous solutions of LFX and ACLFX, **1** and **2**, were performed at pH = 7.4 under N_2O, generation of aryl cations of LFX (λ_{max} = 490 nm and τ *ca*. 200 ns), ALFX (λ_{max} = 600 nm and τ *ca*. 340 ns), **1** (λ_{max} = 480 nm and τ *ca*. 3.1 μs) and **2** (λ_{max} = 480 nm and τ *ca*. 300 ns) were registered.[23–25,27]

Decays traces and transient absorption spectra of all of them are shown in Figures 4.4, 4.5, 4.6 and 4.7. Laser excitation of FQs (10^{-4} M) in 1 mM PB solutions (10^{-4} M, pH *ca*. 7.4) under N_2O atmosphere

displayed the same transient absorption species in the absence and the presence of HSA (up to 10^{-4} M). The aryl cations lifetime of LFX and ACLFX remained nearly unaltered. However, the generation of these intermediates resulted to be lower when HSA was added, being this effect the most important for the ALFX aryl cations (see the absorption of the decays in Figure 4.4 and 4.5). In the case of **1** and **2** this effect was not observed but changes in the lifetime of their aryl cations were detected (see Figure 4.6 and 4.7).

The observed absorption of LFX and ACLFX aryl cations decreases at its λ_{max} by addition of HSA, which can be understood considering this biomolecule-drug equilibrium:

$$[FQ] + [HSA] \underset{K_d}{\overset{K_a}{\rightleftharpoons}} [FQ\cdots HSA]$$

in Equation 4.1:

$K_a = [FQ...HSA] / ([HSA] \times [FQ])$ Eq. 4.1

Thus, applying the K_a determined for ACLFX and LFX by fluorescence quenching in equation 4.1, and assuming the reactivity of ^{1}ACLFX and ^{1}LFX with albumin, can be understood the decrease in the generation of the corresponding to their aryl cations. In the case of ^{1}**1** and ^{1}**2**, as they do not react with albumin, this effect is not observed.

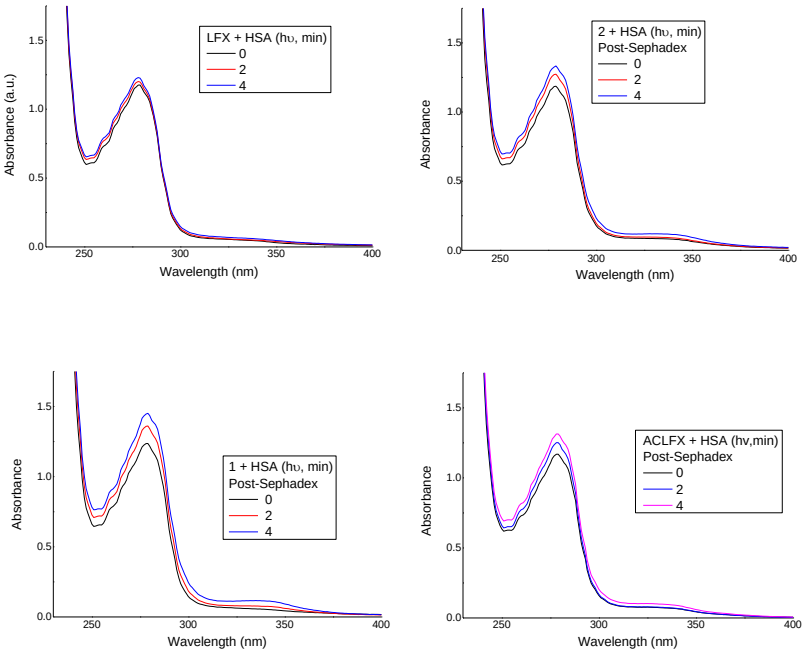

Figure 4.8. Absorption spectra of FQs aqueous solutions in the presence of HSA (1/1) after Sephadex chromatography.

4.2.3. Covalent binding of FQs to HSA

Formation of adducts between HSA and FQs was detected when the corresponding photomixtures were analyzed after gel filtration with Sephadex using UV-Vis spectrometry. Filtered samples of HSA obtained from irradiated solutions (2 and 4 minutes) of FQs in the presence of albumin showed changes in their absorption spectra (results are shown in Figure 4.8). The filtered samples of control experiments (no light) with only (A)LFX or HSA showed no absorption from 300 nm to 400 nm in any case. The amount of FQ-albumin adducts produced during the

irradiation time of each FQ solution in the presence of HSA was determined from their corresponding absorption spectra. Results, shown in Table 4.1, revealed that **1** photobinding is more efficient for those detected for **2** and ACLFX. The photobinding obtained for LFX was the lowest. These results would be correlated with two previous findings: a) the K_a values determined for the FQs with HSA (table 4.1), where there is very low association between LFX and HSA and b) the reactivity detected in the laser flash photolysis experiments for the singlet excited state of ACLFX and the aryl cations for **1** and **2** with albumin. Thus, as it can be observed in Figures 4.4-4.7, while the presence of albumin in the aqueous samples of LFX did not produce any change in its decay traces, an absorption decrease in the ACLFX decay traces and fast decay traces for **1** and **2** was observed using the same experimental conditions with ACLFX, **1** and **2**.

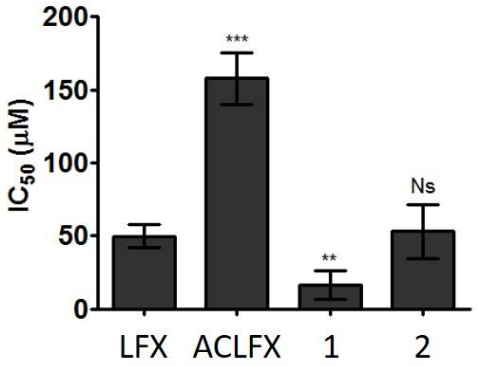

Figure 4.9. Phototoxicity of LFX in the 3T3 NRU Assay. 3T3 cells were treated with serial dilutions of LFX or related compounds for 1h, followed of a 5 J/cm^2 UV light irradiation. CPZ was used as a positive control of phototoxicity and SDS

as a negative control. IC_{50} values were calculated by non-lineal regression with GraphPad Prism 5.0. Data represent Mean±SD from four independent experiments and asterisks correspond to significant differences relative to the IC_{50} LFX by the T-Student test (**p<0,01; ***p<0,001; Ns: non-statistically significant.).

Table 4.2. *In vitro* 3T3 NRU assay of LFX, ACLFX, **1** and **2** with different UVA light dosis.

IC_{50} (μM)				
	DARK	0,2 J/cm^2	0,5 J/cm^2	5 J/cm^2
LFX	>500	543	348	53
ACLFX	>500	>500	>500	153
1	>500	270	192	19
2	>500	311	283	66

4.2.4. Phototoxic properties of FQs

Cell viability upon incubation with LFX, ACLFX, **1** and **2** in combination with UVA light was assessed by the in vitro 3T3 NRU phototoxicity test. Cytotoxicity profiles of BALB/c 3T3 fibroblasts treated with FQs were measured in the presence and absence of UVA light, using neutral red as vital dye, and half maximal inhibitory concentration (IC_{50}) were determined from dose-response curves. Different light doses were tested in this study and the results are showed in Table 4.2 and Figure 4.9.

The effect observed for **1** was higher than LFX, and **2** (a 3-fold increase of the IC_{50} was determined) while in the case of ACLFX, its phototoxicity is very low. Different behaviors must be involved in the phototoxic assays. Noteworthy, the *N*-alkyl chain at the position **1** of these type of fluoroquinolones is a small structural modification with a great influence because the phototoxicity of **1** is the highest. However, the lowest phototoxic effect observed for ACLFX and the results obtained using **2** and LFX can not be easily explained because ACLFX is structurally more related to LFX than **2** with LFX and ACLFX and **2** have acidic properties, while LFX has an amphoteric character. Moreover, it has been observed that this type of fluoroquinolones showed similar cytoplasmic localization in human cells.[27,34] Nevertheless, the phototoxic effect observed in the FQs of this study could be understood combining the affinity of these compounds to biomolecules such as DNA and or proteins and the reactivity of their photo-generated intermediates with their target biomolecules. Hence, although the four FQs under study show the same intermediates, mainly singlet and triplet excited states and aryl cations and radicals, they showed different affinity to DNA and HSA and in the case of **1** and **2**, different location into the protein (see Scheme 4.1, Table 4.1 and Figure 4.2 respectively).

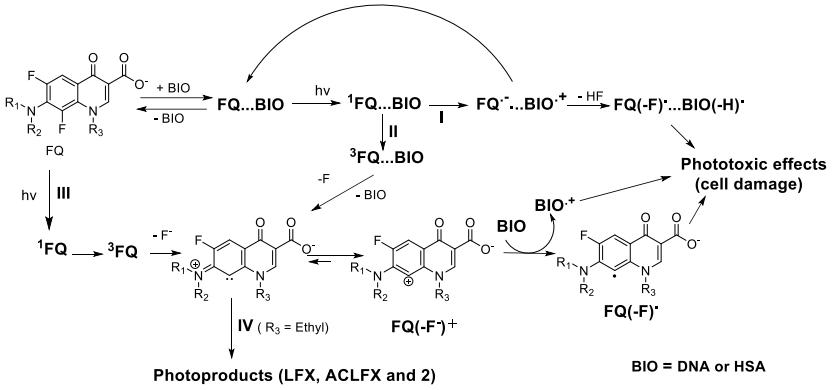

Scheme 4.1. Photochemical process involving the phototoxic effects observed for LFX, ACLFX, **1** and **2**.

Thus, the most phototoxic compound **1**, which has a high affinity for albumin, must react efficiently with proteins via its aryl cation because it does not react with albumin from its ^{1}**1** and cannot generate photoproducts by an intramolecular reaction described for the other dihalogenated FQs.[27] Thereby, although compound **2** has the same affinity than **1** to proteins such as HSA, its phototoxic effectivity can decrease because it can be photode gradated via pathway IV. In the case of ACLFX, which shows the lowest phototoxicity but has the same affinity to HSA than that detected for **2** and also a similar photodegradation pathway, a back electron transfer process of the reaction of its singlet excited state with any reactive amino acid of HSA could explain the results obtained. In fact, ACLFX showed different location in albumin, and consequently, the involvement of route I in its photochemical processes. The phototoxicity observed for LFX could be mainly produced from pathway I with DNA because LFX has best affinity

to DNA and it is known that the back electron transfer process in these biomolecules is a minor pathway.[22]

4.3. Conclusion

To understand the phototoxic effects produced by FQs it is necessary to evaluate their reactivity with biomolecules as well as their affinities. Thereby, as it has been done for the antibacterial activity of FQs, a deep study about the structure-activity of the phototoxic properties of FQs would be needed to enhance the phototoxic potential of FQ in order to obtain drugs with more photochemotherapeutic properties.

4.4. Experimental section

4.4.1. Materials

Calf thymus DNA, Human serum albumin fatty free (HSA) and lomefloxacin (LFX) were commercial products obtained from Sigma-Aldrich while plasmid prB322 was supplied by Roche and Sephadex G-25 columns by GE Healthcare. Sodium phosphate buffer (PB) was prepared from reagent-grade products using milli-Q water; the pH of the solutions was measured through a glass electrode and adjusted with NaOH to pH 7.4.

4.4.2. Synthesis of FQs

Acetyl LFX (*7-(4-acetyl-3-methyl-1-piperazinyl)-1-ethyl-6,8-difluoro-1,4-dihydro-4-oxoquinoline-3-carboxylic acid*, (**ALFX**), was prepared as

previously described from a solution of LFX (300 mg, 0.9 mmol) in acetic anhydride (50 mL) that was refluxed for 7 h.[23]

1-Methyl-7-dimethy1amino-6,8-difluoro-1,4-dihydro-3-quinolinecarboxylic acid (**1**) and *1-Ethyl-7-dimethy1amino-6,8-difluoro-1,4-dihydro-3-quinolinecarboxylic acid* (**2**) were prepared as previously described.[35,36]

4.4.3. Absorption and emission measurements

Ultraviolet spectra were recorded on a UV/Vis scanning spectrophotometer (Cary 50). Fluorescence emission spectra were recorded on a Photon Technology International (PTI) LPS-220B fluorimeter. Lifetimes were measured with a time resolved spectrometer (TimeMaster fluorescence lifetime spectrometer TM-2/2003) from PTI by means of the stroboscopic technique, which is a variation of the boxcar technique. A hydrogen/nitrogen flashlamp (1.8 ns pulse width) was used as excitation source. The kinetic traces were fitted with monoexponential decay functions. Measurements were made under aerated conditions at room temperature (25 °C) in cuvettes of 1 cm path length. The excitation wavelength used to register the fluorescence lifetimes was 320 nm. The fluorescence quantum yield of quinine bisulphate in 1 N H_2SO_4 (ϕ_F = 0.546) was used as a standard.

4.4.4. Fluoroquinolone fluorescence quenching by DNA

The experiments were performed using 10^{-4} M FQ buffered aqueous solutions (10^{-3} M PB, pH *ca*. 7.4) at excitation wavelength of 355 nm

(there is an isosbestic wavelength). The DNA concentrations were determined spectrophotometrically taking into account a molar extinction coefficient ε=258 nm = 6700 cm^{-1} M^{-1}.[37,38] Equation 4.2 was selected to determine the drug-DNA interactions from fluorescence quenching data:[31,32,39–41]

$$F_0/F = 1 + K_{sv}[Q] \quad \text{Eq. 4.2}$$

where F_0 and F are the fluorescence intensities in the absence and presence of the quencher respectively, [Q] is the quencher concentration (DNA from 10^{-5} to 1.5 x 10^{-3} M in nucleotide) and K_{sv} is the Stern-Volmer quenching constant.

4.4.5. Fluorescence quenching of fluoroquinolones by albumin

This fluorescence quenching study was performed by adding HSA concentrations from 10^{-5} to 10^{-4} M FQ buffered aqueous solutions (10^{-3} M PB, pH *ca*. 7.4) after excitation at 310 nm (there is an isosbestic wavelength). These data were also analyzed using the equation 4.2 to establish the drug-biomolecule interactions.

Equation 4.2 was selected to determine the drug-protein interactions from the fluorescence quenching data:[42–46]

4.4.6. Albumin fluorescence quenching by fluoroquinolones

Experiments were performed with phosphate buffered (10^{-3}M, pH *ca* 7.4) aqueous solutions containing 10^{-5} M HSA. Thus, HSA displays a fluorescence band centered at 344 nm, after excitation at 295 nm. The fluorescence quenching of this band was monitored after addition of

increasing the amounts of FQs under study (from 10^{-6} to 1.2 x 10^{-5} M). Before analyzing the data, the so-called inner filter effect correction (IFE) was applied because both FQ absorb light at the excitation and emission wavelengths. The IFE correction was applied using equation 4.3:[42,47,48]

$$F_{corr} = F_{obs} \times 10^{(Aex+Aem)/2} \quad \text{Eq. 4.3}$$

where F_{corr} and F_{obs} are the corrected and observed fluorescence intensities respectively, and A_{ex} and A_{em} are the absorbance values at the excitation and emission wavelengths, respectively.

4.4.7. Laser flash photolysis experiments

A pulsed Nd:YAG laser system was used for the excitation at 355 nm. The single pulses were ~10 ns duration and the energy was from 15 to 5 mJ/pulse. A pulsed xenon lamp was employed as detecting light source. The laser flash photolysis apparatus consisted of the pulsed laser, the Xe lamp, a monochromator and a photomultiplier made up of a tube, housing and power supply. The output signal from the oscilloscope was transferred to a personal computer.

Aqueous solutions of 10^{-4} M FQs were prepared in 10^{-3} M PB and the experiments were registered under anaerobic conditions by bubbling N_2O. Transient absorption spectra at different times after the laser pulse were obtained for each sample in the presence and the absence of biomolecules, paying special attention to intersystem crossing quantum yield changes and to the generation of new intermediates.

The DNA concentrations ranged between 10^{-4} and 10^{-3} M in nucleotides and HSA concentration from 10^{-5} to 10^{-4} M.

The quenching experiments were carried out keeping the pH constant at 7.4 throughout the experiment.

Rate constants of aryl cations quenching by biomolecules were determined using the Stern-Volmer equation 4.4:

$$1/\tau = 1/\tau_0 + k\,[\text{Quencher}] \qquad \text{Eq 4.4}$$

4.4.8. Analysis of the covalent binding of fluoroquinolones to HSA induced by light

The study was performed using 1/1 molar ratio of drug/protein for UV-Vis measurements. FQs were added to 10-^{4} M HSA and allowed to incubate in the dark for 30 minutes. Photolysis was performed using a Rayonet photochemical reactor equipped with six black light phosphor lamps emitting in the 310-390 nm range, with a maximum at *ca*. 350 nm. Samples were then irradiated during 120 seconds UV time periods (with a light doses of *ca*. 280 mJ/cm^2) and then kept in the darkness during 24 hours prior to analysis (controls included drug-HSA mixtures kept in the dark, HSA with and without irradiation and irradiated drug added to HSA). The samples were diluted by a factor of two by adding water before the protein separation. Subsequently, to determine whether FQ is covalently linked to HSA, the solutions were chromatographed on Sephadex G-25 columns equilibrated with 2/8 ethanol/aqueous 10 mM PB, as described previously.[41] The first fraction of each sample contained albumin (alone or covalently linked to a drug)

while in the second one there was the remaining free drug. Thus, the first fraction was analyzed by UV-Vis spectrometry to determine the amount of drug linked to albumin from the absorption spectra of these samples.

4.4.9. *In Vitro* 3T3 neutral red uptake (NRU) phototoxicity test

BALB/c 3T3 fibroblasts cell line was grown in Dulbecco's Modified Eagle Medium (DMEM) supplemented with 4 mM glutamine, 1% penicillin/streptomycin 10% and Fetal Bovine Serum (FBS) and routinely maintained in exponential growth in 75 cm^2 plastic flasks in a humidified incubator at 37°C under 5% carbon dioxide atmosphere. The 3T3 Neutral Red Uptake Phototoxicity Test was performed as described by the OECD guideline 432 (OECD, 2004) with minor modifications.[49,50] Briefly, two 96-wells plates (2.5×10^4 cells/well) were seeded for each compound. Cells were treated with compounds FQs and SDS at several concentrations ranging from 0.5 µM to 500 µM and incubated for 1 h. Afterwards, one plate was irradiated on ice for 11 min to achieve a dose of UVA equivalent to 5 J/cm2 (UVA LIGHT), whereas the other plate was kept in a dark box (DARK). The viability of UVA-treated control cells in the absence of test compounds was > 90% of those kept in the dark indicating the suitability of the UV dose. After irradiation, the compound solutions were replaced with DMEM medium, and plates were incubated overnight. Subsequently, neutral red solution (50 µg/mL) was added into each well and incubated for 2 h. Cells were washed with PBS and neutral red was extracted in 100 µL with the desorbs solution (water 49% (v/v), ethanol 50% (v/v) and acetic acid 1%

(v/v). Then, the absorbance was measured at 550 nm on a Multiskan Ex microplate reader. For each compound dose-response curves were established in order to determine the concentration of compound producing a 50% reduction of the neutral red uptake (IC_{50}) in the dark and light. In the end, Photo-Irritation-Factor (PIF) was determined using the following equation:

$$PIF = IC_{50}\ DARK / IC_{50}\ UVA\ LIGHT \qquad \text{Eq. 4.4}$$

According to the OECD Test Guideline (OECD, 2004)[50] a chemical is predicted as phototoxic if PIF is > 5, probably phototoxic if PIF > 2 and < 5, and non-phototoxic when PIF < 2. Sodium dodecyl sulphate (SDS) was used as negative control and lomefloxacin (LFX) was used as an established phototoxic reference compound.[17,51]

4.5. References

1. Domagala JM, Hanna LD, Heifetz CL, et al. New Structure-Activity Relationships of the Quinolone Antibacterials Using the Target Enzyme. The Development and Application of a DNA Gyrase Assay. *J Med Chem*. 1986;29(3):394-404.
2. Chu DTW, Fernandes PB. Structure-activity relationships of the fluoroquinolones. *Antimicrob Agents Chemother*. 1989;33(2):131-135.
3. de Guidi G, Bracchitta G, Catalfo A. Photosensitization Reactions of Fluoroquinolones and Their Biological Consequences. *Photochem Photobiol*. 2011;87(6):1214-1229.
4. Kang D-H, Kim J-S, Jung M-J, et al. New insight for fluoroquinophenoxazine derivatives as possibly new potent topoisomerase I inhibitor. *Bioorg Med Chem Lett*. 2008;18(4):1520-1524.

5. Azéma J, Guidetti B, Dewelle J, et al. 7-((4-Substituted)piperazin-1-yl) derivatives of ciprofloxacin: Synthesis and in vitro biological evaluation as potential antitumor agents. *Bioorganic Med Chem*. 2009;17(15):5396-5407.
6. Cullen M, Baijal S. Prevention of febrile neutropenia: Use of prophylactic antibiotics. *Br J Cancer*. 2009;101:S11-S14.
7. Kim K, Pollard JM, Norris AJ, et al. High-throughput screening identifies two classes of antibiotics as radioprotectors: Tetracyclines and fluoroquinolones. *Clin Cancer Res*. 2009;15(23):7238-7245.
8. Al-Trawneh SA, Zahra JA, Kamal MR, et al. Synthesis and biological evaluation of tetracyclic fluoroquinolones as antibacterial and anticancer agents. *Bioorganic Med Chem*. 2010;18(16):5873-5884.
9. Paul M, Gafter-Gvili A, Fraser A, Leibovici L. The anti-cancer effects of quinolone antibiotics? *Eur J Clin Microbiol Infect Dis*. 2007;26(11):825-831.
10. Perrone CE, Takahashi KC, Williams GM. Inhibition of human topoisomerase IIalpha by fluoroquinolones and ultraviolet A irradiation. *Toxicol Sci*. 2002;69(1):16-22.
11. Lhiaubet-Vallet V, Bosca F, Miranda MA. Photosensitized DNA Damage: The Case of Fluoroquinolones. *Photochem Photobiol*. 2009;85(4):861-868.
12. Marrot L, Belaïdi JP, Jones C, et al. Molecular responses to photogenotoxic stress induced by the antibiotic lomefloxacin in human skin cells: From DNA damage to apoptosis. *J Invest Dermatol*. 2003;121(3):596-606.
13. JR M, A S, L M. Photogenotoxicity of mammalian cells: a review of the different assays for in vitro testing. *Photochem Photobiol*. 2002;75(5):437-447.
14. Martinez LJ, Li G, Chignell CF. Photogeneration of fluoride by the fluoroquinolone antimicrobial agents lomefloxacin and fleroxacin. *Photochem Photobiol*. 1997;65(3):599-602.

15. Chignell CF, Haseman JK, Sik RH, Tennant RW, Trempus CS. Photocarcinogenesis in the Tg.AC mouse: lomefloxacin and 8-methoxypsoralen. *Photochem Photobiol*. 2003;77(1):77-80.
16. Fasani E, Profumo A, Albini A. Structure and Medium-Dependent Photodecomposition of Fluoroquinolone Antibiotics. *Photochem Photobiol*. 1998;68(5):666-674.
17. Jeffrey AM, Shao L, Brendler-Schwaab SY, Schlüter G, Williams GM. Photochemical mutagenicity of phototoxic and photochemically carcinogenic fluoroquinolones in comparison with the photostable moxifloxacin. *Arch Toxicol*. 2000;74(9):555-559.
18. HAYASHI N. New Findings on the Structure-Phototoxicity Relationship and Photostability of Fluoroquinolones. *YAKUGAKU ZASSHI*. 2005;125(3):255-261.
19. Hayashi N, Nakata Y, Yazaki A. New Findings on the Structure-Phototoxicity Relationship and Photostability of Fluoroquinolones with Various Substituents at Position 1. *Antimicrob Agents Chemother*. 2004;48(3):799-803.
20. Fasani E, Manet I, Capobianco ML, Monti S, Pretali L, Albini A. Fluoroquinolones as potential photochemotherapeutic agents: Covalent addition to guanosine monophosphate. *Org Biomol Chem*. 2010;8(16):3621-3623.
21. Soldevila S, Cuquerella MC, Bosca F. Understanding of the photoallergic properties of fluoroquinolones: Photoreactivity of lomefloxacin with amino acids and albumin. *Chem Res Toxicol*. 2014;27(4):514-523.
22. Soldevila S, Consuelo Cuquerella M, Lhiaubet-Vallet V, Edge R, Bosca F. Seeking the mechanism responsible for fluoroquinolone photomutagenicity: A pulse radiolysis, steady-state, and laser flash photolysis study. *Free Radic Biol Med*. 2014;67:417-425.
23. Albini A, Monti S. Photophysics and photochemistry of fluoroquinolones. *Chem Soc Rev*. 2003;32(4):238-250.

24. Soldevila S, Bosca F. Photoreactivity of fluoroquinolones: Nature of aryl cations generated in water. *Org Lett*. 2012;14(15):3940-3943.
25. Cuquerella MC, Miranda MA, Boscá F. Generation of detectable singlet aryl cations by photodehalogenation of fluoroquinolones. *J Phys Chem B*. 2006;110(13):6441-6443.
26. Freccero M, Fasani E, Mella M, Manet I, Monti S, Albini A. Modeling the Photochemistry of the Reference Phototoxic Drug Lomefloxacin by Steady-State and Time-Resolved Experiments, and DFT and Post-HF Calculations. *Chem - A Eur J*. 2008;14(2):653-663.
27. Anaya-Gonzalez C, Soldevila S, Garcia-Lainez G, Bosca F, Andreu I. Chemical tuning for potential antitumor fluoroquinolones. *Free Radic Biol Med*. 2019;141:150-158.
28. Soldevila S, Cuquerella MC, Bosca F. Understanding of the photoallergic properties of fluoroquinolones: Photoreactivity of lomefloxacin with amino acids and albumin. *Chem Res Toxicol*. 2014;27(4):514-523.
29. Sun H, He P. Characterization of interactions between fluoroquinolones and human serum albumin by CE-frontal analysis. *Chromatographia*. 2008;68(11-12):969-975.
30. Epps DE, Raub TJ, Kézdy FJ. A general, wide-range spectrofluorometric method for measuring the site-specific affinities of drugs toward human serum albumin. *Anal Biochem*. 1995;227(2):342-350.
31. Alarcón E, Edwards AM, Aspee A, et al. Photophysics and photochemistry of dyes bound to human serum albumin are determined by the dye localization. *Photochem Photobiol Sci*. 2010;9(1):93-102.
32. Ahmad B, Parveen S, Khan RH. Effect of albumin conformation on the binding of ciprofloxacin to human serum albumin: A novel approach directly assigning binding site. *Biomacromolecules*. 2006;7(4):1350-1356.

33. Monti S, Manet I, Manoli F, Capobianco ML, Marconi G. Gaining an insight into the photoreactivity of a drug in a protein environment: A case study on nalidixic acid and serum albumin. *J Phys Chem B*. 2008;112(18):5742-5754.
34. Perucca P, Savio M, Cazzalini O, et al. Structure-activity relationship and role of oxygen in the potential antitumour activity of fluoroquinolones in human epithelial cancer cells. *J Photochem Photobiol B Biol*. 2014;140:57-68.
35. Domagala JM, Heifetz CL, Hutt MP, et al. 1-Substituted 7-[3-[(Ethylamino)methyl]-1-pyrrolidinyl]-6,8-difluoro-1,4-dihydro-4-oxo-3-quinolinecarboxylic Acids. New Quantitative Structure-Activity Relationships at N1 for the Quinolone Antibacterials. *J Med Chem*. 1988;31(5):991-1001.
36. Sarma MR, Kumar V, Prasad ASR, et al. *Synthesis and Biological Activity of Novel Antibacterial Quinolones T*. Vol 40.; 2001.
37. Sortino S, Condorelli G. Complexes between fluoroquinolones and calf thymus DNA: Binding mode and photochemical reactivity. *New J Chem*. 2002;26(2):250-258.
38. Son GS, Yeo JA, Kim MS, et al. Binding mode of norfloxacin to calf thymus DNA. *J Am Chem Soc*. 1998;120(26):6451-6457.
39. Chi Z, Liu R, Zhang H. Noncovalent interaction of oxytetracycline with the enzyme trypsin. *Biomacromolecules*. 2010;11(9):2454-2459.
40. Catalfo A, Calandra ML, Renis M, Serrentino ME, De Guidi G. Rufloxacin-induced photosensitization in yeast. *Photochem Photobiol Sci*. 2007;6(2):181
41. Alarcón E, Edwards AM, Aspée A, Borsarelli CD, Lissi EA. Photophysics and photochemistry of rose bengal bound to human serum albumin. *Photochem Photobiol Sci*. 2009;8(7):933-943.
42. Fasani E, Barberis Negra FF, Mella M, Monti S, Albini A. Photoinduced C-F bond cleavage in some fluorinated 7-amino-4-quinolone- 3-carboxylic acids. *J Org Chem*. 1999;64(15):5388-

5395.

43. Sauvaigo S, Douki T, Odin F, Caillat S, Ravanat J-L, Cadet J. Analysis of Fluoroquinolone-mediated Photosensitization of 2′-Deoxyguanosine, Calf Thymus and Cellular DNA: Determination of Type-I, Type-II and Triplet-Triplet Energy Transfer Mechanism Contribution¶. *Photochem Photobiol*. 2007;73(3):230-237.
44. Martínez L, Chignell CF. Photocleavage of DNA by the fluoroquinolone antibacterials. *J Photochem Photobiol B Biol*. 1998;45(1):51-59.
45. Liu CS, Hernandez R, Schuster GB. Mechanism for Radical Cation Transport in Duplex DNA Oligonucleotides. *J Am Chem Soc*. 2004;126(9):2877-2884.
46. Scaiano JC, Stewart LC. Phenyl Radical Kinetics. *J Am Chem Soc*. 1983;105(11):3609-3614. doi:10.1021/ja00349a043
47. Zhang P, Song X, Li H, Yao S, Wang W. Transient species of several fluoroquinolones and their reactions with amino acids. *J Photochem Photobiol A Chem*. 2010;215(2-3):191-195.
48. Cuquerella MC, Miranda MA, Bosca F. Role of excited state intramolecular charge transfer in the photophysical properties of norfloxacin and its derivatives. *J Phys Chem A*. 2006;110(8):2607-2612.
49. Garcia-Lainez G, Martínez-Reig AM, Limones-Herrero D, Consuelo Jiménez M, Miranda MA, Andreu I. Photo(geno)toxicity changes associated with hydroxylation of the aromatic chromophores during diclofenac metabolism. *Toxicol Appl Pharmacol*. 2018;341:51-55.
50. Palumbo F, Garcia-Lainez G, Limones-Herrero D, et al. Enhanced photo(geno)toxicity of demethylated chlorpromazine metabolites. *Toxicol Appl Pharmacol*. 2016;313:131-137.
51. Spratt TE, Schultz SS, Levy DE, Chen D, Schlüter G, Williams GM. Different mechanisms for the photoinduced production of oxidative dna damage by fluoroquinolones differing in photostability. *Chem Res Toxicol*. 1999;12(9):809-815.

Chapter 5. Studies of fluoroquinolone derivatives as alkylating bombs

5.1. Introduction

Fluoroquinolones (FQs) were first discovered in 1980[1] and used as antimicrobial agents due to their pharmacological activity based on the inhibition of topoisomerase II, an enzyme which plays a key role in the replication and repair of bacterial DNA.[2] In the last years, some of the components of this family of quinolones have gained interest as antitumoral drugs acting in the replication of DNA by inhibiting DNA polymerase, topoisomerase I and topoisomerase II.[3–6] Several studies demonstrate that this genotoxic effect is enhanced by ultraviolet (UV) irradiation converting the FQs in proper photochemotherapeutic agents.[7] Photochemical and photophysical properties of 6,8-dihalogenated FQ have been deeply studied in the presence and absence of biomolecules. Unusual heterolysis of C_8-halogen bond generates an aryl cation with alkylating properties, which has been proposed as the origin of the most important FQ side-effects.[8–12] Several studies have associated the formation of reactive intermediates in the photodehalogenation process with the FQ photosensitivity.[8–14] Interestingly, decreasing the peripheral substituents size has recently been shown to improve the efficiency of intermolecular reactions between biomolecules and FQs due to the lack of intramolecular reactivity of a carbene intermediate with their substituents.[15] Thereby, when the phototoxic properties of lomefloxacin (LFX) were compared with **1** and **2** in vitro 3T3 NRU phototoxicity test (see structures in Chart 4.1), the Photo-Irritation-Factor (PIF) of **1** resulted to be more than three times higher than **2** or the phototoxic LFX. Hence, it has been

demonstrated that the photochemotherapeutic properties of antitumor quinolones could be improved by using this structural modification.[15] It has also been evidenced that the intermediate responsible for the phototoxic properties associated with dihalogenated quinolones is the aryl cation.

Nanomedicine has emerged as a new branch to solve the shortcomings of current treatments by designing new materials.[16] An extensive range of nanomaterials has been developed during the last decades as therapeutics either for cancer or other diseases.[16–18] An example of those new materials are the upconversion nanoparticles (UCNP) which have the capability of converting near infrared light (NIR) into UV, Visible (Vis) or NIR emission in an anti-Stokes process.[19] They have gained interest over the past years due to their advantages such as high signal/noise ratio, low toxicity and higher penetration in tissue of NIR light for several applications like bioimaging, drug release, laser design or solar cells among others. [20–26] In this context, several UCNP materials have also been deeply studied for photodynamic therapy (PDT), which uses a combination of special drugs and UV light to treat cancerous. Thus, cancer cells death have been observed by using UCNP cores with shells containing different types of photosensitizers. Thereby, by applying NIR to this type of nanomaterials an activated oxygen specie (singlet oxygen) is generated, which is able to oxidize biomolecules of the cells. [27–31]

With this background, the to design of a new nanomaterial for phototherapy by using the capability of UCNP to transform NIR in UV-

Vis-NIR light and the alkylating properties of some type of fluoroquinolones was proposed. Thereby, the new nanohybrids will attack the cells as alkylating bombs.

The design of the new material will be composed of UCNP ($NaYF_4$: Yb/Tm (20%, 0.5%)@$NaYF_4$) as core and the most phototoxic FQ (compound **1**) as shell together with succinic acid (SA).

5.2. Results and discussion

5.2.1. Synthesis and characterization of upconversion nanoparticles (UCNP)

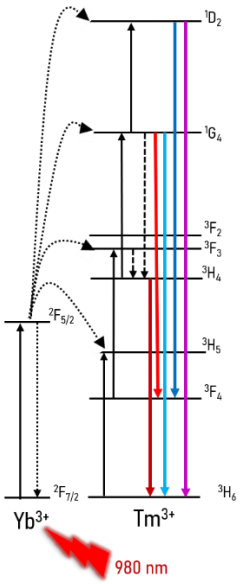

Scheme 5.1. ETU mechanism in a matrix doped with Yb/Tm.

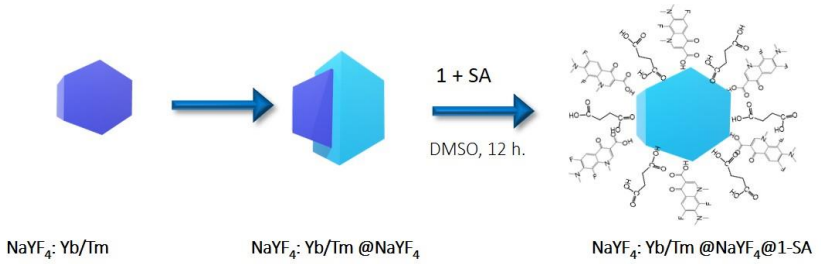

Scheme 5.2. Synthetic route to obtain $NaYF_4$: Yb/Tm@$NaYF_4$@**1**-SA

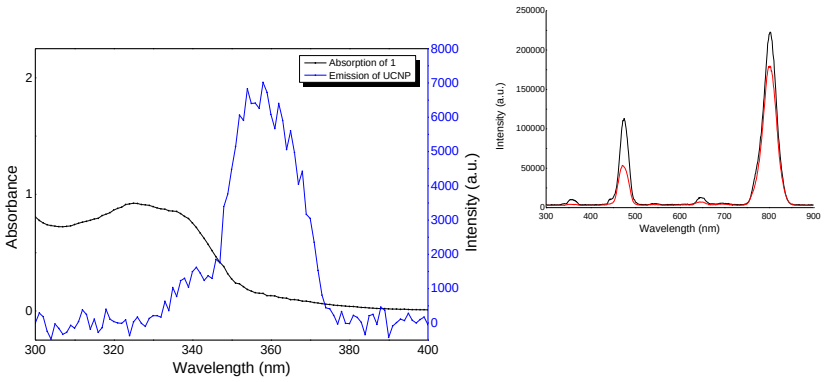

Figure 5.1. Absorption spectrum of **1** and emission spectrum of $NaYF_4$: Yb/Tm (20%, 0.5%)@$NaYF_4$ 2mg / mL at desired region. Inset: complete emission spectrum of $NaYF_4$: Yb/Tm (20%, 0.5%)@$NaYF_4$ (black) and $NaYF_4$: Yb/Tm (20%, 0.5%) (red). λ_{ex} = 980 nm

$NaYF_4$: Yb/Tm 20%, 0,5%) nanoparticles were selected as the base of the nanosystem due to their particular characteristics. On one hand, they are able to absorb in the NIR region (~ 980 nm) and emit at shorter wavelengths avoiding direct irradiation with harmful UV light. On the other hand, due to their specific composition, with Thulium and Yttrium as dopants, they have an emission peak *ca.* 362 nm being a good candidate to excite our studied drug **1** (see Figure 5.1).[19,32]

$NaYF_4$: Yb/Tm (20%, 0,5%) nanoparticles need more than two photons due to their high space between energetic levels. For that reason, $NaYF_4$: Yb/Tm (20%, 0,5%) @$NaYF_4$ core/shell nanoparticles have been synthesize achieving higher emission in the region of interest (see inset of Figure 5.1)[33–35]

First of all, upconversion nanoparticles were synthesized via Ostwald Ripening method (more details in experimental section). As second step, a shell made of $NaYF_4$ was grown in order to protect the $NaYF_4$: Yb/Tm core from the future hydrophilic media and, in addition, to achieve higher emission bands. This nanosystem was going to be studied *in vitro*, so nanoparticles need to have a hydrophilic shell which make them water soluble. Different types of hydrophilic shells have been described in the literature.[33,35–37] In this case, the nanosystem has been covered with succinic acid by ligand exchange (see Scheme 5.1). This type of reaction allows in one-step cover change and drug loading.

After each step of the synthetic route (Scheme 5.2), nanoparticles were characterized by X-ray diffraction system and transmission electron microscopy (see Figure 5.2 and 5.3). β- $NaYF_4$ crystal can be observed in Figure 5.3 X-Ray as compared with the refence. The obtained core/shell nanoparticles have a size of 21 ± 2 nm. $NaYF_4$: Yb/Tm (20%, 0.5%) nanoparticles were less regular in size (17 ± 2.5 nm) and shape.

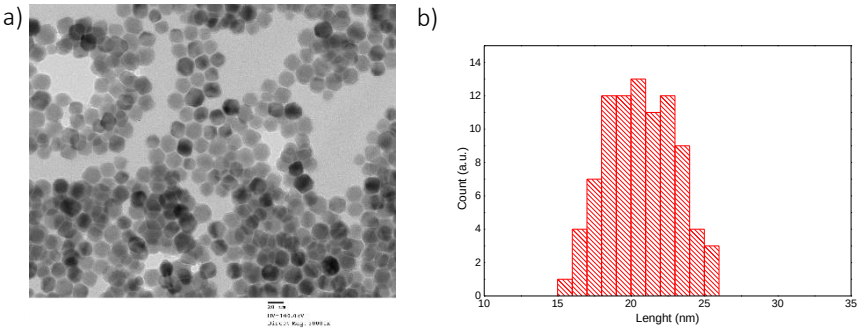

Figure 5.2. a) TEM image of $NaYF_4$: Yb/Tm (20%, 0,5%) @$NaYF_4$ b) Histogram of distribution size

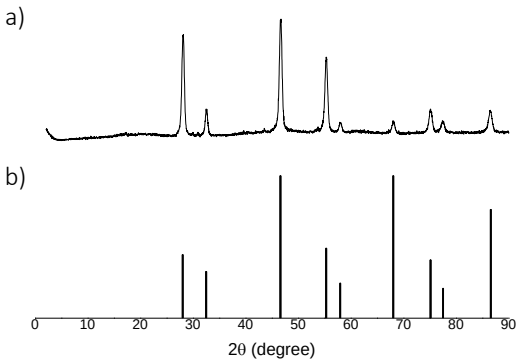

Figure 5.3. a) X-ray spectrum of $NaYF_4$: Yb/Tm (20%, 0,5%) @$NaYF_4$ b) Standard reference from $NaYF_4$ crystal (JCPDS No. 77-2042).

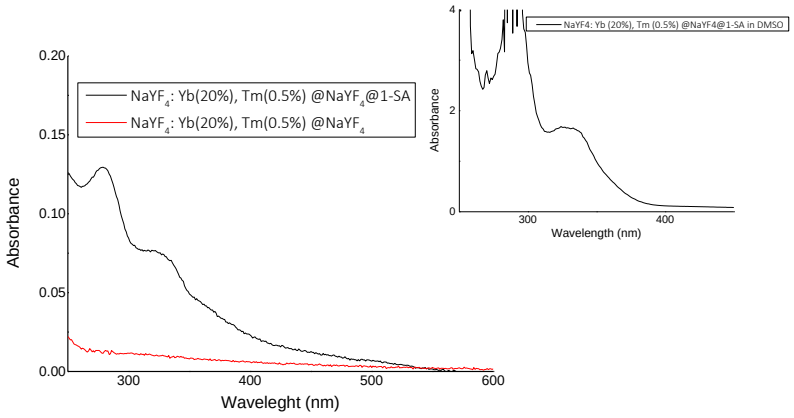

Figure 5.4. Absorption spectrum of $NaYF_4$: Yb/Tm (20%, 0.5%) @$NaYF_4$ 2 mg/ mL in cyclohexane and $NaYF_4$: Yb/Tm (20%, 0.5%) @$NaYF_4$ @**1**-SA 2mg / mL in cell media. Inset: $NaYF_4$: Yb/Tm (20%, 0.5%) @$NaYF_4$ @1-SA 2 mg / mL in DMSO

The ligand exchange of oleic acid (OA) by SA and **1** was performed using different proportions between SA and **1** (see experimental section below). High amount of **1** resulted in high **1** concentration loaded in the system but low hydrophilic nanoparticles (see inset of Figure 5.4). After several trials with different SA-**1** proportions, the selected ones were the specified in experimental section and Figure 5.4. There was high light scattering in the samples resulting in an increase of the base line from 550 nm, which was subtracted for determining **1** concentration in the solutions of nanoparticles. An approximation of the number of molecules of **1** contained in a nanoparticle was determined using the area of **1** and the surface of a

sphere of 20 nm of diameter and between 10-15 molecules of **1** are on the surface of a nanoparticle.

Concerning the stability of the nanoparticles under study, it was observed that their stability in aqueous media was low. Hence, it was observed that the nanoparticles were completely dissolved in aqueous media in two weeks. In fact, our nanosystem showed small deformations or cracks only 48 h after the complete preparation (see in Figure 5.5 TEM images of $NaYF_4$: Yb/Tm (20%, 0.5%) @$NaYF_4$ @1-SA system after 48 h in aqueous media).

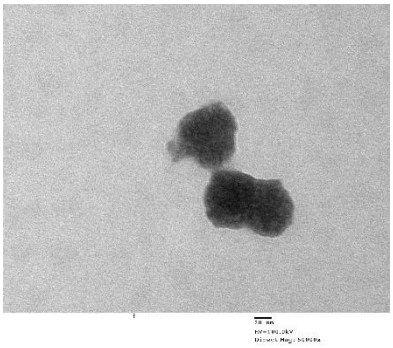

Figure 5.5. TEM image of $NaYF_4$: Yb/Tm (20%, 0.5%) @$NaYF_4$ @1-SA system after 48 h

5.2.2. Photolysis of 1 in aqueous solutions with nanosystem $NaYF_4$:Yb(20%)Tm (0.5%) @$NaYF_4$@1-SA

As a way to detect the generation of the alkylating intermediates (aryl cations, see mechanism in Scheme 3.3), photolysis of **1** was analyzed by measuring fluoride anion release (details in experimental section 5.4). Thus, analysis of irradiations of

$NaYF_4$:Yb(20%)Tm(0.5%)@$NaYF_4$ @**1**-SA in aqueous medium (2.5 mL of nanoparticles 2mg/mL containing **1** 2 x 10^{-5} M) using an infrared laser RLTMDL-980 1-2000 mW (PSU-III-LED) at λ_{max} = 980 nm ± 5 nm and a laser energy of ca. 2000 mW/cm^2 showed that 1 x10^{-5} M of fluoride anion had been released after the first 5 min of the irradiation and this value increased till 1.5 x 10^{-5} M after 10 min. Thereby, it was proved that the irradiation of $NaYF_4$: Yb (20%), Tm (0.5%) @$NaYF_4$ @**1**-SA with a laser at 980 produces the photolysis of **1** with the consequent release of fluoride anion and the generation of its aryl cation (mechanism details shown in previous chapters).

5.2.3. Cell viability assay of $NaYF_4$: Yb/Tm@$NaYF_4$@1-SA

The nanosystem for the cell viability assays contained 2.5 µM **1** in 2 mg of nanoparticles/ mL. Hence, after drug loading and hydrophilic surface achievement, HELA cells were treated with $NaYF_4$: Yb/Tm@$NaYF_4$@**1**-SA. A 24-hour incubation was carried out to ensure the entry of the nanosystem into the cell.[38] After incubation time, cells were irradiated at different times and viability assay was carried out.

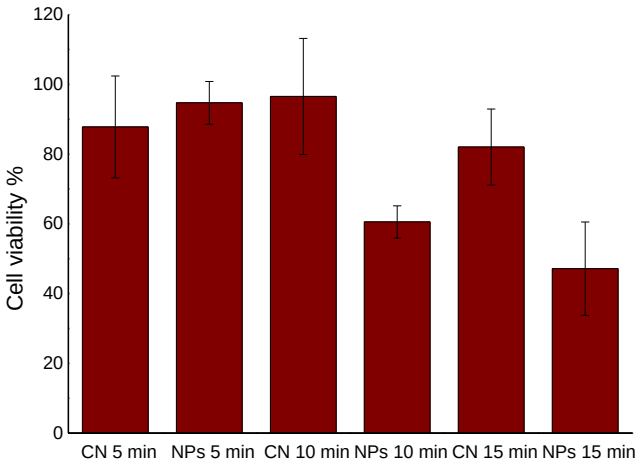

Figure 5.6. Cell viability of HELA cells after irradiation with $NaYF_4$: Yb/Tm@$NaYF_4$@**1**-SA (NPs) and without them (CN) at different irradiation times using a laser at 980 nm (5, 10 and 15 min).

These assays showed great results because the cell viability after 10 min of irradiation was only *ca*. 60 % and *ca*. 50 % after 15 min. Thus, the IC_{50} was achieved using only solutions of 2.5 µM, a value that is more than 6 times lower than that obtained using UVA irradiations of homogeneous solutions of compound **1** (IC_{50} *ca*. 16 µM (see page 70 in Chapter 3)). Hence, it was observed that the expected alkylating bombs increase the phototoxical properties of **1**.

5.3. Conclusions

The high phototoxic capacity observed for compound **1** was improved using nanosystems loaded with this molecule. The concept of an alkylating bomb to kill cells was probed using upconversion

nanoparticles and near infrared light. This increase of the described adverse effect of FQs could be used as a photochemotherapeutic property to destroy tumor cells.

5.4. Experimental section

5.4.1. Materials

Yttrium (III) chloride (YCl_3), Ytterbium (III) chloride ($YbCl_3$), Thulium (III) chloride ($TmCl_3$), oleic acid (OA), 1-octadecene (ODE), ammonium fluoride (NH_4F), sodium hydroxide (NaOH), and human serum albumin were commercial products obtained from Sigma-Aldrich Chemical Sodium phosphate buffer (PB) and sodium bicarbonate buffer were prepared from reagent-grade products using milli-Q water; the pH of the solutions was measured through a glass electrode and adjusted with NaOH to pH *ca*. 7.4. Dulbecco's Modified Eagle Medium (DMEM) was commercially obtained from Thermo Fisher. Other chemicals were of reagent grade and used as received.

5.4.2. Synthesis of 1-Methyl-7-dimethy1amino-6,8-difluoro-1,4-dihydro-3-quinolinecarboxylic acid (1)

1-Methyl-7-dimethy1amino-6,8-difluoro-1,4-dihydro-3-quinolinecarboxylic acid (**1**) was prepared as previously described.[15]

5.4.3. Instrumentation

UV-Vis absorption spectra were registered with a Varian Cary 50 spectrophotometer. For the characterization of $NaYF_4$: Yb/Tm (20%, 0.5%)@$NaYF_4$, Transmission electron microscopy JEOL JEM—1010, CUBIX XRD DY0822 X-ray radioactive system and Photon Technology

International (PTI) LPS-220B fluorimeter coupled with an infrared laser RLTMDL-980 1-2000 mW (PSU-III-LED) were used.

Fluoride detection was performed with a fluoride selective electrode (Crison 96 55 C)

5.4.4. Synthesis of $NaYF_4$: Yb/Tm (20%, 0.5%) [28]

The salts $YCl_3 \cdot H_2O$ (0.795 mmol), $YbCl_3 \cdot H_2O$ (0.2 mmol) and $TmCl_3 \cdot H_2O$ (0.005 mmol) were mixed with 12 mL of oleic acid (OA) and 30 mL of octadecene (ODE) in 100 mL 3-necked flask. The solution was heated to 160°C to form a homogeneous solution and then cooled down to room temperature under nitrogen flow. Afterwards, 10 mL methanol solution containing NH_4F (4 mmol) and NaOH (2.5 mmol) were added, and the solution stirred for 30 minutes. Vacuum-nitrogen cycles were done to help methanol evaporation. Then, the solution was heated to 310 °C, maintained at this temperature for 2 hours under N_2 atmosphere, and then cooled down to room temperature. The resultant nanocrystals were precipitated by the addition of ethanol, washed with ethanol three times, collected by centrifugation, and finally resuspended in cyclohexane.

5.4.5. Synthesis of $NaYF_4$: Yb/Tm (20%, 0.5%) @$NaYF_4$ [34]

A procedure similar to that shown above was used. $YCl_3 \cdot H_2O$ (1 mmol) was mixed with 12 mL of oleic acid (OA) and 30 mL of octadecene (ODE) in 100 mL 3-necked flask. The solution was heated to 160°C to form a homogeneous solution and then cooled down to 80°C under nitrogen flow. When the solution reaches 80°C a solution of

cyclohexane with $NaYF_4$: Yb/Tm nanoparticles was slowly added. Temperature was maintained until complete evaporation of cyclohexane. After room temperature achievement, 10 mL methanol solution containing NH_4F (4 mmol) and NaOH (2.5 mmol) were added, and the solution stirred for 30 minutes. Vacuum-nitrogen cycles were done to help methanol evaporation. Then, the solution was heated to 310°C, maintained at this temperature for 2 hours under N_2 atmosphere, and then cooled down to room temperature. The resultant nanocrystals were precipitated by the addition of ethanol, washed with ethanol three times, collected by centrifugation, and finally resuspended in cyclohexane.

5.4.6. Synthesis of $NaYF_4$: Yb/Tm (20%, 0.5%) @$NaYF_4$ @1-SA [39]

Studies of the photolysis of **1** in the $NaYF_4$: Yb/Tm(20%, 0.5%) @$NaYF_4$ @1-SA nanosystem were carried out adding $NaYF_4$: Yb/Tm (20%, 0,5%) @$NaYF_4$ nanocrystals (20 mg) to 2 mL DMSO solution containing 30 mg of succinic acid (SA) and 40 mg of **1**. Then, the mixture was maintained with magnetic stirring overnigth at room temperature to obtain the hydrophilic nanosystem. Afterwards, these nanosystems were separated by centrifugation, washed 3 times with DMSO and finally dispersed in 10 mL water and analyzed by UV-Vis spectroscopy.

In the cell assays, for a better aqueous solubility of the $NaYF_4$:Yb/Tm(20%, 0.5%) @$NaYF_4$ @1-SA nanosystem, the proportions between SA and **1** were modified. Thus, 40 mg **1** and 40 mg SA were used in this case. Afterwards, the nanosystems were separated by

centrifugation, washed 3 times with DMSO and finally dispersed in 10 mL DMEM cell media and analyzed by UV-Vis spectroscopy.

5.4.7. Irradiation of nanosystem $NaYF_4$: Yb /Tm (20%, 0.5%) @$NaYF_4$@1-SA

$NaYF_4$: Yb /Tm (20%, 0.5%) @$NaYF_4$@**1**-SA was irradiated with an infrared laser RLTMDL-980 1-2000 mW (PSU-III-LED) at λ_{max} = 980 nm ± 5 nm using an energy of 2000 mW/cm^2. Fluoride anion release was measured with a fluoride selective electrode (Crison 96 55 C). Hence, 2.5 mL of nanoparticles 2 mg/mL in cell media containing **1** 2 x 10^{-5} M were placed in a watch glass and irradiated with the laser at λ_{max} = 980 nm during 5 and 10 min. Then, each sample was analyzed with the fluoride selective electrode (Crison 96 55 C). Dark controls were also performed.

5.4.8. In Vitro HELA phototoxicity test

HELA cell line was grown in Dublecco's Modified Eagle Medium (DMEM) supplemented with 4 mM glutamine, 1% penicillin/streptomycin 10% and Fetal Bovine Serum (FBS) and routinely maintained in exponential growth in 75 cm^2 plastic flasks in a humidified incubator at 37°C under 5% carbon dioxide atmosphere.

For the phototoxicity test, two 96-wells plates (2.5 × 10^4 cells/well) were seeded. Cells were treated with $NaYF_4$: Yb /Tm (20%, 0.5%) @$NaYF_4$@**1**-SA at 2.5 µM concentration and incubated for 24 h. Afterwards, one plate was irradiated on ice for 5, 10 and 15 min with an infrared laser RLTMDL-980 1-2000 mW (PSU-III-LED) at λ_{max} = 980

nm ± 5 nm using 2000 mW laser power, whereas the other plate was kept in a dark box (DARK). The viability of NIR-treated control cells in the absence of test compounds was > 90% of those kept in the dark indicating the suitability of the NIR dose. After irradiation, the compound solutions were replaced with DMEM medium, and plates were incubated overnight. Subsequently, MTT (50 µg/mL) was added into each well and incubated for 2 h. Cells were washed with PBS and MTT was extracted in 100 µL with the desorbs solution (water 49% (v/v), ethanol 50% (v/v) and acetic acid 1% (v/v). Then, the absorbance was measured at 550 nm on a Multiskan Ex microplate reader.

5.5. References

1. Al-Trawneh, S. A. *et al.* Synthesis and biological evaluation of tetracyclic fluoroquinolones as antibacterial and anticancer agents. *Bioorganic Med. Chem.* **18**, 5873–5884 (2010).
2. Domagala, J. M. *et al.* New Structure-Activity Relationships of the Quinolone Antibacterials Using the Target Enzyme. The Development and Application of a DNA Gyrase Assay. *J. Med. Chem.* **29**, 394–404 (1986).
3. Chu, D. T. W. *et al.* Synthesis and antitumour activities of quinolone antineoplastic agents. *Drugs Exp. Clin. Res.* **18**, 275–282 (1992).
4. Kang, D.-H. *et al.* New insight for fluoroquinophenoxazine derivatives as possibly new potent topoisomerase I inhibitor. *Bioorg. Med. Chem. Lett.* **18**, 1520–1524 (2008).
5. Azéma, J. *et al.* 7-((4-Substituted)piperazin-1-yl) derivatives of ciprofloxacin: Synthesis and in vitro biological evaluation as potential antitumor agents. *Bioorganic Med. Chem.* **17**, 5396–5407 (2009).
6. Kim, K. *et al.* High-throughput screening identifies two classes of

antibiotics as radioprotectors: Tetracyclines and fluoroquinolones. *Clin. Cancer Res.* **15**, 7238–7245 (2009).

7. Perrone, C. E., Takahashi, K. C. & Williams, G. M. Inhibition of human topoisomerase IIalpha by fluoroquinolones and ultraviolet A irradiation. *Toxicol. Sci.* **69**, 16–22 (2002).
8. Albini, A. & Monti, S. Photophysics and photochemistry of fluoroquinolones. *Chem. Soc. Rev.* **32**, 238–250 (2003).
9. Soldevila, S. & Bosca, F. Photoreactivity of fluoroquinolones: Nature of aryl cations generated in water. *Org. Lett.* **14**, 3940–3943 (2012).
10. Cuquerella, M. C., Miranda, M. A. & Boscá, F. Generation of detectable singlet aryl cations by photodehalogenation of fluoroquinolones. *J. Phys. Chem. B* **110**, 6441–6443 (2006).
11. Freccero, M. *et al.* Modeling the Photochemistry of the Reference Phototoxic Drug Lomefloxacin by Steady-State and Time-Resolved Experiments, and DFT and Post-HF Calculations. *Chem. - A Eur. J.* **14**, 653–663 (2008).
12. Fasani, E. *et al.* Fluoroquinolones as potential photochemotherapeutic agents: Covalent addition to guanosine monophosphate. *Org. Biomol. Chem.* **8**, 3621–3623 (2010).
13. Soldevila, S., Cuquerella, M. C. & Bosca, F. Understanding of the photoallergic properties of fluoroquinolones: Photoreactivity of lomefloxacin with amino acids and albumin. *Chem. Res. Toxicol.* **27**, 514–523 (2014).
14. Soldevila, S., Consuelo Cuquerella, M., Lhiaubet-Vallet, V., Edge, R. & Bosca, F. Seeking the mechanism responsible for fluoroquinolone photomutagenicity: A pulse radiolysis, steady-state, and laser flash photolysis study. *Free Radic. Biol. Med.* **67**, 417–425 (2014).
15. Anaya-Gonzalez, C., Soldevila, S., Garcia-Lainez, G., Bosca, F. & Andreu, I. Chemical tuning for potential antitumor fluoroquinolones. *Free Radic. Biol. Med.* **141**, 150–158 (2019).
16. Wicki, A., Witzigmann, D., Balasubramanian, V. & Huwyler, J.

Nanomedicine in cancer therapy: Challenges, opportunities, and clinical applications. *Journal of Controlled Release* vol. 200 138–157 (2015).

17. Tran, S., DeGiovanni, P.-J., Piel, B. & Rai, P. Cancer nanomedicine: a review of recent success in drug delivery. *Clin. Transl. Med.* **6**, (2017).
18. Duncan, R. & Gaspar, R. Nanomedicine(s) under the microscope. *Molecular Pharmaceutics* vol. 8 2101–2141 (2011).
19. Chen, G., Qiu, H., Prasad, P. N. & Chen, X. Upconversion nanoparticles: Design, nanochemistry, and applications in Theranostics. *Chemical Reviews* vol. 114 5161–5214 (2014).
20. Scheps, R. Upconversion laser processes. *Progress in Quantum Electronics* vol. 20 271–358 (1996).
21. Wolfbeis, O. S. An overview of nanoparticles commonly used in fluorescent bioimaging. *Chemical Society Reviews* vol. 44 4743–4768 (2015).
22. Yang, D. *et al.* Current advances in lanthanide ion (Ln3+)-based upconversion nanomaterials for drug delivery. *Chemical Society Reviews* vol. 44 1416–1448 (2015).
23. Liu, Y., Tu, D., Zhu, H. & Chen, X. Lanthanide-doped luminescent nanoprobes: Controlled synthesis, optical spectroscopy, and bioapplications. *Chem. Soc. Rev.* **42**, 6924–6958 (2013).
24. DaCosta, M. V., Doughan, S., Han, Y. & Krull, U. J. Lanthanide upconversion nanoparticles and applications in bioassays and bioimaging: A review. *Analytica Chimica Acta* vol. 832 1–33 (2014).
25. Gnach, A., Lipinski, T., Bednarkiewicz, A., Rybka, J. & Capobianco, J. A. Upconverting nanoparticles: Assessing the toxicity. *Chemical Society Reviews* vol. 44 1561–1584 (2015).
26. Gu, Z. *et al.* Recent advances in design and fabrication of upconversion nanoparticles and their safe theranostic applications. *Adv. Mater.* **25**, 3758–3779 (2013).
27. Ostańska, E., Aebisher, D. & Bartusik-Aebisher, D. The potential

of photodynamic therapy in current breast cancer treatment methodologies. *Biomedicine and Pharmacotherapy* vol. 137 111302 (2021).

28. Hu, T. *et al.* Recent advances in innovative strategies for enhanced cancer photodynamic therapy. *Theranostics* **11**, 3278–3300 (2021).
29. Xie, W. *et al.* Nanomaterial-based ROS-mediated strategies for combating bacteria and biofilms. *J. Mater. Res.* 1–24 (2021) doi:10.1557/s43578-021-00134-4.
30. Ding, S. *et al.* Near-infrared light excited photodynamic anticancer therapy based on UCNP@AIEgen nanocomposite. *Nanoscale Adv.* (2021) doi:10.1039/D0NA00985G.
31. Liu, Y., Meng, X. & Bu, W. Upconversion-based photodynamic cancer therapy. *Coordination Chemistry Reviews* vol. 379 82–98 (2019).
32. Dong, H., Sun, L. D. & Yan, C. H. Energy transfer in lanthanide upconversion studies for extended optical applications. *Chemical Society Reviews* vol. 44 1608–1634 (2015).
33. Jiang, G., Pichaandi, J., Johnson, N. J. J., Burke, R. D. & Van Veggel, F. C. J. M. An effective polymer cross-linking strategy to obtain stable dispersions of upconverting $NaYF_4$ nanoparticles in buffers and biological growth media for biolabeling applications. *Langmuir* **28**, 3239–3247 (2012).
34. Deng, R., Xie, X., Vendrell, M., Chang, Y. T. & Liu, X. Intracellular glutathione detection using MnO_2-nanosheet- modified upconversion nanoparticles. *J. Am. Chem. Soc.* **133**, 20168–20171 (2011).
35. Sedlmeier, A. & Gorris, H. H. Surface modification and characterization of photon-upconverting nanoparticles for bioanalytical applications. *Chemical Society Reviews* vol. 44 1526–1560 (2015).
36. Muhr, V., Wilhelm, S., Hirsch, T. & Wolfbeis, O. S. Upconversion nanoparticles: From hydrophobic to hydrophilic surfaces. *Acc.*

Chem. Res. **47**, 3481–3493 (2014).

37. Zhang, T., Ge, J., Hu, Y. & Yin, Y. A general approach for transferring hydrophobic nanocrystals into water. *Nano Lett.* **7**, 3203–3207 (2007).
38. Zhang, Z. *et al.* Upconversion superballs for programmable photoactivation of therapeutics. *Nat. Commun.* **10**, 1–12 (2019).
39. Chen, Q. *et al.* Functionalization of upconverted luminescent $NaYF_4$:Yb/Er nanocrystals by folic acid-chitosan conjugates for targeted lung cancer cell imaging. *J. Mater. Chem.* **21**, 7661–7667 (2011).

Chapter 6. Photochemistry of photoactivable 7-Aminocoumarin derivatives

6.1. Introduction

Among the light-responsive organic structures available, photolabile protecting groups (PPGs) represent key tools for biological and biomedical studies.[1] They, which are also called phototriggers, are able to mask the biological functions of bioactive messengers, drugs or neurotransmitters but a suitable light irradiation then triggers the physiological response by releasing the free molecule with remarkable temporal and spatial control. Thereby, in the last few years, PPGs have been widely used for caging biologically active molecules. In many cases, the photorelease of bioactive molecules is used with carriers such as biocompatible macromolecules, nanoparticles, proteins and nanocomposites. Especially in intracellular drug delivery systems, suitable carriers protect drugs from premature degradation, inhibit possible toxicities and control drug tissue distribution.[2] In this context, phototrigger-controlled drug-release nanosystems have been developed as promising tools for controlled-release drug delivery in tumour therapy. [3,4,5]

In general, although different types of caged biomolecules with a stable linkage have been developed for under *in vivo* conditions, all of them use phototriggers absorbing ultraviolet (UV) light to achieve cleavage, which is a major drawback because UV light is damaging to cells and it has poor penetration due to light scattering and absorbance by intrinsic biological chromophores.[6] In this context, to promote the application in biological areas, two approaches are being developed in designing biologically suitable phototriggers: one line of attack is to apply near-

infrared (NIR) light in a two photon excitation method[7] or using upconversion nanoparticles[8] and the second one is to design phototriggers absorbing at longer wavelengths. In this context many PPGs such as 2-nitrobenzyl, phenacyl, benzoin, 7-nitroindoline, and coumarin derivatives are being modified[4,7] to improve their absorption spectra. Recently, (Coumarin-4-yl)methyl derivatives based phototriggers have attracted much attention due to their photolysis efficiencies, long wavelength absorption and efficient fluorescence emissions.[2] They have been successfully applied to mask biological activity in phosphates, carboxylates, sulphates, sulfonates, diols, and carbonyl compounds.[4] Moreover, amino and hydroxyl functionalities have also been protected via carbamate or carbonate linkers.[4,9,10] The photochemical mechanisms involving the coumarin photocleavage have been investigated.[11–17] Hence, it has been well established that the photolysis of these members of arylalkyl-type PPGs occurs upon cleavage of a C–O bond, which generates an anionic leaving group and a coumarinyl carbocation that is subsequently trapped by the solvent.[12] In this context, it has been proposed that this trapping reaction competes with a recombination of the ion pair-separated state to the ground state of the caged compound. Several studies have modified the coumarin chromophore and the leaving group to understand the different efficiencies observed for this type of photolytic reaction. In this way, it has been observed that the efficiency of this process depends on the nucleofugality of the leaving group but it can be also improved adding electron-donating substituents in the coumarin scaffold or increasing the polarity of the medium.[12,17–19]

With this background, the prodrug **COU-DCO** was synthesized by linking a photolabile 7-amino-4-hydroymethylcoumarine chromophore (COU) to N-deacetylcolchicine (**DCO**), an antineoplastic agent,[20] via carbamate formation (see structure in Figure 6.1) with the aim to obtain a photoactivatable drug without the severe toxicity to normal tissues associated with colchicine derivatives.[21] However, the expected cleavage of a C–O bond was not produced when this prodrug was irradiated. Hence, an analysis of the photophysical properties of the coumarin chromophore **COU** alone and linked to **DCO** was performed to determine the process causing this unexpected photostability of **COU-DCO**. Thereby, femtosecond and nanosecond transient absorption spectroscopy together with steady state and time resolved emission techniques were used for this purpose. In this context, as an electron transfer process between **COU** and **DCO** chromophores could produce the inhibition of the photorelease of **DCO** from **COU-DCO**, a dyad without this possible electron transfer property such as **COU** linked to a phenyl alanine derivative PHA, compound **COU-PHA**, was also included in this study (see structure in Scheme 6.1).

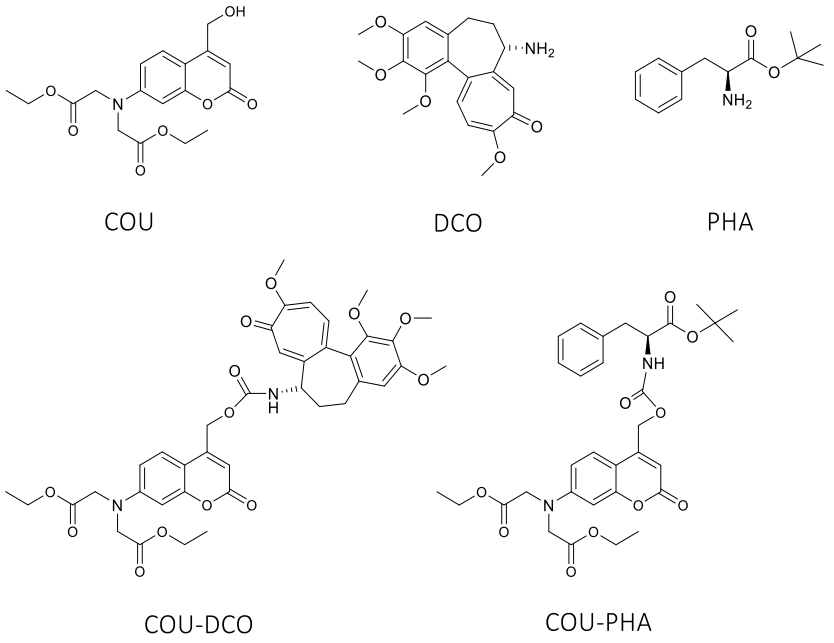

Scheme 6.1. Structures of **COU**, **DCO**, **PHA**, **COU-DCO** and **COU-PHA**.

6.2. Results and discussion

6.2.1. Photolysis of COU-DCO and COU-PHA

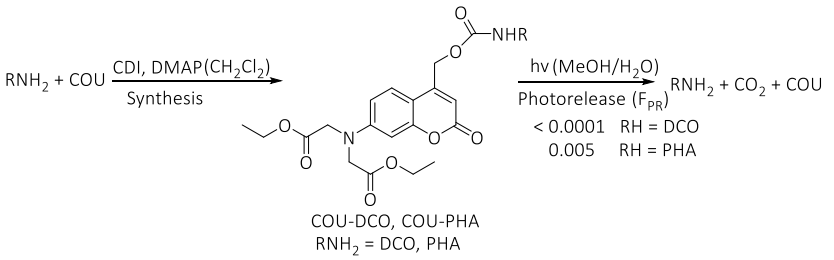

Scheme 6.2. Synthesis and photorelease process of **COU-DCO** and **COU-PHA**

Prodrug **COU-DCO** was synthesized by linking a photolabile 7-amino-4-hydroxymethylcoumarine chromophore (**COU**) to *N*-

deacetylcolchicine (**DCO**) , an antineoplastic agent,[20] via carbamate formation (see Scheme 6.1 and 6.2) with the aim to obtain a photoactivatable drug without the severe toxicity to normal tissues associated with colchicine derivatives.[21] Compound **COU-PHA** was also synthesized using the same procedure (see Scheme 6.2). Initially, photolytic studies were performed using lamps with emission at λ_{max} *ca*. 350 nm in an aerobic medium of MeOH/H_2O (9/1) to determine the capability of both compounds for releasing **DCO** and **PHA**. Thus, the results of the irradiations evidenced a fast photodegradation of both compounds (see Figure 6.1). A complete photodegradation was observed for **COU-DCO** in 15 min, however in the case of **COU-PHA,** after 60 min, *ca*. 20% still remained in the solution.

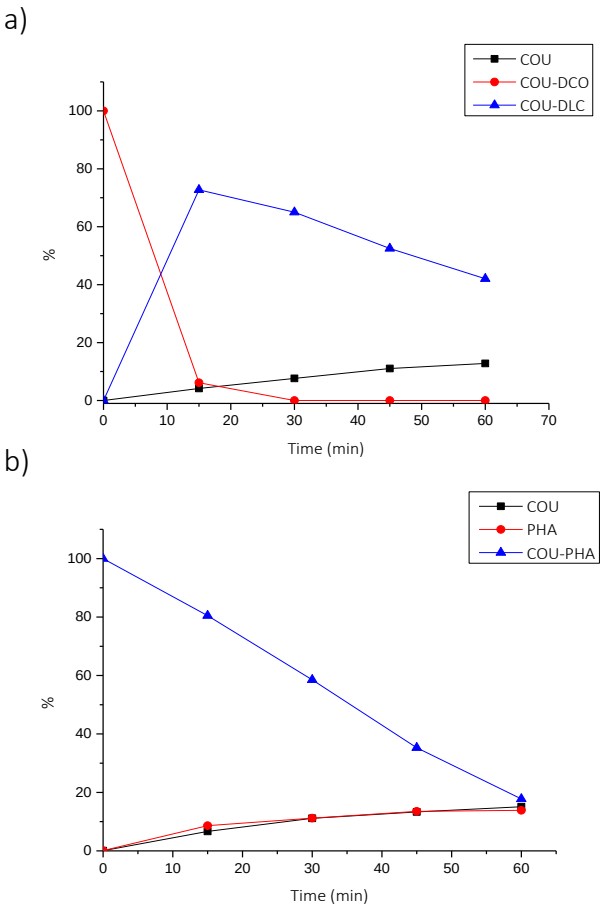

Figure 6.1. Photodegradation of a) **COU-DCO** and b) **COU-PHA** at λ_{max} *ca*. 350 nm in an aerobic medium of MeOH/H_2O (9/1)

However, the photorelease process of the compounds linked to the coumarine **COU** resulted to be very low and very inefficient. Thus, in the irradiated medium after 60 min of irradiation, detection of **PHA** released from **COU-PHA** was lower than 20% and for **COU-DCO** was not observed any amount of **DCO** in the irradiated sample. Nonetheless, these irradiations clearly evidenced the transformation of the **DCO**

linked to **COU** in a deacetillumicolchicine **DLC**, which is a compound formed from a cycloisomerization of the tropolone ring, which usually

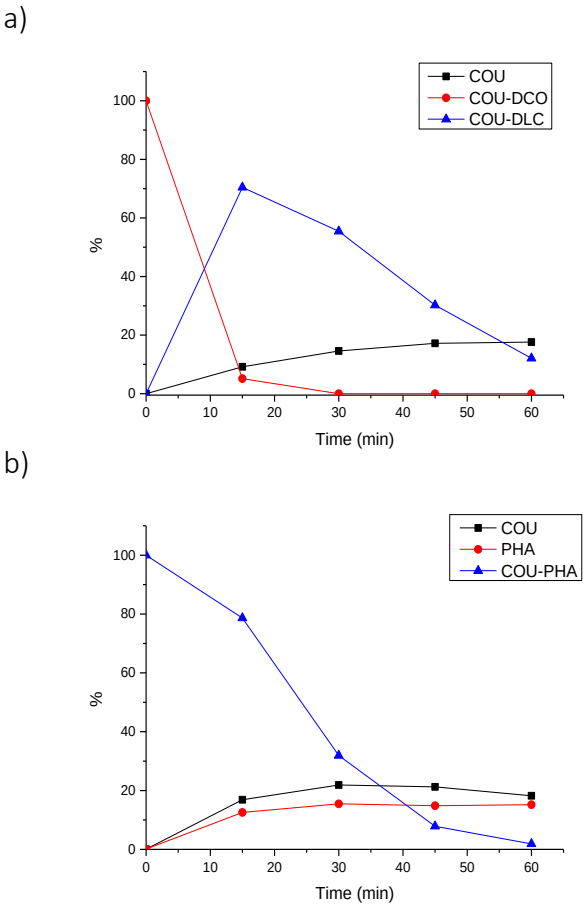

Figure 6.2. Photodegradation of a) **COU-PHA** and b) **COU-DCO** at λ_{max} *ca.* 350 nm in an aerobic medium of MeOH/H_2O (3/1)

occurs in colchinine derivatives in organic solvents.[22] Thereby, while **COU-DCO** and **COU-DLC** showed different peaks by HPLC analysis, using MS analysis the same molecular weight was observed for both dyads.

Interestingly, the photolysis of COU-PHA was faster when the study was performed using a solution with higher proportion of water (MeOH/H_2O 3/1, see Figure 6.2). Moreover, an increase of the release rate of COU and PHA was also detected during the first 15 min. These facts clearly evidence that water is needed for COU-PHA photolysis. By contrast, the rate of photolysis of COU-DCO did not change and the rate of COU released resulted to be lower than that observed in the photolysis of COU-PHA during its first minutes. These results are indicative that photolysis of COU-DCO is not water dependent and that the COU release is produced from its photoproduct COU-DLC.

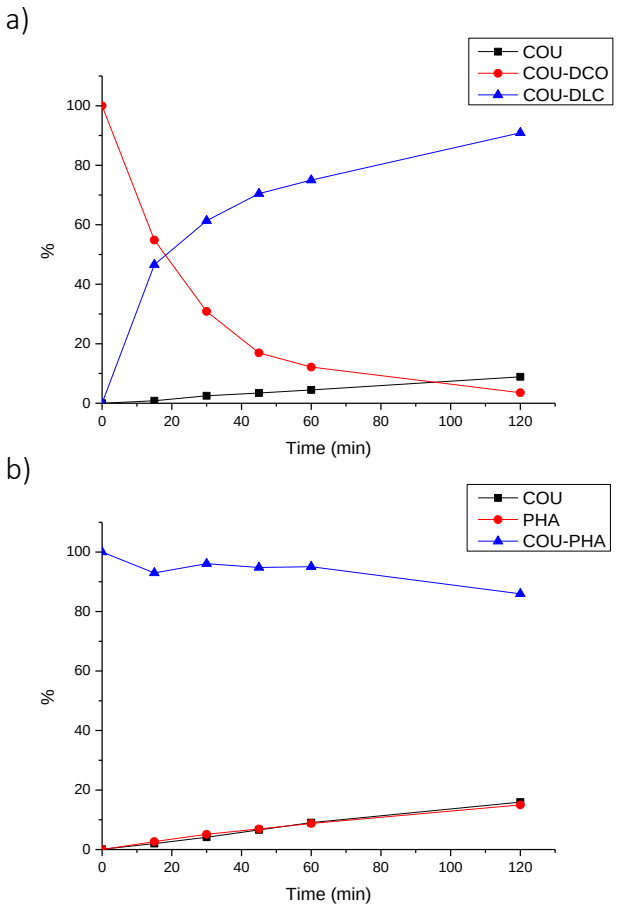

Figure 6.3. Photodegradation of a) **COU-DCO** and b) **COU-PHA** using lamps at λ_{max} *ca.* 420 nm in an aerobic medium of MeOH/H_2O (3/1)

Irradiations using lamps with emission at λ_{max} *ca.* 420 nm were also used in these studies with the aim to inhibit the photoisomerization of the colchicine derivative of **COU-DCO** into **COU-DLC**. Nevertheless, unfortunately, as shown in Figure 6.3, same photolytic processes were detected. In this case, photoisomerization process occurs more slowly than with the use of UVA lamps. Interestingly, using the visible light, the

photorelease of **COU** was a clean process arising from **COU-PHA** and from **COU-DLC** because the percentage of **COU** released was approximately the same as those detected for the **COU-PHA** and **COU-DLC** photodegraded. In this context, photorelease quantum yield (ϕ_{PR}) for **COU-PHA** and **COU-DCO** was determined using benzophenone/benzhydrol method (Table 6.1).

Table 6.1. Photophysical and photochemical properties of **DCO** and the coumarin derivatives **COU**, **COU-DCO** and **COU-PHA** using a methanol/water (9/1) mixture.

	DCO	COU	COU-DCO	COU-PHA
ϕ_F	$< 0.1 \times 10^{-3}$	0.57	0.09	0.53
$\lambda_{F\ (max,\ nm)}$	442	447	458	456
$\tau_{F\ (ns)}$	< 1	4.1	1.81	4.0
$E_{S\ (kJ/mol)}$	296	298	291	295
ϕ_{PR}	---	---	>0.0001	0.005

6.2.2. Photophysical Properties of COU-DCO and COU-PHA

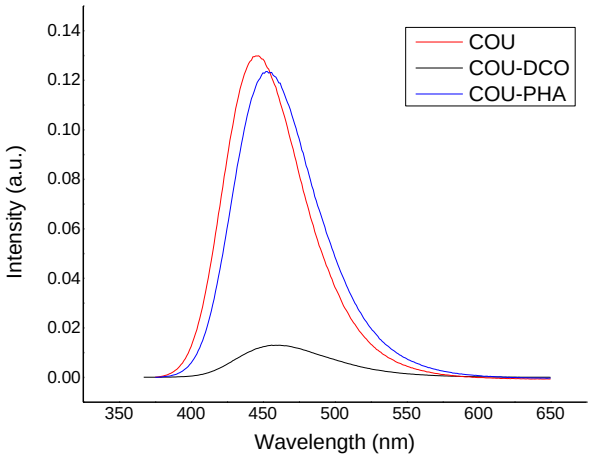

Figure 6.4. Emission of **COU**, **COU-DCO** and **COU-PHA** in methanol/water (9/1) mixture at room temperature

6.2.2.1. Emission Properties of COU-DCO and COU-PHA

To determine the photophysical properties of the singlet excited state of **COU-DCO** and **COU-PHA** steady state and time resolved emission measurements were performed at room temperature with these compounds dissolved in a methanol/water (9/1) mixture. Moreover, compounds **COU** and **DCO** were also studied under the same conditions as reference compounds. **PHA** was not included in this study because this compound does not absorb light at the excitation wavelengths of the photolysis performed.

Fluorescence of **COU-PHA** shows an emission maximum at 456 nm and a fluorescence quantum yield (ϕ_F) of 0.53, which are properties very close to those observed for **COU** under similar conditions (see

Figure 6.4 and Table 6.1). However, in the case of **COU-DCO**, although its emission maximum is also similar to the observed for **COU** and **COU-PHA**, its ϕ_F resulted to be considerably lower. In this context, **DCO** fluorescence was even lower. However, very small differences between the singlet excited state energies of **COU**, **COU-PHA**, **COU-DCO** and **DCO** were obtained when their values were determined from their emission and excitation spectra (Table 6.1). Interestingly, time resolved emission studies displayed a fluorescence lifetime (τ_F) for **COU** quite similar to **COU-PHA** but these τ_F are longer than those determined for **COU-DCO** and **DCO** (see Table 6.1). These results suggest that a new efficient process is only occurring from singlet excited state of **COU** linked to **DCO.**

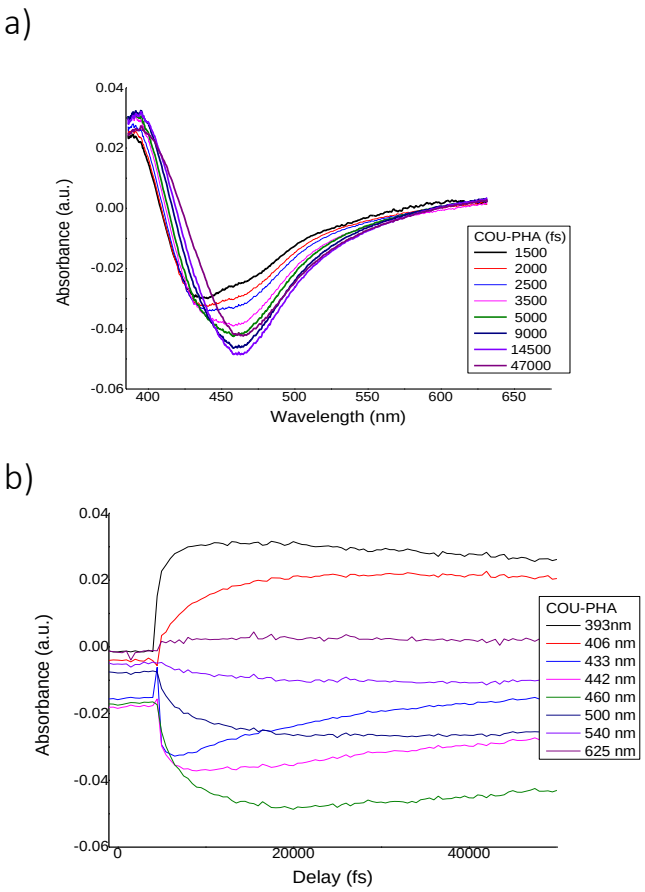

Figure 6.5. a) Transient absorption spectra of **COU-PHA** in MeOH/H_2O 3/1 registered at different times between laser excitation at 375 nm and 50 ps. b) The corresponding kinetics of transient at different wavelengths.

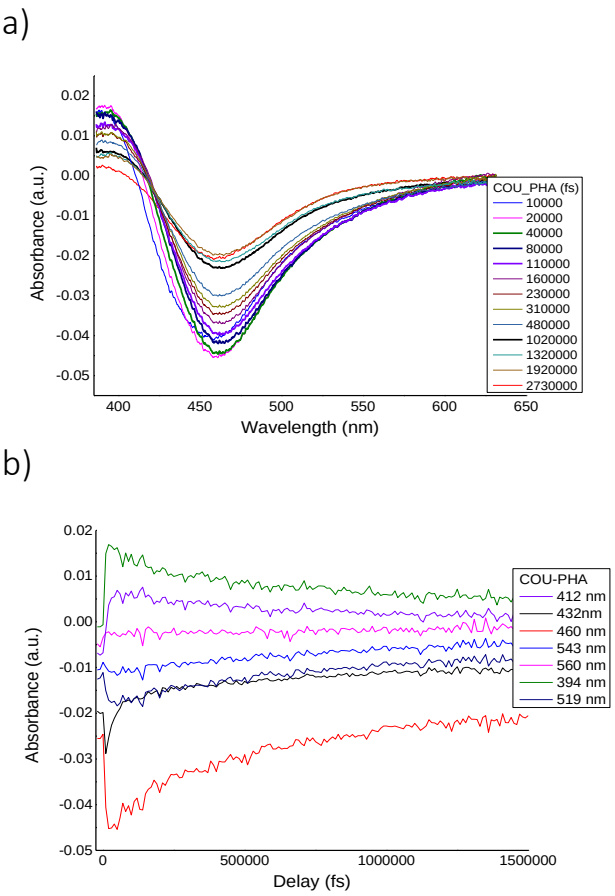

Figure 6.6. a) Transient absorption spectra of **COU-PHA** in MeOH/H_2O 3/1 registered at different times up to 2700 ps after laser excitation at 375 nm. b) The corresponding kinetics from the laser pulse to 1500 ps at different wavelengths.

6.2.2.2. Femtosecond transient absorption spectroscopy of COU-DCO and COU-PHA

Femtosecond transient absorption measurements were performed with **COU**, **DCO**, **COU-DCO** and **COU-PHA** with the aim to detect all the

short transient species formed after excitation of the coumarin derivative chromophore of **COU-DCO** and **COU-PHA**. The study performed with **COU** and **COU-PHA** shows the same intermediates and with similar lifetimes. In Figures 6.5 and 6.6 are shown the different transient species detected from **COU-PHA**. Hence, generation of an intermediate was detected during the initial few hundred femtoseconds after the laser pulse for both compounds. These transient species show a strong positive band located at around 390 nm and a broad negative band in the 420–550 nm region where the minimum is situated *ca.* 430 nm. A fitting analysis of the kinetic curve at 390 nm revealed a monoexponential component with a lifetime of *ca*. 1.5 ps for **COU-PHA** (see Figure 6.5.) The rapid absorption changes at these wavelengths also displayed a shift in the emission maximum (negative band) from 430 nm to 440 nm, which implies the generation of a second intermediate. In this context, the fact that an analysis of the kinetic curve at 428 nm shows a monoexponential fitting with a lifetime of *ca.*9 ps and a large red shift of the negative band of transient absorption spectrum is produced 15.5 ps after the laser pulse, implies the existence of another intermediate state (see Figure 6.5 for **COU-PHA**). The minimum of the negative band of this transient species is coincident with the fluorescence band maximum observed for **COU-PHA** and **COU** in steady state emission studies. Besides, the lifetime determined for the third intermediate of **COU-PHA** and **COU** (*ca.* 4 ns) is similar to these determined by time resolved emission studies (see Table 6.1). Thereby, as described in the literature for other coumarin derivatives[23,24] an initial generation of the coumarin singlet excited

state with an intramolecular charge transfer (ICT) character was detected. This ICT state undergoes in few picoseconds a stabilization after the diffusional solvent relaxation. Finally, a twisting of 7-amino substituent of this intermediate produces the formation of a twisted intramolecular charge transfer (TICT) state, which shows a lifetime of *ca*. 4 ns.

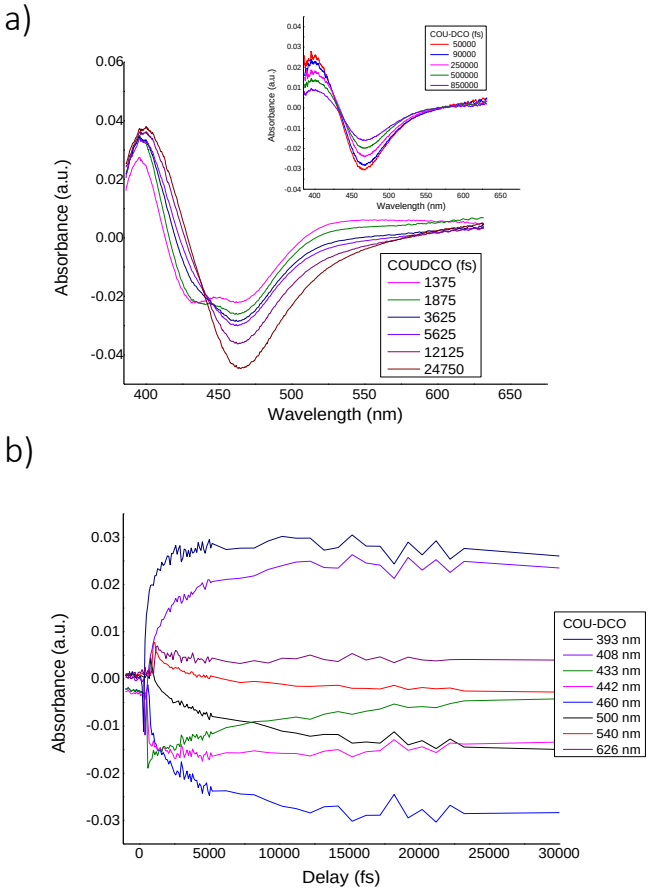

Figure 6.7. a) Transient absorption spectra of **COU-DCO** in MeOH/H_2O 3/1 registered at different times between the laser pulse excitation at 375 nm to 30 ps. Inset: Transient absorption spectra of **COU-DCO** in MeOH/H_2O 3/1 registered after 50 ps b) The corresponding kinetics from the laser pulse to 1500 ps at different wavelengths.

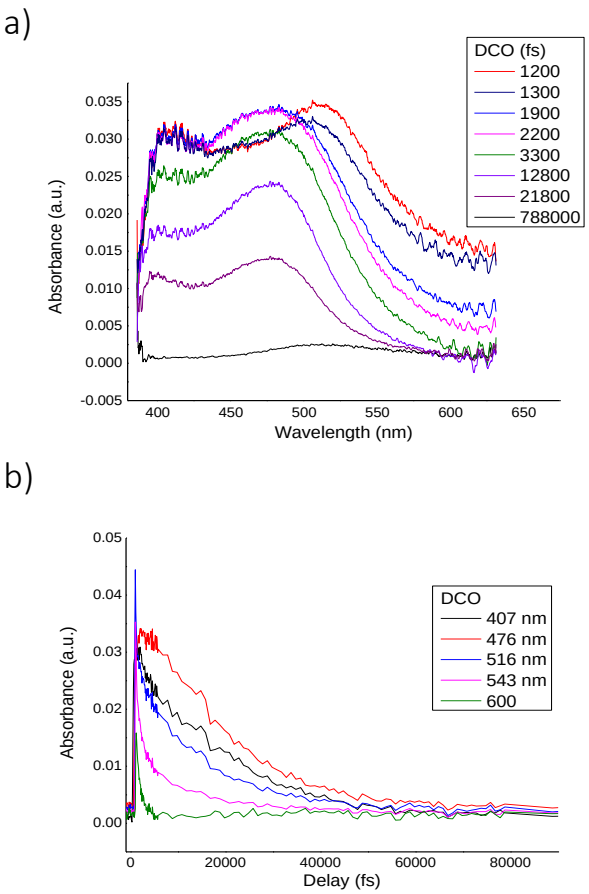

Figure 6.8. a) Transient absorption spectra of DCO in MeOH/H_2O 3/1 registered at different times after the laser pulse excitation at 375 nm b) The corresponding kinetics from the laser pulse to 80 ps at different wavelengths.

Transient absorption spectra obtained during the first 30 ps from **COU-DCO** solutions resulted to be very different than those obtained from **COU** and **COU-PHA** (see Figure 6.7 and compare with Figure 6.5). However, analysis of the traces obtained at 390 nm and 430 nm showed similar lifetimes (*ca* 1 ps at 390 nm and *ca*. 8 ps at 428 nm) than those detected for **COU** and **COU-PHA**. In this context, a study using **DCO** was

performed to determine the possible generation of fast transient species arising from **DCO** (see Figure 6.8). Thus, a strong band with a maximum at 515 nm appears instantaneously within the pulse duration and disappears within *ca*. 2ps leaving a broad structureless band with a maximum at around 480 nm and 410 nm. The second transient species showed a lifetime of *ca*. 30 ps. This implies that the excitation at 375 nm can populate an excited state that rapidly converts into a second one. Such a rapid process is consistent with a rearrangement of the structure and of the charges after Franck-Condon excitation. These intermediates can be assigned as described for similar transient species detected for colchicine, to the **DCO** singlet excited states S11 and its lowest S1.[25]. Thereby, the differences in the transient absorption spectra between **COU-PHA** and **COU-DCO** can be attributed to the short transient species generated from the direct excitation of the chromophore corresponding to **DCO**. In fact, the transient absorption spectra registered from **COU-DCO** after 50 ps of the laser pulse correspond to the same transient species than those detected from **COU-PHA** at the same times (see Figure 6.6a and inset Figure 6.7a). Interestingly, the last intermediate detected from **COU-DCO** excitation, its twisted intramolecular charge transfer (TICT) state, showed a lifetime of *ca*. 2 ns, which is similar to the **COU-DCO** emission lifetime and shorter than that detected for **COU-PHA**.

6.2.2.3. Nanosecond laser flash photolysis experiments using COU-DCO and COU-PHA

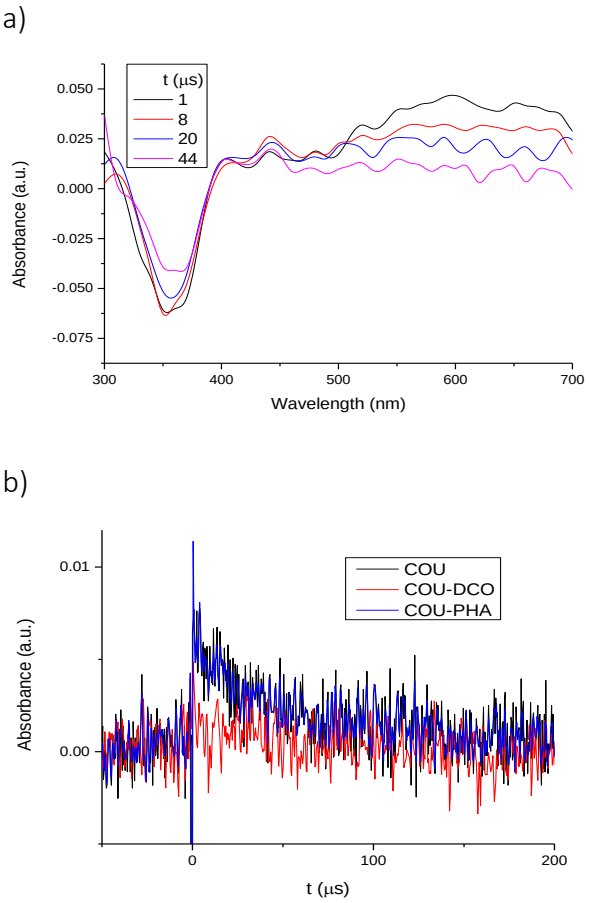

Figure 6.9. a) Transient absorption spectra of **COU-PHA** in deaerated MeOH/H_2O 3/1 medium registered at different times after the laser pulse excitation at 355 nm b) Kinetics obtained at 580 nm from **COU**, **COU-DCO** and **COU-PHA** in deaerated MeOH/H_2O 3/1 media.

Laser flash photolysis assays were performed with **COU**, **COU-DCO** and **COU-PHA** with the aim to detect their triplet excited states. Hence,

the studies were performed under anaerobic conditions. In the case of **COU** and **COU-PHA**, both compounds, in MeOH/H_2O 3/1 solutions, display the same transient species after excitation at 355 nm. The detected intermediate, accordingly with the literature,[26] was the triplet excited state of the coumarin chromophore (see Figure 6.9a). However, no signals were obtained performing the same experiments using **COU-DCO**. In fact, as it can be observed in Figure 6.9b, decay traces at the absorption maximum of these type of coumarin derivatives triplet excited state (*ca*. 580 nm) were only detected using **COU** and **COU-PHA**. Thus, it seems that the triplet excited state of **COU-DCO** is not generated.

Prodrug **COU-DCO** was synthesized by linking a photolabile 7-amino-4-hydroymethylcoumarine chromophore (**COU**) to *N*-deacetylcolchicine (**DCO**) , an antineoplastic agent,[20] via carbamate formation (see Scheme 6.1 and Scheme 6.2). However, liberation of the drug was not detected when the prodrug was irradiated using UVA light and also visible light at λ_{max} *ca.* 420 nm in a methanol/aqueous medium. This unexpected result would be produced due to some photophysical property of **DCO** because it is well known that this coumarin derivative is able to photorelease other drugs.[4,27,28] Two processes could explain the photostability observed for **COU-DCO**. One could be the generation of an energy transfer process from the singlet excited estate of **COU** (^{1}**COU**) to **DCO** with the subsequent fast deactivation of the ^{1}**DCO**. In fact, the efficient ultrafast internal conversion of colchicine derivatives is well known [25,29]The second one would be through an electron

transfer process between the singlet excited estate of **COU** (^{1}**COU**) and **DCO** followed by back electron transfer reaction. The possibility that an initial electron transfer process between ^{1}**COU** and **DCO** to generate their corresponding radicals (see Equations 6.1 and 6.2 respectively) could occur was initially analyzed determining Gibbs free energies (ΔG_{PET}) of the redox processes by using the Rehm-Weller equation 6.3:[30]

$$^1COU + DCO \rightarrow COU^{\cdot -} + DCO^{\cdot +} \qquad \text{Eq. 6.1}$$

$$^1COU + DCO \rightarrow COU^{\cdot +} + DCO^{\cdot -} \qquad \text{Eq. 6.2}$$

$$\Delta G_{et} = E_{ox} - E_{red} - E_S \qquad \text{Eq. 6.3}$$

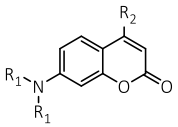

COU COU1

R_1 = -CH_2-COOEt, -CH_2-CH_3

R_2 = -CH_2-OH, -CH_3

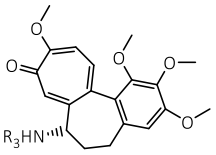

DCO COL

R_3 = -H -CO-CH_3

PHA BZ

R_4 = -CH_2CHNH_2-COOC$(CH_3)_3$ -H

Scheme 6.3. Chemical structure of the protecting group **COU**, the caged compounds **DCO** and **PHA**, and their chromophoric analogues of them such as **COU1**, colchicine (**COL**) and benzene (**BZ**) respectively.

Table 6.2. Redox potential of **COU1**, **COL** and **BZ**

	E_{red} (V)[a]	E_{ox} (V)[a]
COU1[b]	-2.20	1.09
COL[c]	-1.04	1.22
BZ	-3.42[d]	2.48[e]

[a]Potentials in V vs SCE. [b]Ref.[31],[c]Ref.[32] ,[d]Ref.[33],[e] Ref.[34].

The redox potentials of **COU1** and **COL** (see values in Table 6.2 and structures in Figure 6.10)[3135]and the E_s determined for **COU-DCO** (see Table 6.1) were used to determine ΔG_{PET} of the electron transfer processes between the singlet excited state of the coumarin chromophore and the colchicine derivative ground state. Thereby, as results indicated that this electron transfer could occur, compound **COU-PHA** was synthesized for this study in order to compare the photophysical and photochemical properties of both dyads. **COU-PHA** was chosen for this study because the ΔG_{PET} for an electron transfer process to occur between **COU** and a phenyl derivative is theoretically not possible (see Figure 6.10 and Table 6.2).

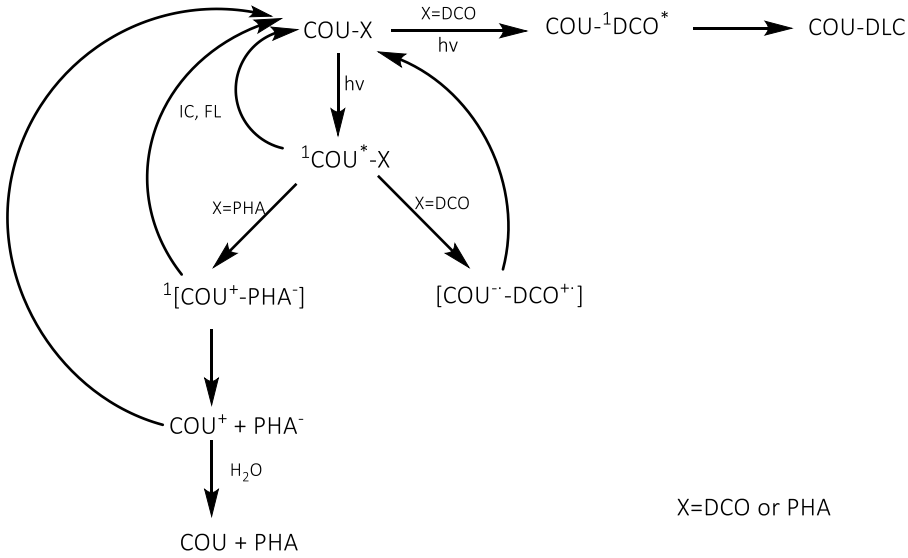

Scheme 6.4. Main processes involved in the photodegradation of COU-PHA and COU-DCO.

Thus, considering all the results obtained in this study, the main processes involved in the photodegradation of **COU-PHA** and **COU-DCO** are summarized in Scheme 6.4. After the analysis of the redox potential commented above, the results of the irradiations performed with **COU-DCO** and **COU-PHA** have been proposed as well as the analysis of all the data obtained in the photophysical studies performed with **COU**, **PHA**, **DCO**, **COU-PHA** and **COU-DCO.**

Thereby, although two deactivation processes were initially proposed to justify the absence of **DCO** photorelease from **COU-DCO**, an efficient energy transfer process between the chromophores of **COU-DCO** can be discarded because the energy determined for ^{1}COU and ^{1}DCO from their fluorescence resulted to be very similar (see Table 6.1) and it is

generally accepted that the rate constant for an energy transfer reaction is nearly diffusion-controlled only when the energy level of the donor is at least 8 kJ/mol above that of the acceptor.[36] Thus, only an electron transfer can occur. This process explains why **COU-DCO** fluorescence lifetime and quantum yield are lower than those determined for **COU** alone or for **COU-PHA** (see Table 6.1) Interestingly, these findings can also be correlated with the absence of **COU** or **DCO** photorelease during the first minutes of the **COU-DCO** irradiations. Moreover, it was observed that the intensity of the fluorescence of a solution of **COU-DCO** irradiated 15 min at λ_{max} *ca*. 350 nm in an aerobic medium of MeOH/H_2O (9/1, see Figure 6.1) increased along with the emission lifetime (data not showed). These results clearly indicate that when **COU-DCO** is phototransformed in **COU-DLC**, fluorescence quantum yield and emission lifetime of **COU** linked to **DLC** is similar to that determined for **COU-PHA**. In fact, both dyads seem to photorelease **COU** with similar efficiency (Figure 6.1-3). The effect of the water in the photorelease process of **COU** was clearly evidenced when with different amounts of water were used in the solution mixture (Figure 6.1 -2). Femtosecond studies have shown that the electron transfer process occurs from the twisted intramolecular charge transfer (TICT) singlet excited state of the **COU** chromophore because the other intermediates generated after excitation of all coumarin derivatives showed similar behaviour. The existence of this electron transfer process also explains why the triplet excited state of **COU-DCO** is not detected.

6.3. Conclusions

Photophysical and photochemical properties of **COU** are modified when the linked chromophore is able to generate an electron transfer process with the excited state of the coumarin chromophore. This study has clearly evidenced this fact using compounds **COU**, **COU-DCO** and **COU-PHA**. Moreover, the intermediated responsible of this type of electron transfer process has been established. It is also noteworthy that an initial analysis of redox properties and energies of the excited states of the compound to link are key points to prepare phototrigger-controlled drug-release nanosystems.

6.4. Experimental section

6.4.1. Materials

Selenium dioxide, ethyl bromoacetate, 4-(dimethylamino)pyridine, NaI, diisopropylethylamine, ethyl bromoacetate, di-*tert*-butyl decarbonate, 4-(dimethylamino)pyridine, triethylamine, trifluoroacetic acid, N,N'-carbonyldiimidazole and sodium methoxide solution (25 wt. % in methanol) were commercial products obtained from Sigma-Aldrich Chemical Company. 7-Amino-4-methylcoumarin was commercial product from Fluorochem. Colchicine and L-Phenylalanine *tert*-butyl ester hydrochloride were commercial products from Carbosynth. Sodium phosphate buffer (PB) was prepared from reagent-grade product from Sigma Aldrich using milli-Q water. One tablet dissolved in 200 mL of deionized water yields 0.01 M phosphate buffer, pH 7.4, at 25 °C. Other chemicals were of reagent grade and used as received.

6.4.2. Synthesis of COU, COU-DCO and COU-PHA

7-[bis(ethoxycarbonylmethyl)lamino]-4-methylcoumarin. It was synthesized using the methodology described in the literature.[37] 7-Amino-4-methylcoumarin (34.25 mmol, 6 g), NaI (34.25 mmol, 5.14 g), diisipropylethylamine (172.61 mmol, 30 mL), and ethyl bromoacetate (0.35 mol, 39 mL) in 165 mL of dry CH_3CN were refluxed for 4 days under nitrogen atmosphere. The mixture was cooled to room temperature, filtered and the solvent was removed under reduced pressure. The residue was dissolved in EtOAc, washed with water and brine, dried over $MgSO_4$, and concentrated under vacuum. The resulting oil was purified by silica-gel column chromatography (EtOAc/ Cyclohexane 1:1) to yield 1 (7.1 g, 20.55 mmol, 60%).

^{1}H NMR (300 MHz, $CDCl_3$) δ 7.42 (d, *J* = 8.8 Hz, 1H), 6.55 (dd, *J* = 8.8, 2.6 Hz, 1H), 6.47 (d, *J* = 2.6 Hz, 1H), 6.03 (d, *J* = 1.1 Hz, 1H), 4.20 (q, *J* = 7.0 Hz, 4H), 4.10 (s, 4H), 2.34 (d, *J* = 1.1 Hz, 3H), 1.28 (q, *J* = 7.0 Hz, 6H). MH^+ calculated for *7-[bis(ethoxycarbonylmethyl)lamino]-4-methylcoumarin* ($C_{18}H_{22}NO_6$): 348.1448, found: 348.1455

7-[bis(ethoxycarbonylmethyl)lamino]-4-(hydroxymethyl)coumarin (COU). To a solution of 138 mL *p*-xylene selenium dioxide (19.81 mmol, 2.21 g) and 7-[bis(ethoxycarbonylmethyl)lamino]-4-methylcoumarin (13.36 mmol, 5 g) were added. The mixture was refluxed with vigorous stirring under a nitrogen atmosphere during 24 h. Afterwards it was filtered and concentrated under reduced pressure. The dark brown residual oil was dissolved in ethanol (100 mL) and then, sodium

borohydride (6.76 mmol, 252.67 mg) was added. This mixture was stirred for 1 h at room temperature. Thereafter, the suspension was hydrolyzed adding HCl 1 M (10.5 mL). The solution was partially concentrated under reduced pressure to remove EtOH. Then, the aqueous mixture was extracted with EtOAc. The organic phase was washed H_2O and brine, dried over $MgSO_4$, and concentrated under vacuum. The resulting oil was purified by silica-gel column chromatography (EtOAc/Cyclohexane 1:1) to yield **COU** (2.66 g, 7.3 mmol, 55 %).

^{1}H NMR (300 MHz, $CDCl_3$) δ 7.23 (d, *J* = 8.7 Hz, 1H), 6.47 (dd, *J* = 8.7, 2.6 Hz, 1H), 6.43 (d, *J* = 2.6 Hz 1H), 6.28 (s, 1H), 4.68 (s, 2H), 4.25 (q, *J* = 7.7 Hz, 4H), 4.10 (s, 4H), 1.27 (t, *J* = 7.4 Hz, 6H). MH^+ calculated for **COU** ($C_{18}H_{22}NO_7$): 364.1397, found: 364.1405.

N-deacetylcolchicine (**DCO**). It was synthesized using the methodology described in the literature.[38,39] Colchicine (8 g, 20.03 mmol) was dissolved in 81 mL of acetonitrile. To this were added 4-(dimethylamino) pyridine (2.45 g, 20.03 mmol), triethylamine (5.44 mL, 36.17 mmol), and di-*tert*-butyl dicarbonate (10.54 g, 48.28 mmol). The reaction flask was attached to a reflux condenser and heated at 100 °C. After 1 h additional di-*tert*-butyl dicarbonate (9.6 g, 43.9 mmol) was added. The reaction was quenched by the addition of 300 mL of CH_2Cl_2 and was washed with 3 × 200 mL of saturated aqueous citric acid. The combined aqueous layers were back extracted with 30 mL of CH_2Cl_2, and the organic layers combined. The organic layer was washed with 100 mL of saturated brine and then concentrated to a reddish brown

solid. The crude sample was carried on through the next step. The crude *N*-Boc-colchicine was dissolved in 115 mL of anhydrous methanol. To this was added sodium methoxide in methanol (26 mL 25% w/v) at 4°C. The solution was stirred at room temperature and monitored via thin layer. After 50 min the solution was transferred to 105 mL brine and extracted with 3 × 200 mL of diethyl ether. The product was dried over $MgSO_4$, filtered, and concentrated to a crude solid. The crude sample was carried through the next reaction. *N*-Boc-deacetylcolchicine was dissolved in CH_2Cl_2 (115 mL) after which TFA (26 mL) was added. The reaction mixture was stirred for 2 h after which a saturated sodium carbonate solution (pH *ca.* 10) was carefully added to quench the reaction. This was extracted twice with CH_2Cl_2 and once with EtOAc. After pooling the organic fractions, drying over $MgSO_4$ and concentration *in vacuo*, a thick brown oil was obtained. After silica-gel column chromatography with CH_2Cl_2/MeOH/Et_3N (90:10:0.1) and concentration, **DCO** was obtained as a slightly yellow solid (3.8 g, 54%). MH^+ calculated for **DCO** ($C_{20}H_{23}NO_5$): 357.1516, found: 358.1658.

^{1}H NMR (300 MHz, $CDCl_3$) δ 7.69 (s, 1H), 7.18 (s, 1H), 6.78 (d, *J* = 6.6 Hz, 1H), 6.52 (d, *J* = 4.4 Hz, 1H), 3.97 (s, 1H), 3.91 (s, 1H), 3.74 – 3.68 (m, 1H), 3.66 – 3.63 (m, 1H), 2.51 – 2.24 (m, 1H).

COU-DCO. COU (1.062 g, 2.9 mmol) was added to a suspension of N,N'-carbonyldiimidazole (542.58 mg, 3.35 mmol) in anhydrous dichloromethane (78 mL). The mixture was refluxed in the dark and under nitrogen. After 4 h, a small sample was taken for analysis. The formation of the carbamate intermediate was confirmed by thin layer

chromatography. The reaction mixture was cooled to room temperature, then 4-dimethylaminopyridine (171.04 mg, 1.4 mmol), ***DCO*** (1 g, 2.8 mmol) and dichloromethane (62 mL) were added. The resulting solution was heated to reflux for 4 h, then overnight at room temperature. After concentration under reduced pressure, the crude residue was purified by silica-gel column chromatography (EtOAc/MeOH 93:7) to yield ***COU-DCO*** as a yellow powder (700 mg, 34 %). MH^+ calculated for **COU-DCO** ($C_{39}H_{43}N_2O_{13}$): 747.2765, found: 747.2765.

^{1}H NMR (300 MHz, $CDCl_3$) δ 7.62 (s, 1H), 7.29 (d, *J* = 11.0 Hz, 1H), 7.23 (d, *J* = 8.8 Hz, 1H), 6.85 (d, *J* = 11.0 Hz, 1H), 6.56 (s, 1H), 6.49 (dd, *J* = 8.9, 2.5 Hz, 1H), 6.45 (d, *J* = 2.5 Hz, 1H), 6.41 (d, *J* = 7.2 Hz, 1H), 5.30 (d, *J* = 15.5 Hz, 1H), 4.86 (d, *J* = 15.5 Hz, 1H), 4.50 – 4.39 (m, *J* = 12.3, 5.9 Hz, 1H), 4.22 (q, *J* = 7.1 Hz, 4H), 4.15 (s, *J* = 7.5 Hz ,4H), 4.00 (s, 3H), 3.91 (d, *J* = 4.6 Hz, 6H), 3.53 (s, *J* = 19.3 Hz, 3H), 2.60 – 2.51 (m, 1H), 2.44 – 2.28 (m, 2H), 1.98 – 1.84 (m, 1H), 1.66 (s, 1H), 1.28 (t, *J* = 7.1 Hz, 8H).

^{13}C NMR (75 MHz, $CDCl_3$) δ 179.63 (s), 169.76 (s), 164.28 (s), 161.44 (s), 155.60 (s), 154.68 (s), 153.67 (s), 151.23 (s), 151.07 (s, *J* = 12.4 Hz), 150.97 (s), 149.94 (s), 141.76 (s), 136.21 (s), 135.42 (s), 134.31 (s), 131.40 (s), 125.58 (s), 124.63 (s), 112.63 (s), 109.47 (s), 108.49 (s, *J* = 25.6 Hz), 108.15 (s), 107.52 (s), 99.62 (s), 61.73 (s, *J* = 9.2 Hz), 61.50 (s), 61.29 (s), 56.48 (s, *J* = 19.5 Hz), 56.23 (s), 54.29 (s), 53.49 (s), 37.21 (s), 30.03 (s), 14.32 (s).

COU-PHA. **COU** (200 g, 0.55 mmol) was added to a suspension of N,N'-carbonyldiimidazole (102.69 mg, 0.63 mmol) in anhydrous

dichloromethane (14 mL). The mixture was refluxed in the dark and under nitrogen. After 4 h, a small sample was taken for analysis. The formation of the carbamate intermediate was confirmed by thin layer chromatography. The reaction mixture was cooled to room temperature, then 4-dimethylaminopyridine (30.5 mg, 0.25 mmol), L-Phenylalanine *tert*-butyl ester hydrochloride (PHA, 178.7 mg, 0.5 mmol) and dichloromethane (12 mL) were added. The resulting solution was heated to reflux for 4 h, then overnight at room temperature. After concentration under reduced pressure, the crude residue was purified by silica-gel column chromatography (EtOAc/Cyclohexane 2:1) to yield **COU-PHA** as a yellow powder (260 mg, 42 %). MH^+ calculated for COU-PHA($C_{32}H_{39}N_2O_{10}$): 610.25, found: 611.2585.

^{1}H NMR (300 MHz, $CDCl_3$) δ 7.35 – 7.28 (m, 3H), 7.24 (s, 1H), 7.18 (d, *J* = 1.5 Hz, 1H), 7.15 (s, 1H), 6.53 (dd, *J* = 8.8, 2.5 Hz, 1H), 6.49 (d, *J* = 2.5 Hz, 1H), 6.19 (s, 1H), 5.38 (d, *J* = 8.0 Hz, 1H), 5.20 (d, *J* = 12.0 Hz, 2H), 4.53 (dd, *J* = 14.0, 6.1 Hz, 1H), 4.24 (q, *J* = 7.1 Hz, 5H), 4.17 (s, 4H), 3.10 (dd, *J* = 5.8, 2.1 Hz, 2H), 1.59 (s, 2H), 1.42 (s, 11H), 1.29 (q, *J* = 13.6, 6.4 Hz, 12H).

^{13}C NMR (75 MHz, $CDCl_3$) δ 170.11 (s), 169.44 (s), 161.06 (s), 155.39 (s), 154.48 (s), 150.78 (s), 149.57 (s), 135.64 (s), 129.26 (s), 128.32 (s), 126.92 (s), 124.40 (s), 109.09 (s), 108.26 (s), 108.16 (s, *J* = 7.6 Hz), 99.37 (s), 82.39 (s), 61.62 (s), 61.41 (s, *J* = 16.3 Hz), 55.15 (s), 53.20 (s), 38.14 (s), 27.75 (s), 14.00 (s).

6.4.3. Photolysis studies with CUO-DCO and COU-PHA

Irradiations were performed in a Luzchem photoreactor (model LZC-4V) equipped with eight lamps emitting in the 310-390 nm range (Gaussian distribution), with a maximum at 350 nm and other ones emitting in the 390-430 nm range (Gaussian distribution), with a maximum at 420 nm. All irradiations were performed under aerated medium at 10^{-4} M concentrations of each compound excluding the study for determining the photo-release quantum yield of COU-DCO and COU-PHA, which was performed under aerobic conditions using a solution of MeOH/10% H_2O at the absorbance of 1. As actinometer was used the photoreaction of benzophenone (absorbance of 1 at 350 nm)/benzhydrol (0.1 M) using $\phi = 0.68$.[40] All irradiations were done at room temperature using 1 cm pathway quartz cells with 4 mL capacity. The samples were irradiated during 30 min taking aliquots after 5, 10, 20, 30, minutes of irradiation. Afterwards, COU-DCO and COU-PHA samples were monitored by HPLC on an analytical C18 column (25 x 0.4 cm, mean particle size 5 μm) with flow rate of 0.7 mL/min, and a mixture of acetonitrile/water/trifluoroacetic acid 50/49.9/0.1 was used as eluent. In the case of the benzophenone samples, they were analyzed by UV-Vis spectroscopy determining the decrease of the absorbance at 360 nm.

6.4.4. Laser flash photolysis experiments

A pulsed Nd:YAG laser was used for the excitation at 355 nm. The single pulses were ~10 ns duration and the energy was from 10 mJ/puls

The laser was a Lotis TII and the home-made detection system consisted of the pulsed laser, the Xe lamp, a monochromator and a photomultiplier made up of a tube, housing and power supply. The output signal from the oscilloscope was transferred to a personal computer. The studies were performed with 3 x 10^{-5} M **COU** and **COU-DCO** and **COU-PHA** in methanol-buffered solutions of 1 mM PB (3/1). The experiments were registered under aerobic and anaerobic conditions.

6.5. NMR Spectra

^{1}H COU

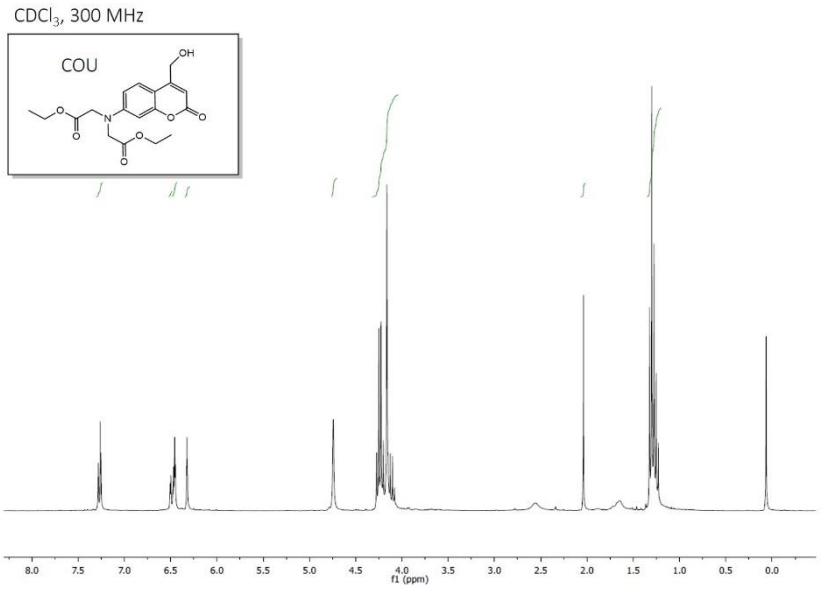

^{1}H DCO

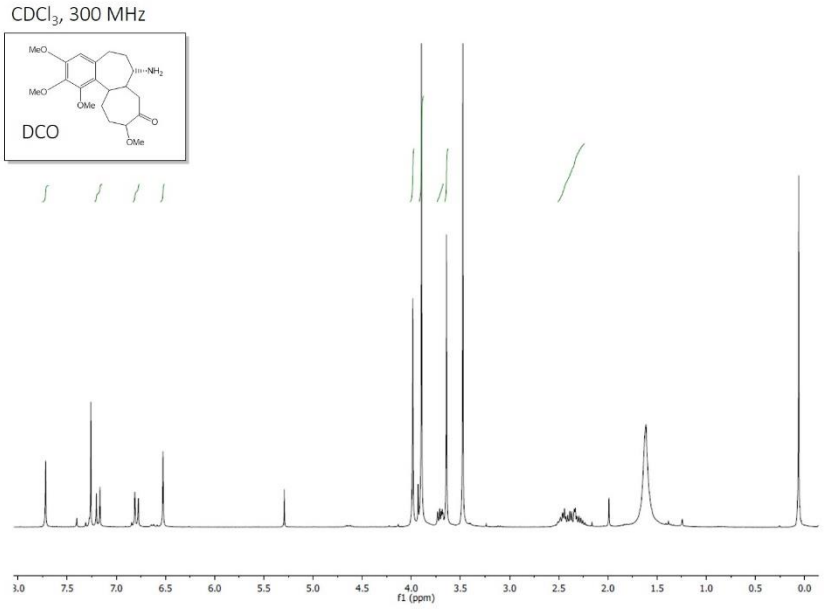
CDCl3, 300 MHz
MeO
MeO
OMe
NH2
O
OMe
DCO
7.5
7.0
6.5
6.0
5.5
5.0
4.5
4.0
3.5
3.0
2.5
2.0
1.5
1.0
0.5
0.0
f1 (ppm)

^{1}H COU-DCO

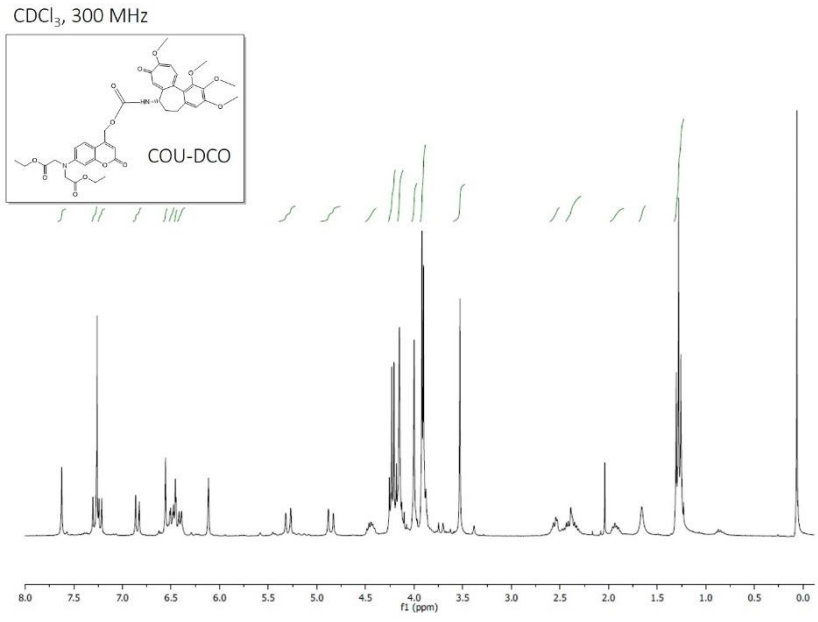
CDCl3, 300 MHz
COU-DCO
8.0
7.5
7.0
6.5
6.0
5.5
5.0
4.5
4.0
3.5
3.0
2.5
2.0
1.5
1.0
0.5
0.0
f1 (ppm)

^{13}C COU-DCO

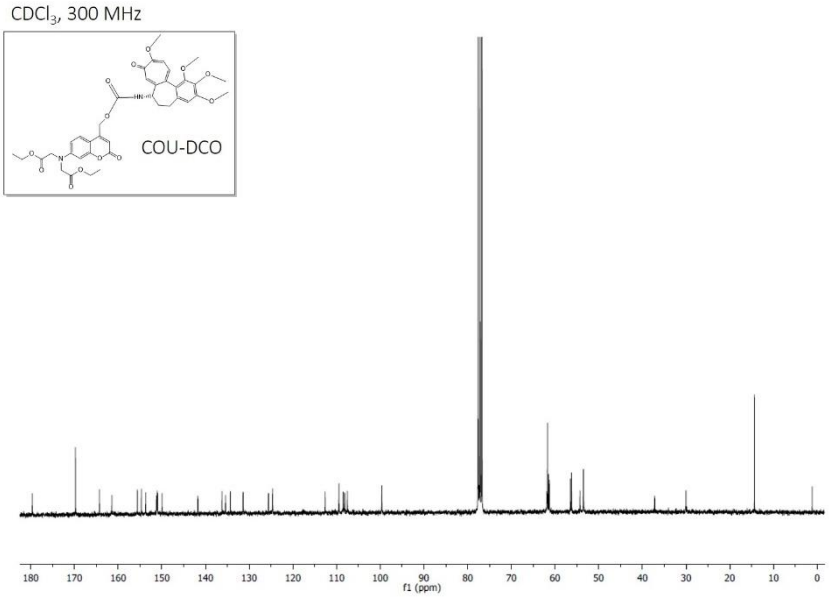
CDCl3, 300 MHz
COU-DCO
180
170
160
150
140
130
120
110
100
90
80
70
60
50
40
30
20
10
0
f1 (ppm)

^{1}H COU-PHA

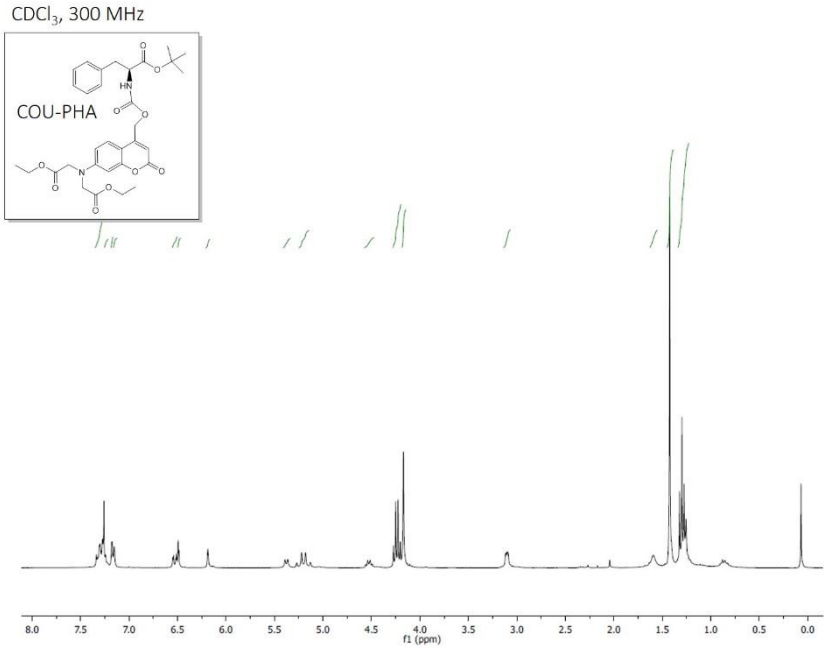
CDCl3, 300 MHz
COU-PHA
8.0
7.5
7.0
6.5
6.0
5.5
5.0
4.5
4.0
3.5
3.0
2.5
2.0
1.5
1.0
0.5
0.0
f1 (ppm)

^{13}C COU-PHA

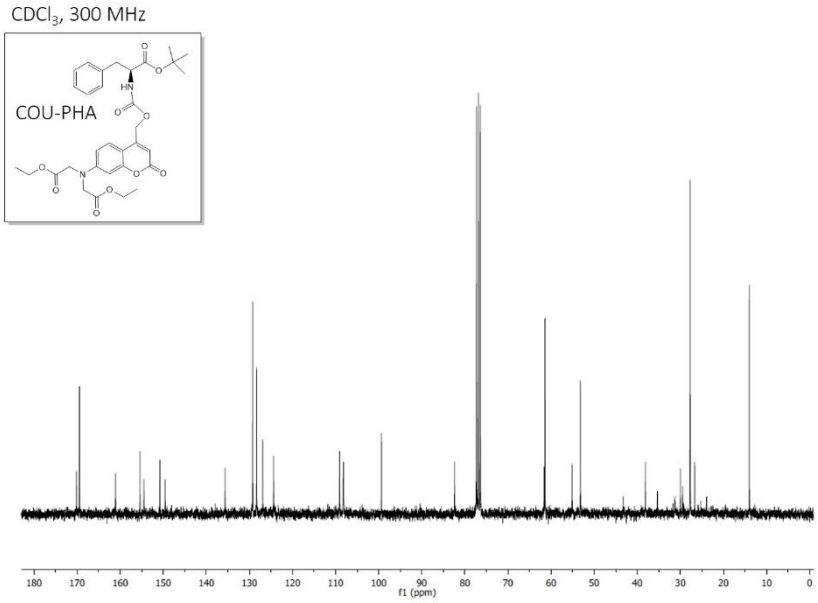

6.6. References

1. Lavis LD, Raines RT. Bright ideas for chemical biology. *ACS Chem Biol*. 2008;3(3):142-155.
2. Lin Q, Bao C, Fan G, et al. 7-Amino coumarin based fluorescent phototriggers coupled with nano/bio-conjugated bonds: Synthesis, labeling and photorelease. *J Mater Chem*. 2012;22(14):6680-6688.
3. Wong PT, Choi SK. Mechanisms of Drug Release in Nanotherapeutic Delivery Systems. *Chem Rev*. 2015;115(9):3388-3432.
4. Klán P, Šolomek T, Bochet CG, et al. Photoremovable protecting groups in chemistry and biology: Reaction mechanisms and efficacy. *Chem Rev*. 2013;113(1):119-191.
5. Li X, Mu J, Liu F, et al. Human transport protein carrier for

controlled photoactivation of antitumor prodrug and real-time intracellular tumor imaging. *Bioconjug Chem*. 2015;26(5):955-961.

6. Schwarz A, Ständer S, Berneburg M, et al. Interleukin-12 suppresses ultraviolet radiation-induced apoptosis by inducing DNA repair. *Nat Cell Biol*. 2002;4(1):26-31.
7. Bao C, Fan G, Lin Q, et al. Styryl conjugated coumarin caged alcohol: Efficient photorelease by either one-photon long wavelength or two-photon NIR excitation. *Org Lett*. 2012;14(2):572-575.
8. Chen S, Weitemier AZ, Zeng X, et al. Near-infrared deep brain stimulation via upconversion nanoparticle–mediated optogenetics. *Science (80-)*. 2018;359(6376):679-684.
9. Takaoka K, Tatsu Y, Yumoto N, Nakajima T, Shimamoto K. Synthesis of carbamate-type caged derivatives of a novel glutamate transporter blocker. *Bioorganic Med Chem*. 2004;12(13):3687-3694.
10. Suzuki AZ, Watanabe T, Kawamoto M, et al. Coumarin-4-ylmethoxycarbonyls as Phototriggers for Alcohols and Phenols. *Org Lett*. 2003;5(25):4867-4870.
11. Schade B, Hagen V, Schmidt R, et al. Deactivation behavior and excited-state properties of (coumarin-4- yl)methyl derivatives. 1. Photocleavage of (7-methoxycoumarin-4-yl)methyl- caged acids with fluorescence enhancement. *J Org Chem*. 1999;64(25):9109-9117.
12. Schmidt R, Geissler D, Hagen V, Bendig J. Mechanism of photocleavage of (coumarin-4-yl)methyl esters. In: *Journal of Physical Chemistry A*. Vol 111. American Chemical Society; 2007:5768-5774.
13. Eckardt T, Hagen V, Schade B, Schmidt R, Schweitzer C, Bendig J. Deactivation behavior and excited-state properties of (coumarin-4-yl)methyl derivatives. 2. Photocleavage of selected (coumarin-4-yl)methyl-caged adenosine cyclic 3′,5′-

monophosphates with fluorescence enhancement. *J Org Chem*. 2002;67(3):703-710.

14. Bassolino G, Nançoz C, Thiel Z, Bois E, Vauthey E, Rivera-Fuentes P. Photolabile coumarins with improved efficiency through azetidinyl substitution. *Chem Sci*. 2018;9(2):387-391.
15. Herzig LM, Elamri I, Schwalbe H, Wachtveitl J. Light-induced antibiotic release from a coumarin-caged compound on the ultrafast timescale. *Phys Chem Chem Phys*. 2017;19(22):14835-14844.
16. Hagen V, Dekowski B, Kotzur N, et al. {7-[Bis(carboxymethyl)amino]coumarin-4-yl}methoxycarbonyl Derivatives for Photorelease of Carboxylic Acids, Alcohols/Phenols, Thioalcohols/Thiophenols, and Amines. *Chem - A Eur J*. 2008;14(5):1621-1627.
17. Klausen M, Dubois V, Clermont G, Tonnelé C, Castet F, Blanchard-Desce M. Dual-wavelength efficient two-photon photorelease of glycine by π-extended dipolar coumarins. *Chem Sci*. 2019;10(15):4209-4219.
18. Givens RS, Rubina M, Wirz J. Applications of p-hydroxyphenacyl (pHP) and coumarin-4-ylmethyl photoremovable protecting groups. *Photochem Photobiol Sci*. 2012;11(3):472-488.
19. Olson JP, Kwon HB, Takasaki KT, et al. Optically selective two-photon uncaging of glutamate at 900 nm. *J Am Chem Soc*. 2013;135(16):5954-5957.
20. Sivakumar G. Colchicine Semisynthetics: Chemotherapeutics for Cancer? *Curr Med Chem*. 2013;20(7):892-898.
21. Finkelstein Y, Aks SE, Hutson JR, et al. Colchicine poisoning: The dark side of an ancient drug. *Clin Toxicol*. 2010;48(5):407-414.
22. Nery ALP, Quina FH, Moreira PF, et al. Does the Photochemical Conversion of Colchicine into Lumicolchicines Involve Triplet Transients? A Solvent Dependence Study. *Photochem Photobiol*. 2007;73(3):213-218.
23. Gustavsson T, Cassara L, Gulbinas V, et al. Femtosecond

spectroscopic study of relaxation processes of three amino-substituted coumarin dyes in methanol and dimethyl sulfoxide. *J Phys Chem A*. 1998;102(23):4229-4245.

24. Cong L, Yin H, Shi Y, Jin M, Ding D. Different mechanisms of ultrafast excited state deactivation of coumarin 500 in dioxane and methanol solvents: Experimental and theoretical study. *RSC Adv*. 2015;5(2):1205-1212.
25. Bussotti L, Cacelli I, D'Auria M, et al. Photochemical Isomerization of Colchicine and Thiocolchicine. *J Phys Chem A*. 2003;107(43):9079-9085.
26. Dempster DN, Morrow T, Quinn MF. Extinction coefficients for triplet-triplet absorption in ethanol solutions of anthracene, naphthalene, 2,5-diphenyloxazole, 7-diethylamino- 4-methyl coumarin and 4-methyl-7-amino-carbostyril. *J Photochem*. 1973;2(5):329-341.
27. Gangopadhyay M, Singh T, Behara KK, Karwa S, Ghosh SK, Singh NDP. Coumarin-containing-star-shaped 4-arm-polyethylene glycol: targeted fluorescent organic nanoparticles for dual treatment of photodynamic therapy and chemotherapy †. *Cite this Photochem Photobiol Sci*. 2015;14:1329.
28. Fournier L, Gauron C, Xu L, et al. A blue-absorbing photolabile protecting group for in vivo chromatically orthogonal photoactivation. *ACS Chem Biol*. 2013;8(7):1528-1536.
29. Bosca F, Tormos R. Behavior of drug excited states within macromolecules: Binding of colchicine and derivatives to albumin. *J Phys Chem B*. 2013;117(25):7528-7534.
30. Rehm D, Weller A. Kinetics of Fluorescence Quenching by Electron and H-Atom Transfer. *Isr J Chem*. 1970;8(2):259-271.
31. Jones G, Griffin S, Choi C yoo, Bergmark WR. Electron Donor-Acceptor Quenching and Photoinduced Electron Transfer for Coumarin Dyes. *J Org Chem*. 1984;49(15):2705-2708.
32. Bodoki E, Laschi S, Palchetti I, Săndulescu R, Mascini M. Electrochemical behavior of colchicine using graphite-based

screen-printed electrodes. *Talanta*. 2008;76(2):288-294.

33. Mortensen J, Heinze J. The Electrochemical Reduction of Benzene—First Direct Determination of the Reduction Potential. *Angew Chemie Int Ed English*. 1984;23(1):84-85.
34. Merkel PB, Luo P, Dinnocenzo JP, Farid S. Accurate oxidation potentials of benzene and biphenyl derivatives via electron-transfer equilibria and transient kinetics. *J Org Chem*. 2009;74(15):5163-5173.
35. Bodoki E, Laschi S, Palchetti I, Săndulescu R, Mascini M. Electrochemical behavior of colchicine using graphite-based screen-printed electrodes. *Talanta*. 2008;76(2):288-294.
36. R.V. Bensansson EJL and TGT. *Flash Photolysis and Pulse Radiolysis*. Elsevier; 1983.
37. Noguchi M, Skwarczynski M, Prakash H, et al. Development of novel water-soluble photocleavable protective group and its application for design of photoresponsive paclitaxel prodrugs. *Bioorganic Med Chem*. 2008;16(10):5389-5397.
38. Bagnato JD, Eilers AL, Horton RA, Grissom CB. Synthesis and characterization of a cobalamin-colchicine conjugate as a novel tumor-targeted cytotoxin. *J Org Chem*. 2004;69(26):8987-8996.
39. Crielaard BJ, Van Der Wal S, Le HT, et al. Liposomes as carriers for colchicine-derived prodrugs: Vascular disrupting nanomedicines with tailorable drug release kinetics. In: *European Journal of Pharmaceutical Sciences*. Vol 45. Elsevier; 2012:429-435.
40. Murov SL, Carmichael I, Hug GL. *Handbook of Photochemistry, 2nd Ed.*; 1993.

Chapter 7: Developing biocompatible upconversion nanosystems for photocontrolled drug delivery using albumin complexed with coumarin derivatives

7.1. Introduction

Cancer nanotherapeutics are rapidly progressing and are being implemented to solve the major limitations of conventional drug delivery systems such as toxic side effects, nonspecific biodistribution and targeting, lack of water solubility or poor oral bioavailability. The fast growth of novel nanomaterials has produced the development of nanocarrier systems, including liposomes, proteins, polymeric nanoparticles, dendrimers, silica and iron oxide nanoparticles and my other types, for targeted drug delivery.[1] In this context, phototrigger-controlled drug-release nanosystems have also been developed as promising tools for controlled-release drug delivery in tumor therapy.[1–4] In general, this type of nanomaterials are composed of a biocompatible nanocarrier with the drug caged and a phototrigger (usually, coumarin or 2-nitrobenzyl derivatives), which can be manipulated by ultraviolet (UV) light to obtain the desired drug-release patterns.[2–4] Nevertheless, this light has low penetration depth in living tissues, which is a limiting factor for applications in early diagnosis and cancer therapy.

Other electromagnetic radiation such as near infrared (NIR) light can achieve high penetration in the body, however it cannot be directly used in phototrigger-controlled drug–release because most of the photoreactions require high energy UV or visible (Vis) light to occur. Fascinatingly, lanthanide-doped upconversion nanoparticles (UCNP) have the capability of converting NIR light into UV and Vis emissions in an anti-Stokes process and are excellent functional agents as the core

scaffolds of core-shell materials.[5] These properties confer UCNP a significant potential for biomedical applications.[6–9]In the past few years, a widely applied approach to preparing phototrigger-controlled drug-release nanosystems for NIR-triggered anticancer drug delivery is the combination of UCNP cores with different types of shells such as hydrogels, block copolymer micelles, and mesoporous silica nanoparticles, where phototriggers bearing excitable chromophores in the UV-Vis range and drugs are loaded.[10–15] The underlying fundamental principle is that controlled NIR light excitation of UCNP generates UV-Vis emission inside the nanosystem which is absorbed by phototrigger to bring about the photochemical reaction responsible for drug release.

Two strategies have been employed to design the nanosystems: a) a drug is caged into an external shell formed by long-chain organic molecules with ionic properties or by different types of polymers which contain a phototrigger within their backbone. Exposure to UV or visible light causes chain scission and drug release. [11–14] b) A prodrug formed by a phototrigger covalently attached to the drug is loaded inside hollow inert cavities of a silica shell by physical adsorption. In this case, excitation of the phototrigger produce photolysis of the prodrug with consequent drug release.[15] Both types of nanosystems have shown to be effective for drug delivery, however, the biocompatibility of silica nanoparticles and some polymers have recently been questioned.[16–19]

With this background, we are interested in developing a new phototrigger-controlled drug-release nanosystem much more

biocompatible. Human serum albumin (HSA) was selected as the shell of the new nanomaterial because this protein is an ideal platform for effective delivery of drugs, mostly attributed to its unique features of low toxicity, minimized inflammatory stimulation and biodegradability.[20,21] Moreover, HSA nanoparticles are excellent drug carrier systems and offer the possibility of surface modification with ligands as folic acid for the selective targeting of drugs into tumor cells.[22] The most convenient way to connect an organic compound such as a prodrug to albumin is probably introducing the molecule into the cavities of the albumin because, at the same time that the association is produced, the protein acts as protecting prodrug from enzymatic processes. For this purpose, it is mandatory that the prodrug, a phototrigger chromophore covalently linked to a pharmaceutical compound, has high binding affinity to HSA. Besides, at the same time, it is convenient that the drug has the inverse property to favor its release to the medium when the prodrug complexed to HSA is photoactivated.

7.2. Results and discussion

Looking for excellent phototriggers with high binding affinity for HSA in the literature it was found that most coumarin derivatives show high association constants to HSA ($K_a > 10^4$ M^{-1}).[23] In fact, warfarin, a compound of this family, is usually employed as reference compound for albumin binding Site I and has a K_a of 5.4×10^5 M^{-1}.[24] In this context, hydroxycoumarin COU (see structure in Scheme 7.1) was selected as phototrigger.

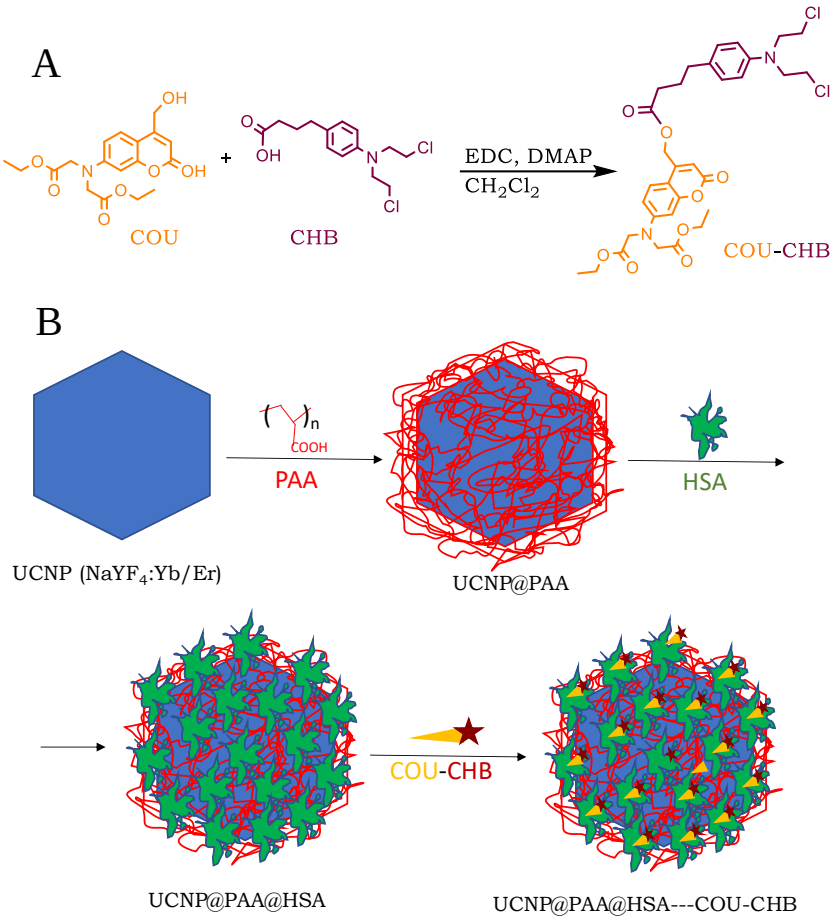

Scheme 7.1. A) Synthesis of prodrug (**COU-CHB**). B) Synthesis of the nanostructure UCNP(NaYF4 : Yb/Er)@PAA@HSA containing an UCNP core and a shell of HSA covalently linked to PAA). C) Photoactivatable drug-release nanosystem formed by loading UCNP@PAA@HSA with **COU-CHB** prodrug.

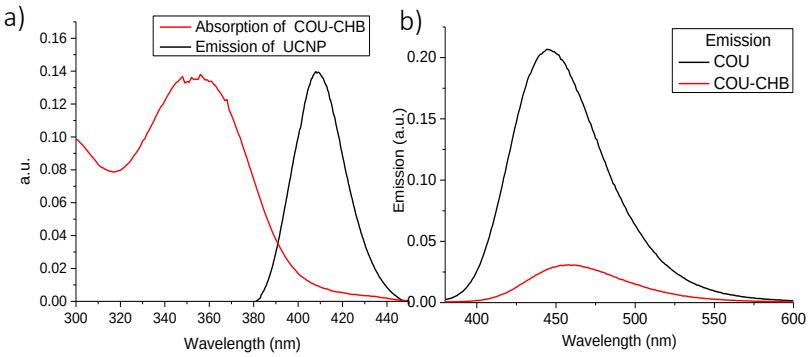

Figure 7.1. a) Absorption spectrum of **COU-CHB** prodrug in methanol/H_2O (3/1) and emission spectrum of the peak at ca. 410 nm of UCNP ($NaYF_4$: Yb/Er 18/2) using 980 nm excitation wavelength. b) Emission spectra of **COU** and **COU-CHB** in methanol/H_2O (3/1) at the excitation wavelength of 350 nm.

The pharmacologically active agent chosen to complete the prodrug was chlorambucil (CHB) because this anticancer compound has a very low binding affinity to HSA ($K_a < 10^3\ M^{-1}$),[25] Moreover, the generation of a photolabile covalent bond between the carboxylic group of CHB and the 4-hydroxymethyl substituent of **COU** is feasible. Thereby, synthesis of the conjugated coumarin chlorambucil prodrug (**COU-CHB**, Scheme 7.1A) was performed by esterification of 7-[bis(ethoxycarbonylmethyl)lamino]-4-(hydroxymethyl)coumarin (**COU**) with CHB using N,N´-dicyclohexylcarbodiimide coupling reagent to yield 60 %. Its structure was unambiguously assigned using NMR spectroscopy and UPLC-HRMS (details of the data and the synthetic route to obtain **COU** are described in the experimental section below).

Next, irradiations of the prodrug in methanol/water (1/1) solutions were performed with white lamps emitting in the 380-460 nm range to confirm that this compound can be used as a photoactivatable prodrug

in nanoystems containing UCNP with UV-Vis emissions (see the overlap between the absorption spectrum of prodrug and emission spectrum of UCNP in Figure 7.1a). The result proved that photolysis of **COU-CHB** gave rise to the release of CHB and **COU** (see Scheme 7.2). Experimental details of this reaction are provided in the experimental section.

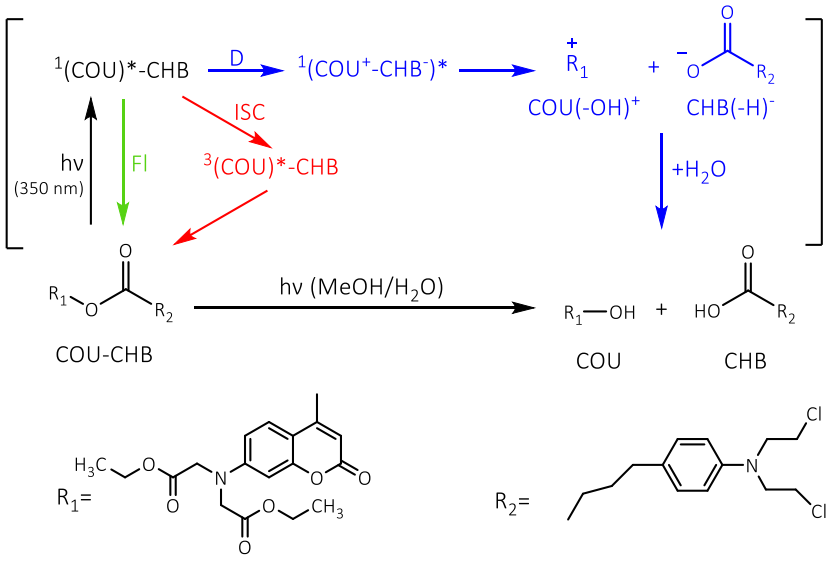

Scheme 7.2. Main pathways of COU-CHB prodrug photolysis.

The photochemical processes involving the heterolytic bond cleavage of **COU-CHB** were evaluated performing steady state and time resolved emission measurements as well as laser flash photolysis experiments using **COU-CHB** and **COU** in buffered H_2O/methanol (1/1) solutions. Notably, the **COU** fluorescence quantum yield (ϕ_F) decreases when it is attached to CHB (see green fluorescence pathway (Fl) in Scheme 7.2). Thus, a ϕ_F of *ca.* 0.57 versus 0.09 were determined for **COU** and **COU-CHB** respectively (see emission spectra in Figure 7.1b).

This result and the shortening of the prodrug emission lifetime (τ_F) as compared with that of **COU** (τ_F *ca.* 3.3 ns and 4.8 ns respectively), suggest a prodrug photolysis arising from the coumarin singlet excited state (^{1}(**COU**)*, see the blue pathway D in Scheme 7.2) as previously reported in the literature for closely related compounds.[26]

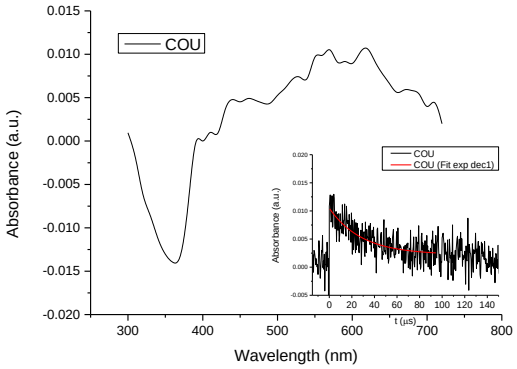

Figure 7.2. Transient absorption spectrum of a methanol/ 1 mM PB (1/1) solution of 3 x 10^{-5} M **COU** under anaerobic conditions (N_2) 1 µs after the laser pulse. Inset: Decay traces at 620 nm and its fit to an exponential 1st order decay.

Further support for the photolytic pathway D was found performing laser flash photolysis experiments with **COU** and **COU-CHB** because the characteristic absorption spectrum of coumarin chromophore triplet excited state (λ_{max} *ca*. 620 nm)[27]was only detected using **COU** (see Figure 7.2; more evidences for this triplet state assignment in the experimental section). The detected traces of the coumarin triplet excited state were very noisy because all 7-aminocoumarins have poor intersystem crossing (ISC) efficiencies.[28] Accordingly, the photolytic pathway D, which only occurs from **COU-CHB**, besides decreasing

fluorescence (Fl) pathway significantly, produces the almost complete suppression of the ISC process (Scheme 7.2). It should be mentioned that the photolysis of this type of coumarin prodrugs needs water to release the drug.[26]

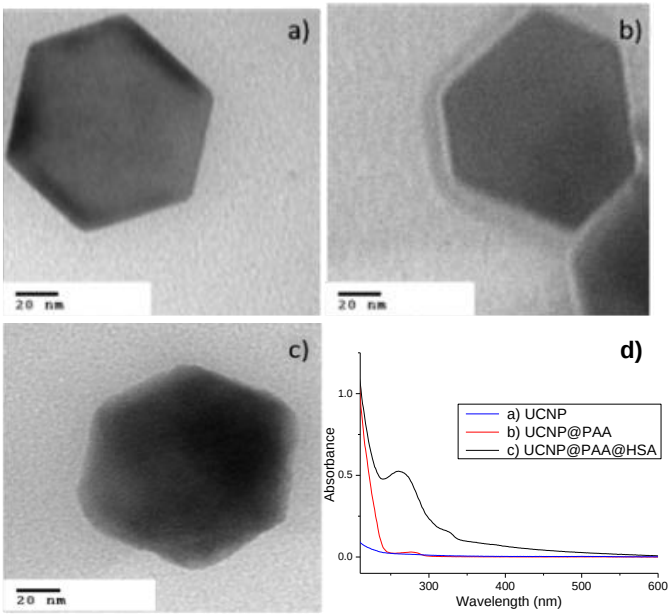

Figure 7.3. TEM of a) UCNP ($NaYF_4$: Yb/Er) b) UCNP@PAA, c) UCNP@PAA@HSA, and d) absorption spectrum of each nanostructure.

The nanocarrier HSA-coated theranostic UCNP (UCNP@PAA@HSA), was synthesized using a methodology described in the literature for a similar UCNP using bovine serum albumin. [29] All the steps to obtain the nanosystem UCNP ($NaYF_4$: Yb/Er) @PAA@HSA are shown in Scheme 7.1B (experimental and some characterization details are provided in experimental section and in Figure 7.7). Summarizing, the initial $NaYF_4$: Yb/Er nanoparticles were synthesized by Ostwald Ripening method (see

structure in Figure 7.3a). The UCNPs showed a size of *ca*. 100 nm and their emission spectra displayed peaks at λ_{max} *ca.* 408, 545 and 660 nm, which is typical when the percentage of lanthanides are 18 % Ytterbium and 2 % of Erbium. An exchange between the non-polar shell of oleic acid of the initial UCNP and polyacrylic acid (PAA) was done to give biocompatibility to the UCNP following literature protocol.[29] Thus, an additional shell 7 ± 3 nm in thickness was observed, pointing to the presence of a PAA layer around each particle (see Figure 7.3b). Moreover, these particles showed an UV absorption attributable to the PAA (Figure 7.3d).

The HSA shell was achieved by amidation of PAA carboxylic acids with primary amino groups present in the protein chain. The specific tendency to accumulate HSA on the surface of $NaYF_4$: Yb/Er @PAA can be observed comparing Figures 7.3b and 7.3c. The presence of the protein on $NaYF_4$: Yb/Er @PAA nanoparticle was also confirmed using UV-Vis spectrometry (Figure 7.3d). Thus, the UCNP@PAA@HSA nanosystem showed a new peak at *ca*. 280 nm, which is attributable to the HSA absorption. In this context, the emission properties of UCNP@PAA and UCNP@PAA@HSA resulted to be similar to that

observed for the primary UCNP (see their emission spectra in Figure 7.6 of the experimental section).

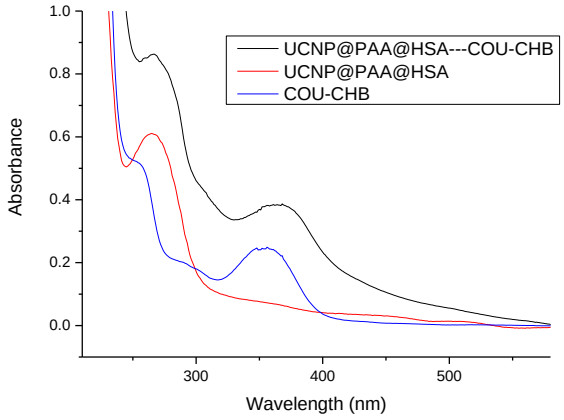

Figure 7.4. Absorption spectra of UCNP@PAA@HSA and COU-CHB loaded to the albumin nanosystem and alone.

The next step to prepare the final nanosystem (UCNP@PAA@HSA---COU-CHB) was to determine the association constant (K_a) between albumin and the **COU-CHB** prodrug. Hence, this data was determined using the emission quenching of the tryptophan unit (Trp) of HSA by the presence of **COU-CHB** (experimental details are included in the experimental section). Interestingly, a K_a value of *ca*. 1.5 10^5 M^{-1} was obtained (see Figure 7.7. for more details). This value predicts an efficient binding between the prodrug and the HSA of our nanosystem. Thereby, taking into account this K_a, **COU-CHB** was loaded into the albumin sites of UPNP@PAA@HSA in more than 95 % using 2 x 10^{-5} M buffered aqueous mixtures of the albumin linked to the nanosystem structure and 10^{-5} M of the prodrug (see Scheme 7.1 and Figure 7.4).

Details of the **COU-CHB** loading are included in experimental section. Afterwards, the UPNP@PAA@HSA---COU-CHB nanosystem was tested in aqueous media using a 980 nm NIR laser 1 W/cm^2 continuous-wave. The overall process of CHB release is shown in Scheme 7.3.

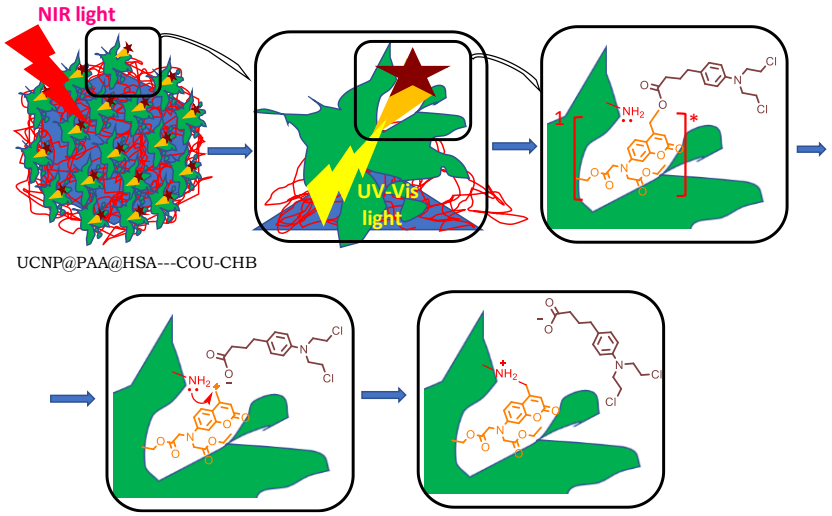

Scheme 7.3. Chlorambucil release from UPNP@PAA@HSA---COU-CHB nanosystem photoinduced by NIR light.

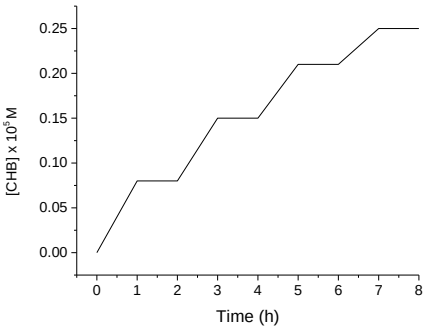

Figure 7.5. The time course of CHB release from UCNP@PAA@HSA---COU-CHB nanosystem using NIR light at 980 nm (1 W cm^{-2}) and dark conditions. ''ON'' indicates the beginning of light irradiation; ''OFF'' indicates the end of light irradiation.

Near infrared upconversion excitation triggers UVA-Vis emission from the nanoparticles which in turn is converted to **COU** excitation in the prodrug. The subsequent coumarin singlet excited state generation produces the CHB releasing. Figure 7.5 shows the partial progress for the release of CHB from UPNP@PAA@HSA---COU-CHB nanosystem using NIR light at 980 nm (1 W cm^{-2}) and under dark conditions (more details are given in experimental section). Interestingly, delivery of **COU** or another coumarin derivative was not detected. The lack of complexation between **COU** and HSA determined using a similar emission quenching study than that performed for **COU-CHB** indicates that the K_a of **COU**---HSA must be lower than 10^4 M^{-1}. A nucleophilic attack of some free amino group of the albumin to **COU** would be in accordance to the **COU-CHB** fragmentation results (see mechanism in Scheme 7.3). Thereby, a clean drug release is produced in the NIR triggered process.

7.3. Conclusions

In summary, we have developed an upconversion-based phototriggered drug-release device using HSA as biocompatible shell. The anticancer drug chlorambucil linked to an hydroxycoumarin derivative phototrigger was loaded into nanocages of UCNP@PAA@HSA through the generation of albumin-prodrug complexes. Irradiation of this nanosystem at 980 nm produces the controlled cleavage of the coumarin phototrigger releasing only the drug into the bulk solution. The binding affinity of chemicals to HSA is a novel and easy method to prepare NIR light-responsive nanodrug

delivery systems with very high biocompatibility. This approach could be extended to load other anticancer drugs such as doxorubicin in UCNP@PAA@HSA and more importantly, it offers the possibility to rescue colchicine and other antineoplastic chemicals that were discarded for cancer treatments due to their high toxicities.

7.4. Experimental section

7.4.1. Materials

Selenium dioxide, ethyl bromoacetate, chlorambucil, 4-(dimethylamino)pyridine, Yttrium (III) chloride (YCl_3), Ytterbium (III) chloride ($YbCl_3$), Erbium (III) chloride ($ErCl_3$), oleic acid (OA), 1-octadecene (ODE), ammonium fluoride (NH_4F), sodium hydroxide (NaOH), polyacrylic acid (PAA) and human serum albumin fatty acid free (HSA) were commercial products obtained from Sigma-Aldrich Chemical Company. 7-Amino-4-methylcoumarin was a commercial product from Fluorochem. Sodium phosphate buffer (PB) and sodium bicarbonate buffer were prepared from reagent-grade products using milli-Q water; the pH of the solutions was measured through a glass electrode and adjusted with NaOH to pH *ca*. 7.4. Other chemicals were of reagent grade and used as received. 0.45 µm diameter PTFE filters were bought from Labbox.

7.4.2. Experimental conditions for absorption and emission measurements

Ultraviolet spectra were recorded on a UV/Vis scanning spectrophotometer (Cary 50). Fluorescence emission spectra were recorded on a Photon Technology International (PTI) LPS-220B fluorimeter. Lifetimes were measured with a time resolved spectrometer (TimeMaster fluorescence lifetime spectrometer TM-2/2003) from PTI by means of the stroboscopic technique, which is a variation of the boxcar technique. A hydrogen/nitrogen flashlamp (1.8 ns pulse width) was used as excitation source. The kinetic traces were fitted with monoexponential decay functions. Measurements were made under aerated conditions at room temperature (25 °C) in cuvettes of 1 cm path length. The excitation wavelength used to register the fluorescence lifetimes was 450 nm. The fluorescence quantum yield of quinine bisulphate in 1 N H_2SO_4 (ϕ_F = 0.546) was used as standard.

7.4.3. Experimental and results of laser flash photolysis experiments

A pulsed Nd:YAG laser was used for the excitation at 355 nm. The single pulses were ~10 ns duration and the energy was from 10 to 1 mJ/pulse. A pulsed xenon lamp was employed as detecting light source. The laser flash photolysis apparatus consisted of the pulsed laser, the Xe lamp, a monochromator and a photomultiplier made up of a tube, housing and power supply. The output signal from the oscilloscope was transferred to a personal computer.

The studies were performed with 3 x 10^{-5} M **COU** and **COU-CHB** in buffered solutions of 1 mM PB/methanol (1/1). The experiments were registered under aerobic and anaerobic conditions.

Additional results. Absorption spectrum obtained for **COU** under anaerobic conditions corresponds, in accordance to the literature,[27] to the triplet excited state of the coumarin chromophore. A lifetime of 28.7 μs was determined under our experimental conditions. Moreover, as expected for a triplet excited state species, the intermediate was efficiently quenched by the presence of oxygen. By contrast, **COU-CHB** did not show any signal using the same experimental conditions.

7.4.4. Experimental for drug release studies

The release of CHB from prodrug **COU-CHB** associated or not to the protein shell of UCNP@PAA@HSA was studied by HPLC. The equipment used was the Agilent 1100 series LC model with a quaternary pump G1311A and photodiode array detector G1315B and wavelength detection from 200 nm to 600 nm equipped with a Mediterranean Sea C18 (25 x 0.46 cm, particle size of 5μm). The mobile phase was acetonitrile/water/Trifluoroacetic acid 40/59.9/0.1 at a flow rate of 1.5 mL/min flow.

7.4.4.1. Procedure for prodrug COU-CHB

A solution of 1mM PB/MeOH (1/1) containing 10^{-5} M of the prodrug was irradiated during 60 min in a photoreactor using four white lamps emitting in the 380-460 nm range with a maximum at 420 nm and

Gaussian distribution. Samples were taken at 30 and 60 min and analyzed by HPLC.

7.4.4.2. Procedure for nanosystem UCNP@PAA@HSA···COU-CHB

The solution containing the nanosystem (conditions in the above section) was irradiated in a quartz cuvette of 1 cm path length with an infrared laser RLTMDL-980 1-2000 mW (PSU-III-LED) at λ_{max} = 980 nm ± 5 nm and 1000 mW power during 240 min with continuous stirring. Dark samples and irradiated samples were taken at 0 min, 60, 120, 180 and 240 min and were analyzed by HPLC after being centrifuged.

7.4.5. Synthetic route and characterization of prodrug COU-CHB

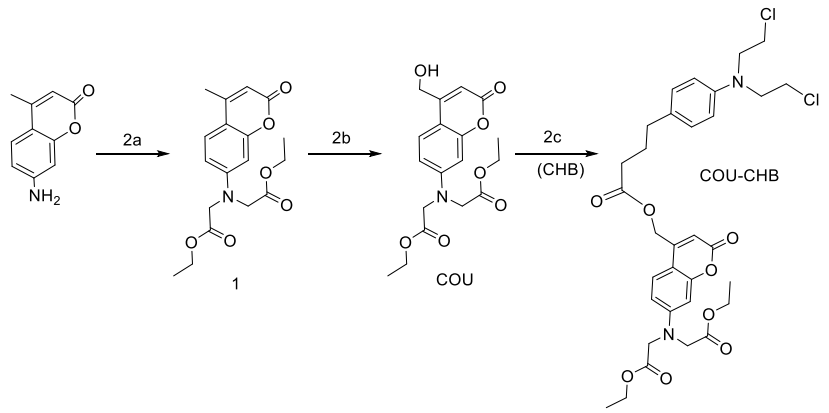

Scheme 7.1. Synthesis of prodrug **COU-CHB** from 7-Amino-4-methylcoumarin.

7-[bis(ethoxycarbonylmethyl)lamino]-4-methylcoumarin (**1**). It was synthesized using the methodology described in the literature.[30] 7-Amino-4-methylcoumarin (34.25 mmol, 6 g), NaI (34.25 mmol, 5.14 g), diisipropylethylamine (172.61 mmol, 30 mL), and ethyl bromoacetate (0.35 mol, 39 mL) in 165 mL of dry CH_3CN were refluxed for 4 days

under nitrogen atmosphere. The mixture was cooled to room temperature, filtered and the solvent was removed under reduced pressure. The residue was dissolved in EtOAc, washed with water and brine, dried over $MgSO_4$, and concentrated under vacuum. The resulting oil was purified by silica-gel column chromatography (EtOAc/ Cyclohexane 1:1) to yield 1 (7.1 g, 20.55 mmol, 60%).

^{1}H NMR (300 MHz, $CDCl_3$) δ 7.42 (d, *J* = 8.8 Hz, 1H), 6.55 (dd, *J* = 8.8, 2.6 Hz, 1H), 6.47 (d, *J* = 2.6 Hz, 1H), 6.03 (d, *J* = 1.1 Hz, 1H), 4.20 (q, *J* = 7.0 Hz, 4H), 4.10 (s, 4H), 2.34 (d, *J* = 1.1 Hz, 3H), 1.28 (q, *J* = 7.0 Hz, 6H). MH^+ calculated for **1** ($C_{18}H_{22}NO_6$): 348.1448, found: 348.1455.

7-[bis(ethoxycarbonylmethyl)lamino]-4-(hydroxymethyl)coumarin (**COU**). Selenium dioxide (19.81 mmol, 2.21 g) and compound **1** (13.36 mmol, 5 g) in 138 mL *p*-xylene were refluxed with vigorous stirring under a nitrogen atmosphere. After 24 h, the mixture was filtered and concentrated under reduced pressure. The dark brown residual oil was dissolved in ethanol (100 mL), then sodium borohydride (6.76 mmol, 252.67 mg) was added, and the solution was stirred for 1 h at room temperature. Thereafter, the suspension was carefully hydrolyzed with 1 M (6.7 mL), diluted with H_2O, and partially concentrated under reduced pressure to remove EtOH. The resulting mixture was extracted with EtOAc. The organic phase was washed with H_2O and brine, dried over $MgSO_4$, and concentrated under vacuum. The resulting oil was purified by silica-gel column chromatography (EtOAc/Cyclohexane 1:1) to yield **COU** (2.66 g, 7.3 mmol, 55 %).

^{1}H NMR (300 MHz, $CDCl_3$) δ 7.23 (d, *J* = 8.7 Hz, 1H), 6.47 (dd, *J* = 8.7, 2.6 Hz, 1H), 6.43 (d, *J* = 2.6 Hz 1H), 6.28 (s, 1H), 4.68 (s, 2H), 4.25 (q, *J* = 7.7 Hz, 4H), 4.10 (s, 4H), 1.27 (t, *J* = 7.4 Hz, 6H). MH^+ calculated for COU ($C_{18}H_{22}NO_7$): 364.1397, found: 364.1405.

COU-CHB. Under dark conditions, a mixture of **COU** (379 mg, 1.09 mmol), chlorambucil (400 mg, 1.31 mmol), EDC (146 mg, 0.76 mmol), and DMAP (26.9 mg, 0.022 mmol) was dissolved in 135 mL anhydrous CH_2Cl_2 under nitrogen atmosphere. After stirring at room temperature for 4 h, the solvent was removed under vacuum. The obtained crude product was purified by preparative TLC (Cyclohexane: ethyl acetate = 1.2: 0.8) to yield **COU-CHL** (424 mg, 0.65 mmol, 60 %). MH^+ calculated for **COU-CHB** ($C_{32}H_{39}N_2O_8Cl_2$): 649.2083, found: 649.2101.

^{1}H NMR (300 MHz, $CDCl_3$) δ 7.33 (d, *J* = 8.8 Hz, 1H), 7.05 (d, *J* = 8.8 Hz, 1H), 6.62 (d, *J* = 8.7 Hz, 1H), 6.54 (dd, *J* = 8.9, 2.6 Hz, 1H), 6.49 (d, *J* = 2.6 Hz, 1H), 5.19 (d, *J* = 1.4 Hz, 1H), 4.30 – 4.11 (m, 5H), 3.73 – 3.56 (m, 5H), 2.58 (t, *J* = 7.4 Hz, 1H), 2.44 (t, *J* = 7.5 Hz, 1H), 1.96 (p, *J* = 7.5 Hz, 1H), 1.29 (t, *J* = 7.1 Hz, 4H).

^{13}C NMR (75 MHz, $CDCl_3$) δ 172.71, 169.58, 161.23, 155.62, 151.06, 149.28, 144.47, 130.13, 129.70, 124.57, 112.24, 109.33, 108.56 108.43, 99.61, 61.62, 61.02, 53.59, 53.39, 40.56, 33.90, 33.33, 26.53, 14.21.

7.4.6. Synthetic route and additional results for obtaining $NaYF_4$: Yb/Er (18%, 2%) @PAA@HSA···COU-CHB nanosystem

7.4.6.1. Synthesis of $NaYF_4$: Yb/ Er(18%, 2%)[31]

The salts $YCl_3 \cdot H_2O$ (0.8 mmol), $YbCl_3 \cdot H_2O$ (0.18 mmol) and $ErCl_3 \cdot H_2O$ (0.02 mmol) were mixed with 12 mL of oleic acid (OA) and 15 mL of octadecene (ODE) in 100 mL 3 necked flask. The solution was heated to 160 ^{0}C to form a homogeneous solution and then cooled down to room temperature under nitrogen flow. Afterwards, 10 mL methanol solution containing NH_4F (4 mmol) and NaOH (2.5 mmol) was added, and the solution stirred for 30 minutes. Vacuum-nitrogen cycles were done to help methanol evaporation. Then, the solution was heated to 305 °C, maintained at this temperature for 2 hours under Ar atmosphere, and then cooled down to room temperature. The resultant nanocrystals were precipitated by the addition of ethanol, washed with ethanol-water (1:1 v/v) three times, collected by centrifugation and finally resuspended in cyclohexane. Characterization of the nanoparticles was performed using the Transmission electron microscopy JEOL JEM—1010 and CUBIX XRD DY0822 X-ray radioactive system.

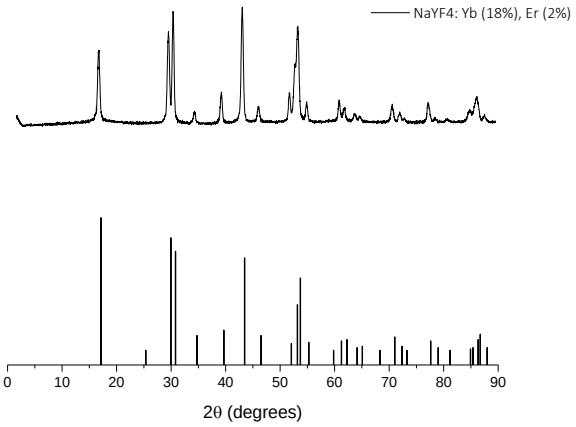

Figure 7.6. XRD spectra of $NaYF_4$: 18% Yb,2%Er and standard JCPDS PDF number 16-0334

7.4.6.2. Surface modification of $NaYF_4$: Yb/Er (18%, 2%) with polyacrylic acid (PAA)[29]

To obtain hydrophilic nanoparticles, the prepared UCNP (50 mg) were dissolved in 2.5 mL of toluene. In a 100 mL three-necked flask, 150 mg of polyacrylic acid (PAA) was dissolved in 15 mL of diethylene glycol (DEG) and heated to 110 °C to form homogeneous solution. A solution of toluene with nanoparticles was slowly added to the mixture and left 1 hour with vigorous stirring under nitrogen atmosphere. Then the solution was heated to 240 °C for 1.5 hours and afterwards, cooled down to room temperature. Nanoparticles were precipitated with ethanol, centrifugated at 4000 rpm for 1 hour, and then washed 3 times with ethanol/water (1:1) at 4000 rpm 1 hour each. Finally, $NaYF_4$: Yb/Er (18%, 2%) @PAA were dispersed in deionized water and preserved at 4 °C for future use.

7.4.6.3. Functionalization of $NaYF_4$: Yb/Er (18%, 2%)@PAA with Human Serum Albumin (HSA)[29]

100 mg of fatty acid free HSA and 5 mg of N-(3-Dimethylaminopropyl)-N′-ethylcarbodiimide hydrochloride were dissolved in 5 mL aqueous solution of $NaYF_4$: Yb/Er (18%, 2%)@PAA of 2 mg/mL. After 2 hours of vigorous stirring, 5 mg of EDC were added. The reaction mixture was maintained at room temperature 6 hours. Nanoparticles were precipitated by centrifugation with water at 6000 rpm for 1 hour. Finally, nanocrystals were dispersed in water and maintained at 4 °C.

7.4.6.4. Preparation of nanosystem $NaYF_4$: Yb/Er (18%, 2%) @PAA@HSA···COU-CHB

To 3 mL of an aqueous solution of $NaYF_4$: Yb/Er (18%, 2%)@PAA@HSA (2 mg/mL of nanoparticles with a HSA concentration of ca. 2×10^{-5} M) 3 µL of 10^{-2} M prodrug **COU-CHB** in DMSO were added to load the prodrug int the nanoparticles. The mixture was kept under continuous stirring in the dark for 10 minutes. Afterwards, sample was centrifuged at 6000 rpm over 30 minutes and washed twice with distilled water. Finally, an UV-Vis spectrum of precipitated in water was done to confirm the loading of the prodrug compared to $NaYF_4$: Yb/Er (18%, 2%)@PAA@HSA.

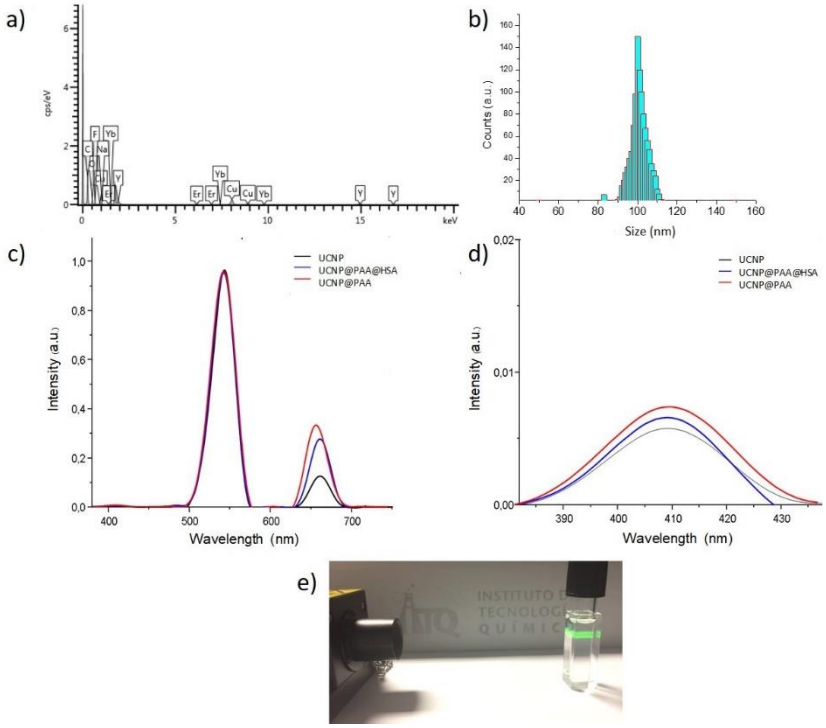

Figure 7.6. a) EDS-TEM of UCNP. b) Histogram of distribution size of UCNP. c) Emission spectrum of UCNP, $NaYF_4$: Yb/Er (18%, 2%)@PAA and $NaYF_4$: Yb/Er (18%, 2%)@PAA@HSA at the excitation wavelength of 980 nm. d) Amplification of the emission band centered at 410 nm. e) Photography of emission spectrum of UCNP.

7.4.6.5. Analysis of complexation between prodrug COU or COU-CHB and HSA

The study was performed using free fatty acid HSA (10^{-4}M) and different amounts of **COU** or prodrug **COU-CHL**. The sample was analyzed by UV-Vis spectrometry and fluorescence spectroscopy after 5 min stirring. The association constants were determined using the

HSA fluorescence band (λ_{max} ≈ 344 nm) after excitation at 295 nm as described in the literature.[32] The fluorescence quenching of this band was monitored adding increasing amounts of **COU** or prodrug **COU-CHL** (from 2 x 10^{-7} M to 2 x 10^{-6} M). Before analyzing the data, inner filter effect correction (IFE) was applied because both compounds absorb light at the excitation and emission wavelengths. The IFE correction was applied using Equation 7.1:

$$F_{corr} = F_{obs} \times 10^{(Aex + Aem)/2} \quad \text{Eq. 7.1}$$

Where F_{corr} and F_{obs} are the corrected and the observed fluorescence respectively, and A_{ex} and A_{em} are the absorbance values at the excitation and emission wavelengths, respectively.

Thus, the corrected data were analyzed using the Equation 7.1 to determine the association constant (K_a) between albumin and COU or the prodrug.

$$F_0/F = 1 + K_{sv} \cdot [Q] \quad \text{Eq. 7.2}$$

F_0 and F are the fluorescence intensities in the absence and presence of the quencher respectively, [Q] is the quencher concentration and K_{sv} is the Stern-Volmer quenching constant, that is a good approximation of K_a.[32]

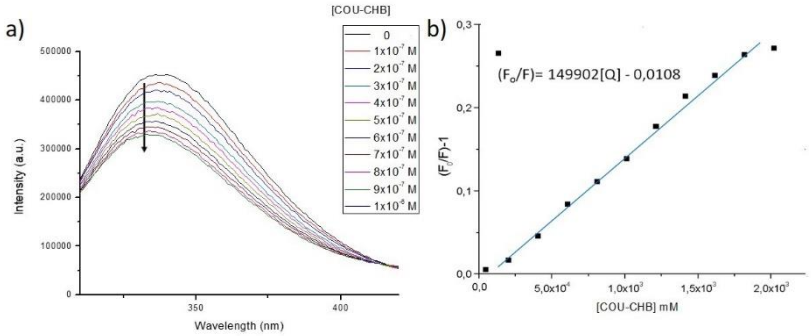

Figure 7.7. a) Emission of HSA at different prodrug concentrations. b) Plot of $(F_0/F)-1$ vs prodrug concentration to determine K_a.

7.5. NMR Spectra

^{1}H COU

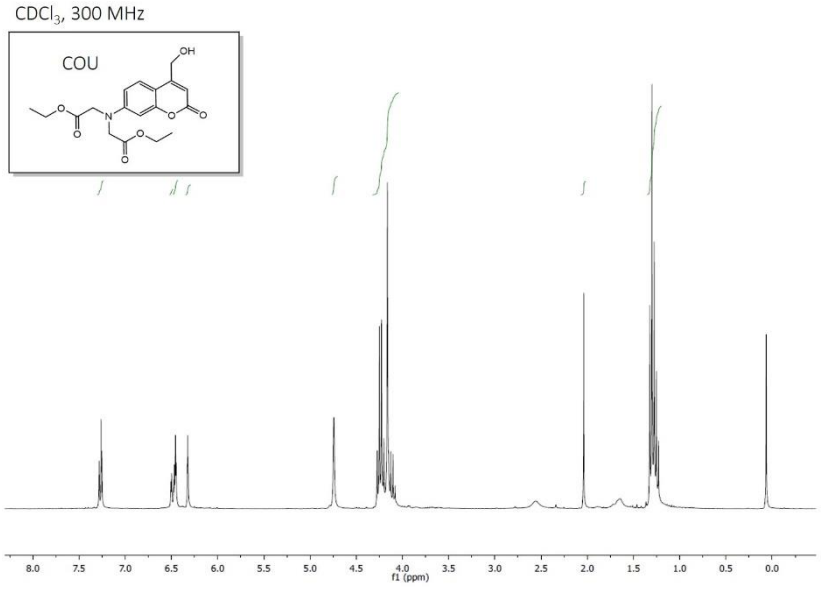

^{1}H COU-CHB

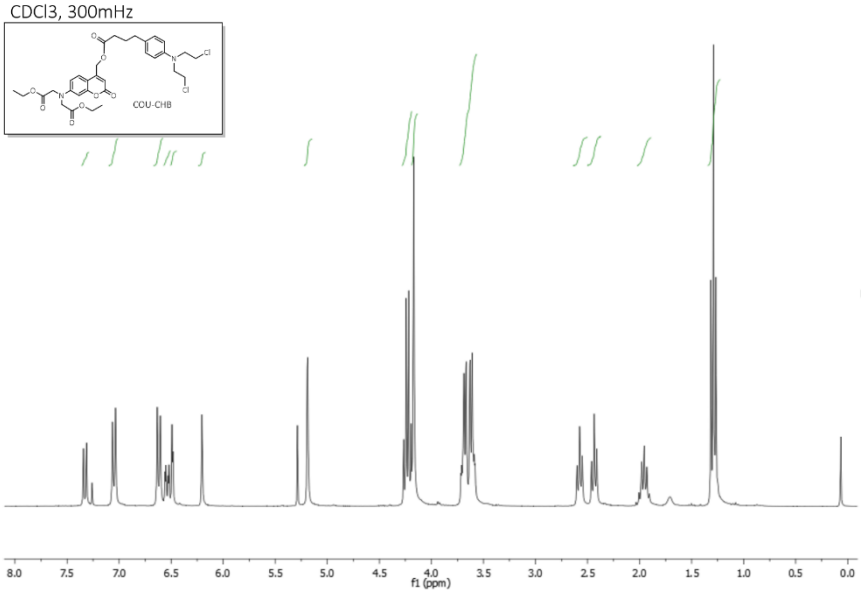

^{13}C COU-CHB

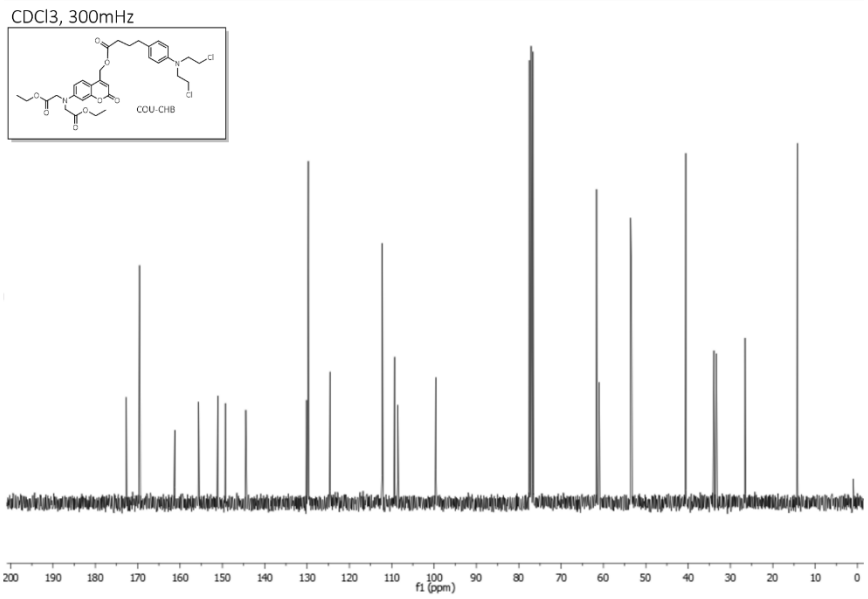

7.6. References

1. Wong PT, Choi SK. Mechanisms of Drug Release in Nanotherapeutic Delivery Systems. *Chem Rev*. 2015;115(9):3388-3432.
2. Klán P, Šolomek T, Bochet CG, et al. Photoremovable protecting groups in chemistry and biology: Reaction mechanisms and efficacy. *Chem Rev*. 2013;113(1):119-191.
3. Li X, Mu J, Liu F, et al. Human transport protein carrier for controlled photoactivation of antitumor prodrug and real-time intracellular tumor imaging. *Bioconjug Chem*. 2015;26(5):955-961.
4. Löw K, Wacker M, Wagner S, Langer K, Von Briesen H. Targeted human serum albumin nanoparticles for specific uptake in EGFR-Expressing colon carcinoma cells. *Nanomedicine Nanotechnology, Biol Med*. 2011;7(4):454-463.
5. Chen G, Qiu H, Prasad PN, Chen X. Upconversion nanoparticles: Design, nanochemistry, and applications in Theranostics. *Chem Rev*. 2014;114(10):5161-5214.
6. Chen S, Weitemier AZ, Zeng X, et al. Near-infrared deep brain stimulation via upconversion nanoparticle–mediated optogenetics. *Science (80-)*. 2018;359(6376):679-684.
7. Wu S, Butt HJ. Near-Infrared-Sensitive Materials Based on Upconverting Nanoparticles. *Adv Mater*. 2016;28(6):1208-1226.
8. Cho HJ, Chung M, Shim MS. Engineered photo-responsive materials for near-infrared-triggered drug delivery. *J Ind Eng Chem*. 2015;31:15-25.
9. Smith AM, Mancini MC, Nie S. Bioimaging: Second window for in vivo imaging. *Nat Nanotechnol*. 2009;4(11):710-711.
10. Yan B, Boyer JC, Branda NR, Zhao Y. Near-infrared light-triggered dissociation of block copolymer micelles using upconverting nanoparticles. *J Am Chem Soc*. 2011;133(49):19714-19717.
11. Viger ML, Grossman M, Fomina N, Almutairi A. Low power

upconverted near-IR light for efficient polymeric nanoparticle degradation and cargo release. *Adv Mater*. 2013;25(27):3733-3738.

12. Yuan Y, Min Y, Hu Q, Xing B, Liu B. NIR photoregulated chemo- and photodynamic cancer therapy based on conjugated polyelectrolyte-drug conjugate encapsulated upconversion nanoparticles. *Nanoscale*. 2014;6(19):11259-11272.
13. Jalani G, Naccache R, Rosenzweig DH, Haglund L, Vetrone F, Cerruti M. Photocleavable Hydrogel-Coated Upconverting Nanoparticles: A Multifunctional Theranostic Platform for NIR Imaging and On-Demand Macromolecular Delivery. *J Am Chem Soc*. 2016;138(3):1078-1083.
14. Chen S, Gao Y, Cao Z, et al. Nanocomposites of Spiropyran-Functionalized Polymers and Upconversion Nanoparticles for Controlled Release Stimulated by Near-Infrared Light and pH. *Macromolecules*. 2016;49(19):7490-7496.
15. Zhao L, Peng J, Huang Q, et al. Near-Infrared Photoregulated Drug Release in Living Tumor Tissue via Yolk-Shell Upconversion Nanocages. *Adv Funct Mater*. 2014;24(3):363-371.
16. Yang Y, Qin Z, Zeng W, et al. Toxicity assessment of nanoparticles in various systems and organs. *Nanotechnol Rev*. 2017;6(3):279-289.
17. Fu C, Liu T, Li L, Liu H, Chen D, Tang F. The absorption, distribution, excretion and toxicity of mesoporous silica nanoparticles in mice following different exposure routes. *Biomaterials*. 2013;34(10):2565-2575.
18. Elsaesser A, Howard CV. Toxicology of nanoparticles. *Adv Drug Deliv Rev*. 2012;64(2):129-137.
19. Yildirimer L, Thanh NTK, Loizidou M, Seifalian AM. Toxicological considerations of clinically applicable nanoparticles. *Nano Today*. 2011;6(6):585-607.
20. Elzoghby AO, Samy WM, Elgindy NA. Protein-based nanocarriers as promising drug and gene delivery systems. *J Control Release*.

2012;161(1):38-49.

21. Liu F, Mu J, Xing B. Recent Advances on the Development of Pharmacotherapeutic Agents on the Basis of Human Serum Albumin. *Curr Pharm Des*. 2015;21(14):1866-1888.
22. Shen Z, Li Y, Kohama K, Oneill B, Bi J. Improved drug targeting of cancer cells by utilizing actively targetable folic acid-conjugated albumin nanospheres. *Pharmacol Res*. 2011;63(1):51-58.
23. Shobini J, Mishra AK, Sandhya K, Chandra N. Interaction of coumarin derivatives with human serum albumin: Investigation by fluorescence spectroscopic technique and modeling studies. *Spectrochim Acta - Part A Mol Biomol Spectrosc*. 2001;57(5):1133-1147.
24. Mueller WE, Wollert U. Human serum albumin as a "silent receptor" for drugs and endogenous substances. *Pharmacology*. 1979;19(2):59-67.
25. El-Hady DA, Albishri HM, Rengarajan R, Deeb S El, Wätzig H. Stabilizing proteins for affinity capillary electrophoresis using ionic liquid aqueous two phase systems: Pharmaceuticals and human serum albumin. *Electrophoresis*. 2015;36(24):3080-3087.
26. Schmidt R, Geissler D, Hagen V, Bendig J. Mechanism of photocleavage of (coumarin-4-yl)methyl esters. In: *Journal of Physical Chemistry A*. Vol 111. American Chemical Society; 2007:5768-5774.
27. Dempster DN, Morrow T, Quinn MF. Extinction coefficients for triplet-triplet absorption in ethanol solutions of anthracene, naphthalene, 2,5-diphenyloxazole, 7-diethylamino- 4-methyl coumarin and 4-methyl-7-amino-carbostyril. *J Photochem*. 1973;2(5):329-341.
28. Priyadarsini KI, Naik DB, Moorthy PN. A study of the triplet state of 7-amino coumarin laser dyes by the nanosecond pulse radiolysis technique. *J Photochem Photobiol A Chem*. 1990;54(2):251-261.

29. Chen Q, Wang C, Cheng L, He W, Cheng Z, Liu Z. Protein modified upconversion nanoparticles for imaging-guided combined photothermal and photodynamic therapy. *Biomaterials*. 2014;35(9):2915-2923.
30. Noguchi M, Skwarczynski M, Prakash H, et al. Development of novel water-soluble photocleavable protective group and its application for design of photoresponsive paclitaxel prodrugs. *Bioorganic Med Chem*. 2008;16(10):5389-5397.
31. Naccache R, Vetrone F, Mahalingam V, Cuccia LA, Capobianco JA. Controlled synthesis and water dispersibility of hexagonal phase $NaGdF_4:Ho^{3+}/Yb^{3+}$ nanoparticles. *Chem Mater*. 2009;21(4):717-723.
32. Bosca F. Seeking to shed some light on the binding of fluoroquinolones to albumins. *J Phys Chem B*. 2012;116(11):3504-3511.

Chapter 8. Instrumentation

8.1. General instrumentation

8.1.1. Nuclear magnetic resonance (NMR)

The one-dimensional (1H, 13C, DEPT-135) NMR spectra were measured by a 300 MHz Varian Bruker instrument, using DMSO-d_6 and $CDCl_3$ as solvents. The corresponding solvent signals were taken as reference (chemical shift of δ of *ca* 2.50 ppm and 7.26 ppm for ^{1}H NMR and 39.52 and 77.16 ppm for ^{13}C NMR, respectively). Coupling constants (*J*) are given in hertz (Hz).

8.1.2. Chromatography

8.1.2.1. Thin-layer liquid chromatography (TLC)

Thin-layer liquid analysis were performed using SiO_2 (silica gel F_{254}) as the stationary phase. In the case of Liquid Chromatography silica gel 60, SDS, 230-400 mesh ASTM was used.

8.1.2.2. High performance liquid chromatography

All samples were analyzed on an Agilent 1100 Series HPLC set up equipped with a diode array detector covering a detection range from 200 to 400 nm. Analysis were performed using a Mediterranean Sea C18 column (250 x 4.6 mm, 5 µm). In all cases the H_2O mobile phase was acidified at a pH of ca. 3 and the flow rate set at 1,5 mL/min.

8.1.2.3. Ultra performance liquid chromatography tandem mass spectrometer (UPLC-MS/MS)

Analysis were performed using an UPLC-MS/MS: ACQUITY UPLC system (Waters Corp.) with a conditioned autosampler at 4 °C. The system uses an ACQUITY UPLC BEH C18 column (50 mm × 2.1 mm i.d., 1.7 µm) maintained at 40 °C. The analysis was achieved with gradient elution using acetonitrile and water (containing 0.01% formic acid) as the mobile phase. The Waters ACQUITY™ XevoQToF Spectrometer (Waters Corp.) was connected to the UPLC system via an electrospray ionization (ESI) interface. The ESI source was operated in positive ionization mode with the capillary voltage at 3.0 kV. The temperature of the source and desolvation was set at 100 °C and 400 °C, respectively. The cone and desolvation gas flows were 100 L h−1 and 800 L h−1, respectively. All data collected in Centroid mode were acquired using Masslynx™ software (Waters Corp.). Leucine-enkephalin was used as the lock mass generating an [M+H]+ ion (m/z 556.2771) at a concentration of 500 pg/mL and flow rate of 50 µL/min to ensure accuracy during the MS analysis.

8.2. Photochemical instrumentation

8.2.1. UV-VIS absorption spectroscopy

All UV-Vis absorption spectra were registered with a simple beam Varian Cary 50 spectrophotometer, using quartz cells of 1cm optical path length.

8.2.2. Time-resolved fluorescence spectroscopy

Time-resolved fluorescence spectra were recorded on an EasyLife V (OBB) spectrofluorimeter. The apparatus was equipped with a diode LED (λ_{exc} = 340 nm) excitation source; the residual excitation signal was filtered in emission by using a cut-off filter (50% transmission at 380 nm).

8.2.3. Steady-state photolysis

Irradiation of the samples was performed under anaerobic conditions in quartz cuvettes of 1 cm optical path length, quartz flasks o, using three a Luzchem photoreactor (model LZV-4V) with a variable number of lamps (maximum output at 350 nm or 420 nm).

8.2.4. Laser flash photolysis spectroscopy (LFP)

For the LFP a pulsed Nd: YAG SL404G-10 Spectron Laser Systems, was used at 355 nm (3rd harmonic) as the excitation wavelength, and the energy of the single pulses (ca 10 ns duration) was setted under 15 mJ pulses. The apparatus consisted of the pulsed laser, a pulsed Lo255 Oriel Xenon lamp, a

77200 Oriel monochromator, an 70705 Oriel photomultiplier tube (PMT) housing, a 70705 PMT power supply and a TDS-640A Tektronix oscilloscope. The output signal from the oscilloscope was transferred to a personal computer and all experiments were performed in quartz cuvettes of 1 cm optical path.

8.2.5. Femtosecond transient absorption spectroscopy

Transient absorption spectra were recorded using a compact regenerative amplifier LIBRA-HE Coherent, a tunable optical paramagnetic amplifier OPERA-SOLO Coherent and the transient absorption spectrometer ExciPro (CDP Systems). Thus, femtosecond laser pulses are produced by a commercial regenerative amplified laser system LIBRA Coherent including in its optical bench an oscillator VITESSE (To seed), a Nd-YLF laser Evolution (to pump the Ti-Za crystal), a regenerative amplifier itself and a stretcher/compressor which outputs 100 fs, 4 mJ pulses centred at 800 nm with a 1 kHz repetition rate. The beam is split into two parts: one beam is used for white light generation (the probe beams) and the second beam is used to pump the tunable optical paramagnetic amplifier OPERA-SOLO Coherent (Light Conversion, TOPAS (UV-VIS)). The OPA provides the pump source with tuneable wavelengths in the range 245–2600 nm and a duration of 100 fs pulse. In the present case, the pump was set at 340 nm (*ca*. 5 μJ pulses) and passed through a chopper prior to focusing onto the sample rotating cell (0.8 mm optical path length) placed into the transient absorption spectrometer ExciPro (CDP Systems). The white light used as probe was produced after part of the 800 nm light from the amplifier passed through a computer-controlled 8 ns variable optical delay line and impinged on a CaF_2 rotating crystal. This white light was split in two identical portions to generate reference and probe beams that then were focused on the rotating cell containing the sample. The pump and the probe coincided in the interrogation of the sample. A computer-controlled imaging spectrometer was placed after

this path to measure the probe and the reference pulses and to obtain the transient absorption decays and spectra.

8.2.6. Phosphorescence emission measurements

The phosphorescence spectra were recorded using a spectrophosphorimeter Photon Technology International (PTI, TimeMater TM/2003) equipped with a pulsed Xenon lamp. Compounds were dissolved in ethanol, adjusting their absorbance at *ca*. 0.8 at the excitation wavelength, with cuvettes of 1cm optical pathway. Measurements were carried out in a quartz tube (0.5 mm diameter) at 77 K.

Singlet-oxygen measurements were performed registering phosphorescence decay traces at 1270 nm after laser pulse employing a Peltier-cooled (- 62.8 ºC) Hamamatsu NIR detector operating at 650 V, coupled to a computer-controlled grating monochromator. A pulsed Nd:YAG L52137 V LOTIS TII was used at the excitation wavelength of 355 nm. The single pulses were of *ca*. 10 ns duration, and the energy was lower than 5 mJ per pulse. The system consisted of the pulsed laser, a 77250 Oriel mono-chromator coupled to the Hamamatsu NIR detector and the oscilloscope connected to the computer. The output signal was transferred from the oscilloscope to a personal computer. All measurements were made at room temperature, under air atmosphere, and using deuterated water at pH *ca*. 7.4 (1mM PB) as solvent in 10 × 10 mm^2 quartz cells with a capacity of 4 mL. The absorbance of the samples was 0.30 at the laser excitation wavelength.

Perinaphthenone in water (singlet oxygen quantum yield (ϕ_Δ) *ca*. 0.98) was used as standard to estimate ϕ_Δ of each compound by comparing the phosphorescence intensities at 1270 nm. The signal was obtained from the average of 50 laser shots. In this context, fresh samples were used each five laser shots to obtain the luminescence of singlet oxygen at 1270 nm.

Chapter 9. General Conclusions

In this doctoral thesis, new drugs, produgs and materials have been investigated, with special emphasis on fluoroquinolones, colchicine and chlorambuxcil as drugs, an aminomethylcoumarin derivative as phototriggers and two types of upconversion nanoparticles as part of new nanosystems. Thus, a thorough research work has been carried out to get a deeper insight into the photochemistry, photophysics and phototoxicity of mentioned systems.

In this context, different strategies have been carried out to investigate new light-mediated cancer treatments. On one hand, a study on new phototoxic drugs, their characteristics under UVA light and using IR light of upconversion nanoparticles. On the other hand, synthesizing new nanosystems by combining new prodrugs formed by a photoremovable protecting group and different drugs with upconversion materials. Very different drugs were selected as object of study based on aforementioned strategies. The first were fluoroquinolones, generally used as antibacterial drugs, but with great photogenotoxic properties. As part of the prodrugs, colchicine, rarely used due to its high toxicity but with great properties and finally chlorambucil as a common anticancer drug.

A study of new photogenotoxic fluoroquinolones and their photophysical, photochemical and phototoxic properties was performed in Chapter 3:

- A new fluoroquinolone (**1**) with a *N*(1)-methyl group in the chromophoric system showed relevant changes in the

photodehalogenation process increasing the generation and lifetime an alkylating intermediate.

- The highest phototoxicity of **1** *in vitro* 3T3 NRU assays was mainly attributed to the photodehalogenation process arising from its triplet excited state FQ.

Next, the interaction between these new fluoroquinolones and others previously described such as Lomefloxacin and its acyl-Lomefloxacin derivative with biomolecules and their phototoxic effects in cells have been analyzed in Chapter 4, assessing that:

- *N*-alkyl chain at the position **1** of these fluoroquinolones is a small structural change that has a great influence in the interactions between FQ and biomolecules.
- The phototoxic effect observed in the FQs of this study can be understood by combining the affinity of these compounds to biomolecules such as DNA and/or proteins with the reactivity of their photogenerated intermediates.

Finally, for fluoroquinolones studies, design of a new material composed by best fluoroquinolone of previous chapters and upconversion nanoparticles was achieved:

- New $NaYF_4$: Yb/Tm (18%, 0,5%) @$NaYF_4$ @**1**-SA material has been synthesized.
- Improvement of the high phototoxic ability observed for compound **1** using nanosystems charged with this molecule.

Going to prodrugs strategies, first, synthesis of new prodrug composed by 7-amino-4-hydroymethylcoumarine chromophore (COU) as photoprotecting group and N-deacetylcolchicine (DCO) was done. However, photolysis of this dyad COU-DCO does not produce drug liberation. Photophysical studies were done to understand this unexpected result:

- Photophysical and photochemical properties of **COU** can be clearly modified when a linked chromophore can generate electron transfer processes as evidenced with **COU**, **COU-DCO** and **COU-PHA**.
- The intermediate responsible of this type of electron transfer process but also the described photorelease reaction associated to coumarin derivatives was established.

Finally, a new material based on a prodrug formed by the linking of a coumarin as phototrigger with chlorambucil as drug and an upconversion nanosystem was studied. As non toxic hydrophilic shell was selected Human Serum Albumin (HAS), which, at the same time, was the loading site for the prodrug:

- An upconversion-based phototriggered drug-release system using HSA as biocompatible shell was synthesized.
- The binding affinity of chemicals to HSA is a novel and easy method to prepare NIR light-responsive nanodrug delivery systems with very high biocompatibility.

Chapter 10. Summary-Resumen-Resum

10.1. Summary

Cancer is one of the leading causes of death worldwide. Generally used anticancer treatments have various side effects produced by their low specificity. This is one of the reasons why the search for new treatments continues.

Within these new investigations is the extensive field of nanomedicine, which can be explained as the study of new materials on a nanometric scale. It can be translated in the reduction of these side effects by increasing the selectivity and specificity of the treatments. Among the nanomaterials are upconversion nanoparticles that are capable of absorbing light in the near infrared and emit it in the ultraviolet-visible region.

On the other hand, since the beginning of the history of medicine, light has been used as a form of treatment, having a very important role. A drawback for such treatments is sometimes the need to use light from the ultraviolet-visible region since biomolecules are capable of absorbing and causing cell damage.

In this context, this Doctoral Thesis focuses on the study of new forms of anticancer treatment combining nanomedicine and light. For this, new phototoxic drugs and new materials capable of being activated by near infrared light have been developed.

First, new fluoroquinolones were synthesized to explore their phototoxic properties for using in photochemotherapy (Chapter 3 of

the Thesis). The photophysical and photochemical characteristics of the new compounds were studied, in addition to their ability to produce greater phototoxicity in cells than fluoroquinolones such as lomefloxacin by applying ultraviolet light.

Based on the results obtained, a study was carried out to determine the differences between the interactions of some dihalogenated fluoroquinolones including the above commented, and biomolecules such as DNA and proteins. The reactivity of their photo-generated intermediates was also studied in Chapter 4.

After a deep knowledge of the phototoxic capacity of the new drugs, design of a nanosystem composed of fluoroquinolones and upconversion nanoparticles was carried out in Chapter 5. The high phototoxic capacity of this new nanosystem was demonstrated. In this way phototoxic activity was generated from a fluoroquinolone without the use of ultraviolet light.

On the other hand, the formation of prodrugs opens a door to the selective administration of anticancer drugs. Prodrugs consist of the photolabile binding of a molecule capable of being activated by light and the drug of interest. However, a knowledge of the photophysical and photochemical properties of the phototrigger as well as the redox potentials of both members of the dyad can be crucial to obtain the desired photorelease. Thus, in Chapter 6, the relevance of these data was highlighted using a prodrug formed by a coumarin derivative as a photoactivatable molecule and colchicine as a drug.

Finally, in Chapter 7 the synthesis of a new nanosystem containing a prodrug formed by a derivative of coumarin linked to the anticancer drug chlorambucil, and upconversion biocompatible nanoparticles was explored. The addition of human serum albumin as a coating for the nanoparticles fulfills the dual function of obtaining biocompatible nanoparticles and being the loading site for the prodrug.

10.2. Resumen

El cáncer es una de las principales causas de muerte a nivel mundial. Los tratamientos anticancerígenos generalmente usados tienen diversos efectos secundarios producidos por su baja especificidad. Esta es una de las razones por las que se sigue en continua búsqueda de nuevos tratamientos.

Dentro de estas nuevas investigaciones se encuentra el extenso campo de la nanomedicina, es decir, el estudio de nuevos materiales a escala nanométrica. Esta permite reducir dichos efectos secundarios aumentando la selectividad y especificidad de los tratamientos. Dentro de los nanomateriales se encuentran las nanopartículas de upconversion que son capaces de absorber luz en el infrarrojo cercano y emitirla en la región ultravioleta-visible.

Por otro lado, desde el principio de la historia de la medicina la luz se ha empleado como forma de tratamiento teniendo un rol muy importante. Un inconveniente para dichos tratamientos suele ser la necesidad de emplear luz de la región ultravioleta-visible, pues las biomoléculas son capaces de absorber y produce daño celular.

En este contexto, la presente Tesis Doctoral se centra en el estudio de nuevas formas de tratamiento anticancerígeno combinando nanomedicina y luz. Para ello se han desarrollado nuevos fármacos fototóxicos y nuevos materiales capaces de ser activados mediante luz infrarroja cercana.

En primer lugar, se sintetizaron nuevas fluoroquinolonas para explorar sus propiedades fototóxicas para su uso en fotoquimioterapia (Capítulo 3 de la Tesis). Se estudiaron las características fotofísicas y fotoquímicas de los nuevos compuestos, además de su capacidad para producir mayor fototoxicidad en las células en comparación con las fluoroquinolonas como la lomefloxacina mediante la aplicación de luz ultravioleta.

En base a los resultados obtenidos se realizó un estudio para determinar las diferencias entre las interacciones de algunas fluoroquinolonas dihalogenadas, incluidas las comentadas anteriormente, y biomoléculas como ADN y proteínas. La reactividad de sus intermedios fotogenerados también se estudió en el Capítulo 4.

Tras conocer en profundidad la capacidad fototóxica de los nuevos fármacos, en el Capítulo 5 se llevó a cabo el diseño de un nanosistema compuesto por fluoroquinolonas y nanopartículas de conversión ascendente. Se demostró la alta capacidad fototóxica de este nuevo nanosistema. De esta manera, se generó actividad fototóxica a partir de una fluoroquinolona sin el uso de luz ultravioleta

Por otro lado, la formación de profármacos abre la puerta a la administración selectiva de fármacos contra el cáncer. Los profármacos consisten en la unión fotolábil de una molécula capaz de ser activada por la luz y el fármaco de interés. Sin embargo, un conocimiento profundo de las propiedades fotofísicas y fotoquímicas del fotodisparador y de los potenciales redox de ambos miembros de la

diada puede ser crucial para obtener la fotoliberación deseada. Así, en el capítulo 6, se destacó la relevancia de estos datos utilizando un profármaco formado por un derivado de cumarina como molécula fotoactivable y colchicina como fármaco.

Finalmente, en el Capítulo 7 se exploró la síntesis de un nuevo nanosistema que contiene un profármaco formado por un derivado de cumarina unido al fármaco contra el cáncer clorambucilo y nanopartículas biocomatibles de conversión ascendente. La adición de albúmina de suero humano como recubrimiento de las nanopartículas cumple la doble función de obtener nanopartículas biocompatibles y ser el lugar de carga del profármaco.

10.3. Resum

El càncer és una de les principals causes de mort a nivell mundial. Els tractaments anticancerígens generalment usats tenen diversos efectes secundaris produïts per la seva baixa especificitat. Aquesta és una de les raons per les que se segueix en contínua recerca de nous tractaments.

Dins d'aquestes noves investigacions es troba l'extens camp de la nanomedicina, és a dir, l'estudi de nous materials a escala nanomètrica. Aquesta permet reduir aquests efectes secundaris augmentant la selectivitat i especificitat dels tractaments. Dins dels nanomaterials es troben les nanopartícules de upconversion que són capaços d'absorbir llum en l'infraroig proper i emetre-la en la regió ultraviolada-visible.

D'altra banda, des del principi de la història de la medicina la llum s'ha emprat com a forma de tractament tenint un paper molt important. Un inconvenient per aquests tractaments sol ser la necessitat d'emprar llum de la regió ultraviolada-visible, ja que les biomolècules són capaços d'absorbir-la i produïr dany cel·lular.

En aquest context, la present Tesi Doctoral es centra en l'estudi de noves formes de tractament anticancerigen combinant nanomedicina i llum. Per això s'han desenvolupat nous fàrmacs fototòxics i nous materials capaços de ser activats mitjançant llum infraroja propera.

En primer lloc, es van sintetitzar noves fluoroquinolones per explorar les seves propietats fototòxiques per al seu ús en

fotoquimioteràpia (Capítol 3 de la Tesi). Es van estudiar les característiques fotofísiques i fotoquímiques dels nous compostos, a més de la seva capacitat per produir major fototoxicitat en les cèl·lules en comparació amb les fluoroquinolones com la lomefloxacina mitjançant l'aplicació de llum ultraviolada.

En base als resultats obtinguts es va realitzar un estudi per determinar les diferències entre les interaccions d'algunes fluoroquinolones dihalogenades, incloses les comentades anteriorment, i biomolècules com ADN i proteïnes. La reactivitat de les seves intermedis fotogenerats també es va estudiar en el Capítol 4.

Després de conèixer en profunditat la capacitat fototòxica dels nous fàrmacs, en el Capítol 5 es va dur a terme el disseny d'un nanosistema compost per fluoroquinolones i nanopartícules de upconversion. Es va demostrar l'alta capacitat fototòxica d'aquest nou nanosistema. D'aquesta manera, es va generar activitat fototòxica a partir d'una fluoroquinolona sense l'ús de llum ultraviolada

D'altra banda, la formació de profàrmacs obre la porta a l'administració selectiva de fàrmacs contra el càncer. Els profàrmacs consisteixen en la unió fotolàbil d'una molècula capaç de ser activada per la llum i el fàrmac d'interès. No obstant això, un coneixement profund de les propietats fotofísiques i fotoquímiques del fotodisparador i dels potencials redox de tots dos membres de la diada pot ser crucial per obtenir el fotoalliberament desitjada. Així, en el capítol 6, es va destacar la rellevància d'aquestes dades utilitzant un

profàrmac format per un derivat de cumarina com a molècula fotoactivable i colquicina com a fàrmac.

Finalment, en el Capítol 7 es va explorar la síntesi d'un nou nanosistema que conté un profàrmac format per un derivat de cumarina unit a l'fàrmac contra el càncer clorambucilo i nanopartícules biocomatibles de upconversion. L'addició d'albúmina de sèrum humà com a recobriment de les nanopartícules compleix la doble funció d'obtenir nanopartícules biocompatibles i ser el lloc de càrrega del profàrmac.

Chapter 11. Scientific contribution

11.1. Contribution to Congresses

- Anaya-Gonzalez, C., Garcia-Lainez, G., Andreu, I., Bosca, F. "Fluoroquinolone Based Materials as Alkilating Bombs". XVI Simposio de Jóvenes Investigadores Químicos, Valencia, 4th-7th November 2019. Oral communication

- Anaya-Gonzalez, C., Andreu, I., Bosca, F. "Studies of Fluoroquinolones as Alkylating Bombs" 17th International Congress on Photobiology and 18th Congress of the European Society for Photobiology, Barcelona, Spain, 25th-30th August 2019. Poster.

- Anaya-Gonzalez, C., Orbe, E., Bosca, F. "Developing a new upconversion nanosystemfor controlled anticancer drug delivery using human serum albumin complexed with a coumarin derivative phototrigger". 9th Nano Ontario Conference, Ottawa, Canada, 22nd-23rd November 2018. Poster

- Anaya-Gonzalez, C., Orbe, E., Tormos, R., Bosca, F. "Drug Photorelease from binding of its phototrigger derivative to albumin Upconversion nanoparticles" 27th Congress of the PhotoIUPAC, Dublin, Ireland, 8th-13th July 2018. Oral communication.

- Anaya-Gonzalez, C., Soldevila, S., Tormos, R., Bosca, F. "Mechanisms involved in photoactivation of caged prodrugs" 17th

Congress of the European Society for Photobiology, Pisa, Italy, 4th-8th September 2017. Poster.

11.2. Publications

- Anaya-Gonzalez, C., Soldevila, S., Garcia-Lainez, G., Bosca, F. & Andreu, I. Chemical tuning for potential antitumor fluoroquinolones. *Free Radic. Biol. Med.* 141, 150–158 (2019)